Titre: Title:	A model study of the effects of microstructure on electrical properties of cardiac bundles
Auteur: Author:	Sining Wang
Date:	1993
Type:	Mémoire ou thèse / Dissertation or Thesis
Référence: Citation:	Wang, S. (1993). A model study of the effects of microstructure on electrical properties of cardiac bundles [Thèse de doctorat, École Polytechnique de Montréal]. PolyPublie. https://publications.polymtl.ca/54403/

URL de PolyPublie: PolyPublie URL:	https://publications.polymtl.ca/54403/
Directeurs de recherche: Advisors:	Fernand A. Roberge, & Joshua L. Leon
Programme: Program:	Non spécifié

UNIVERSITE DE MONTREAL

A MODEL STUDY OF THE EFFECTS OF MICROSTRUCTURE ON ELECTRICAL PROPERTIES OF CARDIAC BUNDLES

par

Sining Wang

INSTITUT DE GENIE BIOMEDICAL

ECOLE POLYTECHNIQUE

THESE PRESENTEE EN VUE DE L'OBTENTION

DU GRADE DE PHILOSOPHIAE DOCTOR (PH.D.)

(GENIE BIOMEDICAL)

Novembre 1993

ISBN 0-315-90026-1

Canada

UNIVERSITE DE MONTREAL

ECOLE POLYTECHNIQUE

Cette thèse intitulée:

A MODEL STUDY OF THE EFFECTS OF MICROSTRUCTURE ON ELECTRICAL PROPERTIES OF CARDIAC BUNDLES

présentée par Sining Wang

en vue de l'obtention du grade de Philosophiae Doctor (Ph.D.)

a été dûment acceptée par le jury d'examen constitué de :

M. GULRAJANI Ramesh M., Ph.D., président

M. ROBERGE Fernand A., Ph.D., directeur

M. LEON Joshua L., Ph.D., co-directeur

M. HENRIQUEZ Craig, Ph.D., membre

M. SAVARD Pierre, Ph.D., membre

Abstract

The influence of structural complexities of cardiac tissue on the conduction of action potentials is manifested by the nonuniform anisotropic propagation of cardiac impulses. This phenomenon may enhance the possibility of unidirectional block and provide areas of slow conduction facilitating micro-reentry. In this thesis we study the effects of microstructure of the electric properties of myocardium using a model of a bundle of parallel fibers. Our main objectives are to investigate: 1) how factors such as cell size and packing density relate to directional resistivities, 2) how to determine anisotropic resistivities from measured interstitial potentials, and 3) how the anisotropic properties affect propagation in a small cardiac bundle. The work is based on a mathematical computer model, referred to as the boundary element model (BEM), which includes the intracellular and interstitial spaces and additional structural information such as the fiber radius, the fiber spacing, and the packing arrangement of the bundle.

The effect of packing density on the conduction velocity and on shape of the propagating action potential is examined by changing the fiber spacing. In general, the BEM and bidomain representation of the bundle yield very similar descriptions of electrical properties. The curvature of the propagating wavefront increases with a more restricted interstitial space which, in turn, is a consequence of tighter packing. There is then a concomitant decrease in conduction velocity and, in the BEM, a concomitant increase in the rate of rise of the upstroke ($\dot{V}_{max}$) at the center of the bundle. The time constant of the foot of the action potential (τ_{foot}) is affected

little by changes in the packing density. The essential difference between the BEM and bidomain model with the condition of equal anisotropy ratio is the absence, in the latter, of an increase in $\dot{V}_{max}$ at the center of the bundle as the packing density increases.

A mathematical method is presented to estimate the bidomain anisotropic resistivities in the bundle. This method estimates the interstitial longitudinal (ρ_{ex}) and radial (ρ_{er}) resistivities, and the intracellular longitudinal resistivity (ρ_{ix}), with either direct or alternating current stimulation. When the method is combined with the four-electrode impedance measurement technique and a sinusoidal current source, the intracellular radial resistivity (ρ_{ir}) can also be estimated. In particular, we investigate the variations of ρ_{ex}, ρ_{er}, ρ_{ix} and ρ_{ir} with the packing density. The predicted values of ρ_{ex} and ρ_{ix} are the same as those obtained with the standard estimation method used in the bidomain model, but a different result is predicted for ρ_{er}. Our simulations indicate that the bidomain model performs well only at relatively low packing density.

The use of the four-electrode impedance measurement technique in conjunction with the bidomain model is limited by the assumption of equal anisotropy ratio between the intracellular and interstitial resistivities. In this thesis, a new method is presented to evaluate the anisotropic resistivities using measured interstitial potentials. With this method, the interstitial resistivities ρ_{ex} and ρ_{er} can be determined at low frequency (*e.g.* $10\,Hz$) sinusoidal stimulation when the electrode spacing is less than half the real part of the space constant ($Re(\lambda(f))$) of the bundle, while the

determination of ρ_{ix} and ρ_{ir} requires higher frequencies (*e.g.* $500\,Hz$) of sinusoidal stimulation and a spacing between the source and potential measurement electrodes about 4.5 to 25 $Re(\lambda(f))$. This new method does not require any assumption about the anisotropy ratio and can be applied by changing the sinusoidal frequency of the stimulating current.

Résumé

L'influence de l'organisation structurale du tissu cardiaque sur la conduction du potentiel d'action se manifeste par la propagation anisotrope non-uniforme des impulsions cardiaques. Ce phénomène peut favoriser l'apparition d'un bloc unidirectionnel des impulsions et créer des zones de conduction lente favorables à la micro-réentrée. Dans cette thèse, on étudie les effets de la microstructure sur les propriétés électriques myocardiques à l'aide d'un modèle d'un faisceau de fibres cardiaques. Le faisceau comprend 169 fibres identiques, disposées de façon parallèle pour former une section transverse hexagonale symmétrique. Chaque fibre est reliée aux fibres voisines immediates par une résistance transverse, répétée à tous les 150 μm le long du faisceau. La longueur du faisceau permet d'obtenir des conditions de propagation stable dans le voisinage de sa partie centrale lorsqu'un stimulus est appliqué à l'une de ses extrémités.

Nos principaux objectifs sont d'examiuer: 1) comment des facteurs comme les dimensions cellulaires et la densité d'empaquetage des fibres affectent la résistivité du tissu selon les différentes directions; 2) comment déterminer ces valeurs de résistivité anisotrope à partir de la mesure des potentiels interstitiels; et 3) comment les propriétés anisotropes affectent la propagation dans un petit faisceau de fibres cardiaques. Le modèle de fibre cardiaque est un câble homogene et uniforme de 5 μm de rayon, avec une membrane excitable de type Beeler-Reuter modifié. La représentation mathématique, appelée modèle à éléments bornés (BE), qui inclut

les espaces intracellulaire et interstitiel, ainsi que des informations structurales additionnelles comme le rayon des fibres et leur arrangement dans le faisceau.

Les effets de la densité d'empaquetage (variation du facteur f_i) sur la vitesse de conduction et la forme du potentiel d'action propagé sont étudiés en changeant l'espacement entre les fibres. Notre approche consiste à comparer le modèle BE au modèle bidomaine. Ce dernier est basé sur une représentation globale des milieux intracellulaire et interstitiel du faisceau, en considérant que les deux milieux sont réparés par une membrane cellulaire continue. Ainsi le modèle bidomaine ne tient pas compte de l'organisation microscopique du faisceau et définit les conditions de propagation au moyen de valeurs moyennes des paramètres.

En général, la description des propriétés électriques démontrées par le modèle BE et le modèle bidomaine sont très semblables. La courbure du front d'onde d'excitation propagée augmente lorsque l'espace interstitiel diminue, et cette diminution résulte à son tour d'un empaquetage plus serré. Il y a alors une diminution parallèle de la vitesse de conduction et, dans le modèle BE, une augmentation concomittante de la vitesse de dépolarisation de la montée du potentiel d'action ($\dot{V}_{max}$) au centre du faisceau. La constante de temps du pied du potentiel d'action (τ_{foot}) est peu modifiée par les changements de densité d'empaquetage. La différence essentielle entre les modèles BE et bidomaine est l'absence, dans ce dernier, d'une augmentation de $\dot{V}_{max}$ au centre du faisceau lorsque f_i augmente.

Pour un front d'onde d'excitation convexe, plus la courbure augmente, plus les cellules situées dans la partie la plus avancée du front sont l'objet d'une fuite accrue de courant due à l'activité des cellules qui sont situées dans la partie la moins avancée. On devrait alors s'attendre à une augmentation de τ_{foor} et à une diminution de $\dot{V}_{max}$ au centre du faisceau, en comparaison avec les valeurs à la surface. Cependant, nos résultats de simulation diffèrent en ce qui a trait à $\dot{V}_{max}$, dont la valeur augmente au centre du faisceau avec une augmentation de la courbure du front d'onde. Ce comportement particulier de $\dot{V}_{max}$ est attribuable au potentiel interstitiel plus elevé au centre du faisceau, particulièrement à haute densité d'empaquetage.

Une méthode mathématique est présentée pour estimer les résistivités anisotropes du faisceau. Cette méthode permettent d'estimer les résistivités interstitielles longitudinale (ρ_{ex}) et radiale (ρ_{er}), ainsi que la résistivité intracellulaire longitudinale (ρ_{ix}), avec un courant de stimulation direct ou alternatif. Quand la méthode est combinée à la technique de mesure d'impédance à quatre électrodes et à la stimulation à l'aide d'un courant sinusoidal, la résistivité intracellulaire radiale (ρ_{ir}) peut aussi être estimée. En particulier, nous étudions les variations de ρ_{ex}, ρ_{er}, ρ_{ix} et ρ_{ir} avec la densité d'empaquetage. Les valeurs de ρ_{ex} et ρ_{ix} prédites par la méthode sont les mêmes que celles obtenues avec l'approche standard basée sur le modèle bidomaine, mais un résultat différent est prédit pour ρ_{er}. Nos simulations

indiquent que l'approche basée sur le modèle bidomaine donne de bons résultats seulement à faible densité d'empaquetage, et qu'elle ne convient pas pour estimer ρ_{ir}.

La technique de mesure d'impédance à quatre électrodes basée sur le modèle bidomaine a été introduite par Plonsey et Barr. Elle est restreinte par l'hypothèse d'un rapport égal entre les résistivités anisotropes intracellulaires et interstitielles. Dans cette thèse, une nouvelle méthode est présentée pour estimer les résistivités anisotropes à partir du potentiel interstitiel. Avec cette méthode, les résistivités interstitielles ρ_{ex} et ρ_{er} peuvent être déterminées à basse fréquence de stimulation (*e.g.*, $10Hz$) sinusoidale lorsque la distance entre les électrodes de stimulation et d'enregistrement est moindre que la moitié de la partie réelle de la constante d'espace ($Re(\lambda(f))$) du faisceau. D'autre part, l'estimation de ρ_{ix} et ρ_{ir} exige une fréquence relativement élevée (*e.g.*, $500\,Hz$) de stimulation sinusoidale et une distance entre les électrodes de $4.5 \sim 25\,Re(\lambda(f))$. Cette nouvelle méthode ne requiert aucune hypothèse concernant le rapport des résistivités anisotropes et peut être utilisée en variant la fréquence sinusoidale du courant de stimulation.

Il est à noter, cependant, qu'en dépit des améliorations apportées par cette nouvelle méthode d'estimation des résistivités tissulaires, il reste encore des limitations importantes. D'une part, à cause de la difficulté de mesurer la dérivée spatiale radiale du potentiel interstitiel dans un faisceau de fibres, la méthode n'est actuelle-

ment applicable qu'à un mince feuillet du tissu. Pour obvier à ceci, on pourrait envisager d'évaluer la dérivée spatiale radiale à partir des valeurs de dérivées spatiales des potentiels interstitiels longitudinal et transverse. D'autre part, la distance interélectrode de 15 μm considérée dans la présente analyse est irréaliste au plan des mesures expérimentales et il faudrait l'augmenter au moins à 30 μm. Ceci amènerait une augmentation d'environ 15% de l'erreur d'estimation, à moins de diminuer davantage la frequence de stimulation sinusoidale (*i.e.*, en-dessous de 10 Hz).

Acknowledgements

With the dream that one day I would be able to contribute something to improve human health, I applied for Ph.D. studies in the Biomedical Engineering Institute. I wish to thank Dr. Fernand A. Roberge who gave me this chance by accepting me as a student. During the last four years, his firm support, invaluable guidance, and encouragement contributed to make my work valuable and challenging.

I would like to express my sincere appreciation to Dr. Josh Leon. As a co-director, he gave me detailed suggestions and helpful guidances in all aspects of my work. His encouragement was a decisive factor in the final stage of this work.

A special thank goes to Mr. Hervé Hogues who designed the initial computer code for this project for providing his kind help at any time we need. I would also like to thank Dr. Kaj Henneberg for offering his insight through discussions and for spending times to read this thesis and making many suggesting comments.

My colleagues and fellow graduate students in the Biomedical Modeling Research Group are really good friends. I have overcome many difficulties through their help, discussions, even debate. Parties, soccer games are nice entertainments to amuse me besides academic discussions, computer simulations, and so on. I would like to thank all these friends for their assistance, kindness and joys. I have enjoyed all the time when I studied here.

Finally, I really appreciate the financial support from the Laboratoire de Modélisation Biomédical de l'Université de Montréal during my studies.

Table of Contents

List of Figures

List of Tables

Table of Symboles

ϕ_i	:	Intracellular potential (mV)
ϕ_e	:	Interstitial potential (mV)
∇^2	:	Laplacian operator
$\vec{\nabla}$	:	Differential operator
$\vec{n}$	:	Unit normal vector of surface
dv	:	Volume element
$d\Omega$	:	Solid angle element
dS	:	Surface element
ϕ_i^j	:	Intracellular potential on surface j (mV)
ϕ_e^j	:	Interstitial potential on surface j (mV)
ϕ^o	:	Potential on exterior surface S^o (mV)
σ_i	:	Bulk intracellular conductivity $(m\mho/cm)$
σ_e	:	Bulk interstitial conductivity $(m\mho/cm)$
I_{m}	:	Membrane current per unit area $(\mu A/cm^2)$
C_{m}	:	Membrane capacitance per unit area $(\mu F/cm^2)$
I_{ion}	:	Ionic current per unit area $(\mu A/cm^2)$
S^k	:	Surface of cell k
Δ^{jv}	:	v^{th} element of j^{th} surface
I_s	:	Point current source
σ_{il}	:	Intracellular conductivity in direction l $(m\mho/cm)$
σ_{el}	:	Interstitial conductivity in direction l $(m\mho/cm)$

R_{m}	:	Transmembrane resistance (Ωcm^2)
λ	:	Space constant of tissue (cm)
k	:	Equal anisotropy ratio of intracellular and interstitial conductivities
a	:	Spacing between potential-measurement and source electrodes (cm)
β	:	Surface to volume ratio of tissue ($1/cm$)
V_m	:	Transmembrane potential $= \phi_i - \phi_e$ (mV)
$\Delta\phi_{el}$	:	Interstitial potential difference between measurement electrodes in direction l
$\Delta\phi_{il}$	:	Intracellular potential difference between measurement electrodes in direction l
λ_l	:	Space constant of tissue in direction l
Z_{m}	:	Membrane impedance per unit area $= R_{\mathrm{m}}\|\|C_{\mathrm{m}}$ (Ωcm^2)
ω	:	Angular frequency (radians/sec)
λ_0	:	Resting-state space constant of bundle (cm)
$Re(\lambda_\omega)$	:	Real part of space constant of bundle at frequency ω
f_i	:	Intracellular volume fraction
$\dot{V}_{max}$	:	Maximum rate of rise of action potential (V/sec) (dV/dt_{max})
τ_{foot}	:	Time constant of foot of action potential ($m\,sec$)
$\vec{J}_i$	:	Intracellular current density per area ($\mu A/cm^2$)
$\vec{J}_e$	:	Interstitial current density per area ($\mu A/cm^2$)
I_v	:	Current density per volume ($\mu A/cm^3$)
ρ_{il}	:	Intracellular resistivity in direction l ($K\Omega\,cm$)
ρ_{el}	:	Interstitial resistivity in direction l ($K\Omega\,cm$)

I_{m_i}	:	Membrane current fit by estimated intracellular resitivities using transmembrane current stimulation ($\mu A/cm^2$)
I_{m_e}	:	Membrane current fit by estimated interstitial resitivities using transmembrane current stimulation ($\mu A/cm^2$)
ΔI_{m}	:	Membrane current difference between measurement electrodes
$\Delta\phi_i$	:	Intracellular potential difference between measurement electrodes
$\Delta\phi_e$	:	Interstitial potential difference between measurement electrodes
ΔV_{m}	:	Membrane potential difference between measurement electrodes
f	:	Frequency of alternating stimulation current (Hz)
$\hat{I}_{\mathrm{m}}$	:	Membrane current fit by estimated interstitial resitivities using *a.c.* current stimulation ($\mu A/cm^2$)
$\hat{I}'_{\mathrm{m}}$	:	Membrane current fit by estimated intracellular resitivities using *a.c.* current stimulation ($\mu A/cm^2$)
$\hat{\phi}_i$	:	Intracellular potential calculated from $\hat{I}_{\mathrm{m}}$ and Z_{m}
$\gamma(f)$	:	$1/\lambda(f)$
R_c	:	Transverse connection resistance ($M\Omega/\mu m$)

Chapter 1

Introduction

A variety of clinical arrhythmias, from atrial flutter to ventricular tachycardia, are caused by reentry. This hypothesis was first suggested in 1897 by McWilliam [50] in his article 'Fibrillar contraction of the heart'. Since then numerous investigations of re-entrant activity have been reported [2, 3, 4, 53, 55]. It is currently believed that slow conduction is associated with the occurrence of reentry. Reentry is usually initiated by a premature beat which is blocked in the direction of the long axis of the cells, with sustained propagation occurring in the transverse direction [49]. There have been substantial efforts devoted to the study of slow conduction and unidirectional block in normal and diseased cardiac tissue. Much of this effort was aimed at understanding how modifications of the active and passive membrane properties, such as alterations in the inward sodium current, led to slow conduction [28]. However, more recent work has focused on the role of cell-to-cell coupling in the transmission of electrical impulses and on the importance of abnormal cell coupling for arrhythmogenesis [7, 43]. Recently, Spach [79, 80, 82] proposed that

the anisotropic structure of the tissue leads to directionally dependent differences in action potential (AP) shape: higher upstroke velocity, shorter τ_{foot} and larger maximum amplitude along wavefronts propagating transversely to the principal fiber direction. Such considerations suggest that the genesis and maintenance of re-entrant activity depend on the complex microscopic structure of the tissue.

1.1 Ultrastructure of cardiac tissue

For many years the heart muscle was considered to be an anatomical syncytium [20]. It is not a true syncytium, however, and it consists of isolated cells joined by specialized areas of contact – the intercalated disks [76]. The disks comprise three junctional complexes: desmosome in which the apposing cell membranes are separated by a gap of 250-390 $\AA$; intermediate junctions and the gap junctions (nexuses) through which the cell membranes are in intimate contact [20, 78]. The nexus is a discrete anatomic entity which provides direct diffusive pathways from one cell to the next. It is composed of connexons consisting of transmembrane proteins with strategically located hydrophilic properties, forming 'low resistance' intercellular channels [9]. The nexus thus introduces a recurrent discontinuity in the resistivity of cardiac tissue.

Cardiac myocytes are linked to each other at their ends, forming a single column. Sommer and Johnson [77] described cardiac tissue in terms of a *unit bundle* (defined as the smallest assembly of cardiac cells completely surrounded by interstitial space) consisting of 2-50 cells side by side. The myocytes within a

unit bundle have many interconnections. These bundles, enveloped by extracellular space, may remain laterally isolated over a distance of two or three cell lengths before adjoining another bundle [78]. This shape and arrangement of the cells give rise to the tissue's anisotropic properties, specifically a higher bulk resistivity across fibers than along their length, thus leading to a higher conduction velocity in the longitudinal than in the transverse direction [13, 79].

1.2 Modeling and Experimental studies of cardiac tissue

Electrical propagation in ventricular muscle results from current flow between cells at a microscopic level. Disruption of this microscale spread of current might be expected to cause cardiac arrhythmias [49]. However, there is a very limited understanding of the underlying mechanism of these arrhythmias, because of the difficulty of measuring microscale voltage and current. This limitation has motivated the development of computer models of electrical propagation. As Spach points out, 'if a satisfactory quantitative model of propagation can be developed for cardiac muscle, it will provide an important base for studying the mechanisms and therapy of cardiac arrhythmias' [81].

The first important modeling studies of propagation in excitable tissue originated with the pioneering work of Hodgkin and Huxley [36], in which they considered the spread of electrical activity along an isolated unmyelinated squid axon. Their model was based on the assumption that a single fiber can be regarded as a

cable-like structure with a core of protoplasm and a thin surface membrane having a high resistance and a large capacity per unit area. This one-dimensional representation is referred to as the *linear core-conductor* model and the associated governing equations are the *cable equations.* The formalism introduced by Hodgkin and Huxley was later extended to other types of excitable fibers, including cardiac tissue [8, 24].

In early investigations of electrophysiological properties of cardiac tissue, Weidmann [87] measured the myoplasmic resistance, membrane resistance, and membrane capacitance of Purkinje fibers of the mammalian heart, assuming that the core-conduction model was applicable. In later experiments [88], he observed that the space constant associated with the exponential decay of the transmembrane potential was significantly longer than the cell length, suggesting cytoplasmic continuity of neighboring cells. Using cable theory for subthreshold conditions, Fozzard [26] described a different membrane capacitance representation, comprising a capacitance in parallel with a capacitance and resistance in series. This result may be a reflection of the influence of the restricted interstitial space. Hellam and Studt [30] found that the structural complexities of tissue organization could significantly affect the electrical properties of cardiac tissue, and indicated that these properties should be included in a core conduction model.

In a series of experiments on small tissue preparations, Spach *et al.* [79, 80, 81] confirmed the earlier results of Sano *et al.* [73] and Clerc [13] regarding the faster conduction velocity along the cell axis, compared to the velocity of transverse prop-

agation. These authors reported also that the shape of the propagated transmembrane potential and the extracellular potential waveform were dependent on the direction of propagation, and that the safety factor of propagation of premature impulses was higher in the transverse than in the longitudinal direction. Finally, based on measurements of conduction velocity, rate of rise, time constant of the foot of the action potential, and extracellular potentials, they concluded that transverse propagation was discontinuous.

Suenson [83] has presented evidence that the shape of the wave front across a strand of cardiac muscle is curved, with the action potential on the surface propagating ahead of that deeper in the strand. Kléber *et al.* [44, 45] have shown that the interstitial space can have a dramatic impact on the electrical behavior of cardiac tissue. These observations cannot be explained by extensions of the continuous cable theory [13]. Recent theoretical studies in electrical behavior of thick cardiac bundles [31, 32, 34, 71], based on the anisotropic bidomain model, have reproduced some of these experimental results [45, 83]. Roth [71] found that the wave front is curved, with the action potential at the surface of the bundle leading that at the center, and conduction velocity changing in proportion to the intracellular volume fraction. Henriquez [32, 34] has shown that the shape of the action potential is influenced by tissue resistivities, in contrast with the predictions of the core-conductor model.

In general, the bundle model is shown to be significantly better than the classical core conductor model in describing the behavior of cardiac tissue. In the

bidomain model, however, the two separate media, the intracellular and interstitial spaces which are homogeneous, anisotropic and juxtaposed everywhere to the excitable membrane, are averaged over many cells. Although the presence of a second domain distinguishes multicellular tissue from a normal electrical conductor or 'monodomain', this model only gives a macroscopic view of the electrical behavior of a cardiac bundle. The important effects arising from the complex ultrastructure of the tissue are ignored.

1.3 Objectives and thesis outline

To improve our understanding of propagation and to enhance our modeling efforts, it is imperative to establish a close link between the model and the structural properties of the tissue. In this thesis, we focus on the role of the structural complexities of cardiac tissue played in modulating the conduction of cardiac impulses. We are particularly interested in the consequences of replacing the very complex structure of cardiac tissue with the averaged conductivity properties of the bidomain model. We will examine how the structural properties relate to the bulk parameters and attempt to understand how such factors as cell size, density of cell packing, etc. influence tissue anisotropy, bulk intracellular and interstitial resistivities, and tissue capacitance. We will use the boundary element method, a mathematical/computer model based on Green's theorem [38, 39, 47] which allows us to include detailed structural information, to make a thorough analysis of the bidomain approach and

to compare these results with previously published data using the bidomain model. We will combine the four-electrode technique and the boundary element method to evaluate the anisotropic bidomain conductivities of the bundle, and the results will be compared with simulations carried out using the bidomain model.

The theoretical principles of the boundary element method and the four-electrode measurement technique are discussed in Chapter 2. In Chapter 3, we examine the effects of tissue structure on the conduction velocity and shape of the propagating wavefront, and compare the results with the predictions of the bidomain model. An alternative theoretical method to estimate bidomain conductivities based on known intracellular and interstitial potentials and membrane current is presented in Chapter 4. We use this method to investigate the conductivity distributions in a cardiac bundle, and study how these conductivities are influenced by the packing density of the bundle. The results are compared with those obtained from the standard formulation of the bidomain model. In Chapter 5, we present a method to combine the four-electrode measurement technique and the boundary element method to evaluate the bidomain anisotropic conductivities from measured interstitial potentials. In this chapter we will also discuss the criteria for the inter-electrode spacing of the four-electrode system, as well as the determination of the interstitial and intracellular conductivity parameters, and the expected quality of the estimates. Finally, in Chapter 6 the main findings of this thesis are summarized.

Chapter 2

Theory

Propagation in a bundle of cardiac fibers has been studied by several investigators using models based on one-dimensional continuous cable theory [42]. This assumes that the transmembrane potential is constant across any cross-section, which has led us to ask: Can the tissue at the surface of a preparation be represented by the same one-dimensional cable as the tissue at the center? Experimental observations have shown this assumption to be incorrect [13, 83], and raised the possibility of serious errors in the interpretation of data. Recently Roth [71] and Henriquez [34] used the anisotropic bidomain model to evaluate these effects. Both of these studies have predicted that the magnitude of the interstitial potential within a bundle of cardiac fibers could be high enough to significantly affect the shape of the activation wave front and the shape of the action potential.

2.1 The bidomain model

Cardiac muscle is a multicellular tissue and, on a microscopic level, each point outside the membrane is in either the intracellular or the interstitial space. The voltage distribution cannot be calculated correctly without taking both spaces into account. The bidomain model was developed to describe such multicellular syncytial tissue, first presented by Miller and Geselowitz in relation to the electrocardiogram [52], by Tung [84] in reference to ischemic myocardial *d.c.* potential, and by Eisenberg *et al.* in relation to the lens of the eye [25]. The term 'bidomain' arises because two separate domains are considered, which represent the intracellular and interstitial spaces averaged over many cells. Current passes from one domain to the other through the cell membrane. The electrical properties of each domain depend on the passive electrical properties of the intracellular and interstitial fluids, the properties of junctions between cells and the geometrical arrangement of the cells. The model was used successfully to account for the human electrocardiogram and magnetocardiogram in the normal and ischemic heart [27, 52], as well as for potentials in a tissue bath preparation [79].

In the bidomain model, the intracellular and interstitial media are assumed to be homogeneous and anisotropic, and connected everywhere by an excitable membrane, ignoring the complex ultrastructure of the tissue. In this chapter we describe an alternative approach which retains more of the structural complexity of the tissue. This approach is based upon the quasi-static model of an excitable cell [60], using Green's theorem to develop an expression for the intracellular and interstitial

potentials at the cell membrane. The model results in a three-dimensional electrostatic problem. A Boundary Element Method is then used to solve for the potential distributions.

2.2 Boundary element method

The boundary element method is an alternative formulation of the cable equation to model excitation in a cylinder of cardiac fiber. It makes use of Green's theorem to develop an expression for the intracellular and interstitial potential at the membrane. This expression includes both the transmembrane current, which is derived from the Beeler-Reuter model with modified sodium current [23], and complex microstructure. The method has been described in detail previously [40, 47]. We briefly explain it in this section.

2.2.1 Mathematical fundamentals

Cardiac tissue that consists of two volumes, intracellular (i) and interstitial (e) domains separated by the cell membrane, are assumed to have good conducting properties. Since the highest harmonic component of significance in bioelectric systems is on the order of $1kHz$, the distribution of potentials and currents in cardiac tissue can be expressed by quasi-static formulations [60]. The basic hypotheses underlying this model are:

- The individual fibers in a bundle are closed volumes.
- The intracellular and interstitial media are uniform and isotropic.

- The density of the membrane current is described by the modified Beeler-Reuter model [23] or Ebihara-Johnson model [24].

- The extracellular medium surrounding the tissue is unbounded and the potential at infinity is zero.

Assuming that a cell with a volume v and closed surface S is surrounded by the infinite extracellular space as illustrated in Fig.1 a), Green's theorem ([17], p257) allows us to write down an expression for the potential ϕ at the observation point P as follows:

$$k\phi(P) = -\int_v \frac{\nabla^2\phi}{r}\,dv + \int_S \frac{\vec{\nabla}\phi\cdot\vec{n}}{r}\,dS - \int_S \phi\vec{\nabla}(\frac{1}{r})\cdot\vec{n}\,dS \tag{2.1}$$

where $\vec{n}$ represents the normal vector of the surface element dS with the positive direction from the inside to the outside of surface S, r is the distance between P and surface element dS or volume element dv. The constant k takes the following values according to the location of P :

$$k = \begin{cases} 4\pi & \text{if } P \text{ is inside of volume } v \\ 2\pi & \text{if } P \text{ is on surface } S \\ 0 & \text{if } P \text{ is outside of volume } v\,. \end{cases}$$

On the membrane surface, there is no static electrical charge, so that both $\nabla^2\phi_i$ and $\nabla^2\phi_e$ are equal to zero, and $k = 2\pi$. Then the intracellular and interstitial potentials on the membrane surface can be written as:

$$\phi_i(P) = \frac{1}{2\pi}\int_S \frac{\vec{\nabla}\phi_i\cdot\vec{n}}{r}\,dS - \frac{1}{2\pi}\int_S \phi_i\vec{\nabla}(\frac{1}{r})\cdot\vec{n}\,dS \tag{2.2}$$

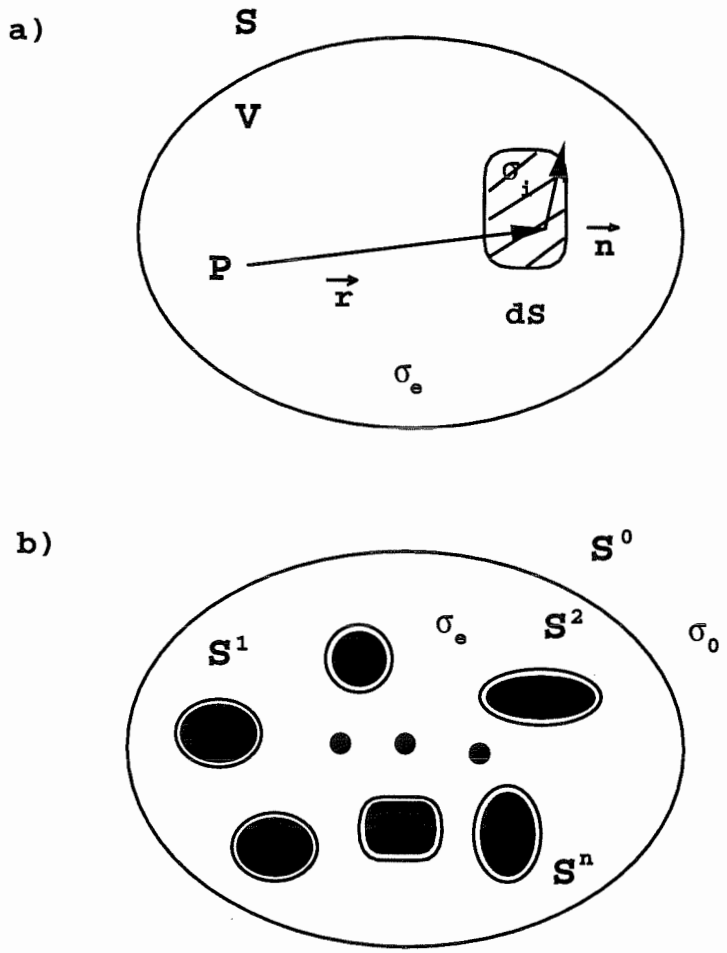

Figure 2.1: a) A single cell of conductivity σ_i surrounded by a volume conductor of conductivity σ_e. P: observation point, $\vec{r}$: distance vector between the observation site and the source pointing from P to the source, $\vec{n}$: the normal unit vector for the cell surface ds, v and S: volume and surface of the surrounding volume conductor. b) N cells separated by the interstitial medium of conductivity σ_e and surrounded by the extracellular volume of conductivity σ_o. $S^1 \cdots S^n$ represent the surface of cell $1 \cdots n$, and S^0 is the surface of the surrounding volume conductor.

$$\phi_e(P) = -\frac{1}{2\pi}\int_S \frac{\vec{\nabla}\phi_e \cdot \vec{n}}{r}\, dS + \frac{1}{2\pi}\int_S \phi_e \vec{\nabla}(\frac{1}{r}) \cdot \vec{n}\, dS\ . \tag{2.3}$$

In a multicellular system such as in Fig.1 b) (surface S° represents the envelope outside the interstitial space), the intracellular and interstitial potentials on j^{th} cell can be expressed as:

$$2\pi\phi_i^j(P_j) = \int_{S^j} \frac{\vec{\nabla}\phi_i^j \cdot \vec{n}}{r}\, dS - \int_{S^j} \phi_i^j \vec{\nabla}(\frac{1}{r}) \cdot \vec{n}\, dS \tag{2.4}$$

$$2\pi\phi_e^j(P_j) = \int_{S^\circ} \frac{\vec{\nabla}\phi^\circ \cdot \vec{n}}{r}\, dS - \int_{S^\circ} \phi^\circ \vec{\nabla}(\frac{1}{r}) \cdot \vec{n}\, dS$$

$$-\sum_{k=1}^{n}\left(\int_{S^k} \frac{\vec{\nabla}\phi_e^k \cdot \vec{n}}{r}\, dS - \int_{S^k} \phi_e^k \vec{\nabla}(\frac{1}{r}) \cdot \vec{n} dS\right) \tag{2.5}$$

where ϕ° stands for the potential on surface S°. In general, the external surface S° can be considered as a sphere of radius $R_\circ$. When $R_\circ \to \infty$, the extracellular medium occupies the whole space. For the extracellular potential $\phi^\circ \propto 1/r$, we have

$$\lim_{R_\circ \to \infty} \phi^\circ = 0$$

$$\int_{S^\circ} \vec{\nabla}\phi^\circ \cdot \vec{n}\, dS = \frac{I}{\sigma_e}\ .$$

The second equation results from the conservation of current if there exists a current source on the external surface. Substituting it into the first term on the right side of Eq.(2.5), we obtain

$$\int_{S^\circ} \frac{\vec{\nabla}\phi^\circ \cdot \vec{n}}{r}\, dS = \frac{I}{\sigma_e R_\circ} \longrightarrow 0\ . \tag{2.6}$$

Therefore, Eq.(2.5) is simplified as

$$2\pi\phi_e^j(P_j) = -\sum_{k=1}^{n}\left(\int_{S^k}\frac{\vec{\nabla}\phi_e^k\cdot\vec{n}}{r}\,dS - \int_{S^k}\phi_e^k\vec{\nabla}(\frac{1}{r})\cdot\vec{n}\,dS\right) . \tag{2.7}$$

Eqs (2.4) and (2.7) are the general formulas which describe the potential distributions in a multicellular system.

Considering the boundary conditions of intracellular and interstitial potentials at the cell membrane:

$$\vec{\nabla}\phi_i\cdot\vec{n} = -\vec{E}_i\cdot\vec{n} = -\frac{\vec{J}_i}{\sigma_i}\cdot\vec{n} = -\frac{I_{\rm m}}{\sigma_i} \tag{2.8}$$

$$\vec{\nabla}\phi_e\cdot\vec{n} = -\vec{E}_e\cdot\vec{n} = -\frac{\vec{J}_e}{\sigma_e}\cdot\vec{n} = -\frac{I_{\rm m}}{\sigma_e} \tag{2.9}$$

where $I_{\rm m}$ is the membrane current per unit area ($\mu A/cm^2$), σ_i and σ_e are conductivities of the intracellular and interstitial volumes ($siemens/cm$). Expressing the membrane current as

$$I_{\rm m} = C_{\rm m}\frac{\partial(\phi_i-\phi_e)}{\partial t} + I_{ion}\,, \tag{2.10}$$

Eqs (2.4) and (2.7) become:

$$2\pi\sigma_i\phi_i^j(P_j) = -\int_{S^j}\left(C_{\rm m}\frac{\partial(\phi_i-\phi_e)}{\partial t} + I_{ion}\right)\frac{dS}{r} + \sigma_i\int_{S^j}\phi_i^j\,d\Omega \tag{2.11}$$

$$2\pi\sigma_e\phi_e^j(P_j) = \sum_{k=1}^{n}\left[\int_{S^k}\left(C_{\rm m}\frac{\partial(\phi_i-\phi_e)}{\partial t} + I_{ion}\right)\frac{dS}{r} - \sigma_e\int_{S^k}\phi_e^k\,d\Omega\right] \tag{2.12}$$

where $d\Omega = -\vec{\nabla}(1/r)\cdot\vec{n}\,dS$ represents the solid angle of the surface element dS with respect to the observation point P_j.

2.2.2 Numerical solution

For most complicated surface shapes, we have to resort to a numerical solution for Eqs (2.11) and (2.12). Decomposing each cell surface of S^j into m^j elements, which are small enough so that potentials ϕ_i^j and ϕ_e^j can be considered as constants on each element, Eqs (2.11) and (2.12) become:

$$2\pi\sigma_i\phi_i^{ju} = \sum_{v=1}^{m^j}\left(-I_{ion}^{jv}\int_{\triangle^{jv}}\frac{dS}{r} - C_{\mathrm{m}}\frac{\partial\phi_i^{jv}}{\partial t}\int_{\triangle^{jv}}\frac{dS}{r} + C_{\mathrm{m}}\frac{\partial\phi_e^{jv}}{\partial t}\int_{\triangle^{jv}}\frac{dS}{r} + \sigma_i\phi_i^{jv}\int_{\triangle^{jv}}d\Omega\right) \tag{2.13}$$

$$2\pi\sigma_e\phi_e^{jv} = \sum_{k=1}^{n}\sum_{u=1}^{m^k}\left(I_{ion}^{ku}\int_{\triangle^{ku}}\frac{dS}{r} + C_{\mathrm{m}}\frac{\partial\phi_i^{ku}}{\partial t}\int_{\triangle^{ku}}\frac{dS}{r} - C_{\mathrm{m}}\frac{\partial\phi_e^{ku}}{\partial t}\int_{\triangle^{ku}}\frac{dS}{r} - \sigma_e\phi_e^{ku}\int_{\triangle^{ku}}d\Omega\right). \tag{2.14}$$

Denoting matrices A_{jk} and B_{jk} as:

$$[A_{jk}]_{uv} = \int_{\triangle^{kv}}\frac{dS}{r} \;\; and \;\; [B_{jk}]_{uv} = \int_{\triangle^{kv}}d\Omega\,, \tag{2.15}$$

where j, k, u and v are cell surface elements. The above discretized Eqs (2.13) and (2.14) can be rewritten more concisely in a matrix form. Suppose potentials and ionic current at cell 'k' can be represented by the following matrices,

$$\mathbf{\Phi}_i^k = \begin{pmatrix}\phi_i^{k1}\\ \phi_i^{k2}\\ \vdots\\ \phi_i^{km^k}\end{pmatrix}, \;\; \mathbf{\Phi}_e^k = \begin{pmatrix}\phi_e^{k1}\\ \phi_e^{k2}\\ \vdots\\ \phi_e^{km^k}\end{pmatrix} \; and \; \mathbf{I}_{ion}^k = \begin{pmatrix}I_{ion}^{k1}\\ I_{ion}^{k2}\\ \vdots\\ I_{ion}^{km^k}\end{pmatrix},$$

then, Eqs (2.13) and (2.14) take the matrix form as:

$$C_{\mathrm{m}}\begin{pmatrix}\mathbf{A}_c & -\mathbf{A}_c\\ \mathbf{C}_c & -\mathbf{C}_c\end{pmatrix}\begin{pmatrix}\mathbf{\Phi}_i^c\\ \mathbf{\Phi}_e^c\end{pmatrix}' - \begin{pmatrix}\sigma_i(\mathbf{B}_c - 2\pi I) & 0\\ 0 & \sigma_e(\mathbf{D}_c + 2\pi I)\end{pmatrix}\begin{pmatrix}\mathbf{\Phi}_i^c\\ \mathbf{\Phi}_e^c\end{pmatrix} + \begin{pmatrix}\mathbf{A}_c & 0\\ 0 & \mathbf{C}_c\end{pmatrix}\begin{pmatrix}\mathbf{I}_{ion}^c\\ \mathbf{I}_{ion}^c\end{pmatrix} = \begin{pmatrix}0\\ 0\end{pmatrix}. \tag{2.16}$$

Where the sign ' stands for time derivatives, matrices $\mathbf{A}_c$ and $\mathbf{B}_c$ are diagnal matrices, $\mathbf{C}_c$ and $\mathbf{D}_c$ are full matrices, which are defined as follows:

$$\mathbf{A}_c = \begin{pmatrix} A_{11} & 0 & \cdots & 0 \\ 0 & A_{22} & \cdots & 0 \\ \vdots & \ddots & \ddots & 0 \\ 0 & \cdots & 0 & A_{nn} \end{pmatrix} \quad \mathbf{C}_c = \begin{pmatrix} A_{11} & A_{12} & \cdots & A_{1n} \\ A_{21} & A_{22} & \cdots & A_{2n} \\ \vdots & \vdots & \ddots & \vdots \\ A_{n1} & A_{n2} & \cdots & A_{nn} \end{pmatrix}$$

$$\mathbf{B}_c = \begin{pmatrix} B_{11} & 0 & \cdots & 0 \\ 0 & B_{22} & \cdots & 0 \\ \vdots & \ddots & \ddots & 0 \\ 0 & \cdots & 0 & B_{nn} \end{pmatrix} \quad \mathbf{D}_c = \begin{pmatrix} B_{11} & B_{12} & \cdots & B_{1n} \\ B_{21} & B_{22} & \cdots & B_{2n} \\ \vdots & \vdots & \ddots & \vdots \\ B_{n1} & B_{n2} & \cdots & B_{nn} \end{pmatrix}$$

and Φ_i^c, Φ_e^c and $\mathbf{I}_{ion}^c$ are combined matrices for all 'n' cells:

$$\Phi_i^c = \begin{pmatrix} \phi_i^1 \\ \phi_i^2 \\ \vdots \\ \phi_i^n \end{pmatrix} , \quad \Phi_e^c = \begin{pmatrix} \phi_e^1 \\ \phi_e^2 \\ \vdots \\ \phi_e^n \end{pmatrix} \; and \; \mathbf{I}_{ion}^c = \begin{pmatrix} I_{ion}^1 \\ I_{ion}^2 \\ \vdots \\ I_{ion}^n \end{pmatrix} .$$

Using $\vec{\Phi}$ to represent combined intracellular and interstitial potentials, matrix (2.16) can be abbreviated as:

$$\mathbf{M}_1 \frac{\partial \vec{\Phi}}{\partial t} + \mathbf{M}_2 \vec{\Phi} + \mathbf{M}_3 \vec{\mathbf{I}}_{ion} = 0 \, . \tag{2.17}$$

The integrals in matrices $\mathbf{M}_1$, $\mathbf{M}_2$ and $\mathbf{M}_3$ can be computed using standard analytical methods ([12] p346). Now discretizing Eq.(2.17) in time by setting $t_i = t_{i-1} + \triangle t$, the final numerical equation is

$$(\mathbf{M}_1 + \triangle t \mathbf{M}_2)\vec{\Phi}(t_i) = \mathbf{M}_1 \vec{\Phi}(t_{i-1}) - \triangle t \mathbf{M}_3 \vec{\mathbf{I}}_{ion}(t_{i-1}) \tag{2.18}$$

or,

$$\vec{\Phi}(t_i) = (\mathbf{M}_1 + \triangle t \mathbf{M}_2)^{-1}(\mathbf{M}_1 \vec{\Phi}(t_{i-1}) - \triangle t \mathbf{M}_3 \vec{\mathbf{I}}_{ion}(t_{i-1})) \, . \tag{2.19}$$

The system can be solved by either direct or iterative methods. Reviewing the whole procedure developed above, it is noted that there is no limitation on the structures of the multicellular system. The extent to which the complexity of the tissue structure can be included in this model depends only on whether the integrals of Eq.(2.15) can be computed numerically.

2.2.3 Point source stimulation

A monopolar point source of intensity I_s within the interstitial space can be included in Eq.(2.16). Supposing a small sphere Γ with radius R_Γ centered at the point source, the potential on the surface of this small sphere will be referred to as ϕ_e and the current density of the surface is

$$\frac{I_s}{4\,\pi\,R_\Gamma^2} \quad .$$

Thus Eq.(2.7) should include the following terms

$$-\int_\Gamma \frac{\vec{\nabla}\phi_e^\Gamma \cdot \vec{n}}{r}\,dS + \int_\Gamma \phi_e^\Gamma\,\vec{\nabla}\frac{1}{r}\cdot\vec{n}\,dS \quad . \tag{2.20}$$

Considering

$$\vec{\nabla}\phi_e^\Gamma \cdot \vec{n} = -\vec{E}_e^\Gamma \cdot \vec{n} = -\frac{\vec{J}^\Gamma}{\sigma_e}\cdot\vec{n} = -\frac{1}{\sigma_e}\,\frac{I_s}{4\,\pi\,R_\Gamma^2}$$

and

$$\vec{\nabla}\frac{1}{r}\cdot\vec{n}\,dS = -d\Omega$$

Eq.(2.20) becomes

$$\frac{1}{\sigma_e}\left(\int_\Gamma \frac{I_s}{4\,\pi\,R_\Gamma^2}\,\frac{dS}{r} - \sigma_e\int_\Gamma \phi_e^\Gamma\,d\Omega\right) \quad . \tag{2.21}$$

When $R_\Gamma \to 0$, the potential on the surface can be considered as constant, then

$$\int_\Gamma \phi_e^\Gamma \, d\Omega \to \phi_e^\Gamma \int_\Gamma d\Omega$$

and

$$\int_\Gamma d\Omega \to 0$$

when Γ is a closed surface, the first term of the above equation is

$$\frac{1}{\sigma_e} \frac{I_s}{4\,\pi\, R_\Gamma^2} \int_\Gamma \frac{dS}{r} \longrightarrow \frac{1}{\sigma_e} \frac{I_s}{4\,\pi\, R_\Gamma^2} \frac{4\,\pi\, R_\Gamma^2}{r_s} \longrightarrow \frac{1}{\sigma_e} \frac{I_s}{r_s}$$

where r_s represents the distance between the observation point P_j and the stimulation point P_s.

We define a vector $R^j(P_s)$ of order m^j that stands for the reciprocal distance between each element on cell j (total m^j elements on cell j) and the stimulation point, so that the following vector should be added to the right side of Eq.(2.16)

$$I_s \begin{pmatrix} 0 \\ 0 \\ \vdots \\ 0 \\ R^1(P_s) \\ \vdots \\ R^n(P_s) \end{pmatrix} \begin{matrix} \\ \\ \\ \leftarrow \quad n \\ \leftarrow \quad n+1 \\ \\ \end{matrix} .$$

If the stimulation source is located inside cell j, the positions of $R^j(P_s)$ added to Eq.(2.16) should correspond to the intracellular potential, which is related to the upper part of the above vector. For multi-monopolar current sources, we simply need to extend the distance vector $R^j(P_s)$ to a matrix $R_k^j(P_s)$, where $k = 1, 2, \cdots n$ represents the number of point sources.

2.2.4 Intracellular junctions

In this subsection we describ how the intracellular junction resistances are included in the boundary element method. Consider a channel connecting element v of cell j to element u of cell k with resistance R_c, P_c^j and P_c^k represent the observation points on either cell. The connection resistance R_c will allow current flowing from element v to element u. In this case the intracellular boundary condition at the cell membrane represented by Eq.(2.8) can be modified to

$$\vec{\nabla}\phi_i^{jv} \cdot \vec{n} = -\frac{1}{\sigma_i}\left(I_{\rm m} - \frac{\Delta\phi_i^{vu}}{R_c}\right)$$

where $\Delta\phi_i^{vu} = \phi_i^{jv} - \phi_i^{ku}$. Thus the first integral of Eq.(2.4) or the first three integrals of Eq.(2.13) for element v becomes

$$\begin{aligned} 2\pi\sigma_i\phi_i^{jv} &= -\int_{S^{jv}}\left(I_{\rm m} - \frac{\Delta\phi_i^{vu}}{R_c}\right)\frac{dS}{r} \\ &= -\int_{S^{jv}} I_{\rm m}\frac{dS}{r} + \int_{S^{jv}}\frac{1}{R_c}\left(\phi_i^{jv} - \phi_i^{ku}\right)\frac{dS}{r}\,. \end{aligned} \tag{2.22}$$

Using vectors $R^j(P_c^j)$ and $R^k(P_c^k)$ of orders m^j and m^k to represent the reciprocal distance between P_c^j, P_c^k and junction locations v and u, the effect of intracellular connection resistance can be included into matrix $\mathbf{A}_c$ by making the following modification:

$$\mathbf{A}_c = \begin{pmatrix} A_{11} & \cdots & \cdots & 0 & \\ \vdots & \ddots & & & \\ \cdots & A_{jj} - R^j(P_c^j)(I_u^{m^j})^T/R_c & \cdots & R^j(P_c^j)(I_v^{m^k})^T/R_c & \cdots & \leftarrow j \\ & & \vdots & & & \\ \cdots & R^k(P_c^k)(I_u^{m^j})^T/R_c & \cdots & A_{kk} - R^k(P_c^k)(I_v^{m^k})^T/R_c & \cdots & \leftarrow k \\ & & & \ddots & 0 & \\ 0 & \cdots & & \cdots & A_{nn} & \end{pmatrix}$$

where

$$(I_v^{m^j})^T = (\overbrace{0,\cdots,0,1,0,\cdots,0}^{m^j})$$
$$\uparrow$$
$$v$$

2.2.5 Validation of the model

The boundary element model (BEM) has been validated by simulating action potential propagation in a cylindrical bundle of cardiac tissue [39, 47], and comparing the results with data published by Roth [71]. The bundle simulated with the BEM consists of many parallel fibers and is illustrated in Fig.2.2. The bundle is a model of uniform anisotropic cardiac tissue. It is assumed that the dimensions and conductivity are the same for all fibers, and the effects of inhomogeneities introduced by collagen, blood vessle, mitochondria etc. are ignored. A cylindrical coordinate system is used, with x and r denoting the axial and radial directions, respectively. Nominal values of intracellular and interstitial conductivities were chosen as $5.0\,mS/cm$ and $66.66\,mS/cm$, respectively, to match earlier modeling studies carried out in our laboratory on excitation in strands of ventricular tissue [10]. The bundle is surrounded by an unbounded extracellular space of the same conductivity as the interstitial medium. The radius of each fiber is $5\,\mu m$ and the length is $3\,mm$. Resistive connections linking each fiber to its six immediate neighbors were introduced at every $150\mu m$. The nominal connection resistance (R_n) was $5M\Omega$.

Fig.2.3 shows the symmetric hexagonal organization of the bundle. This con-

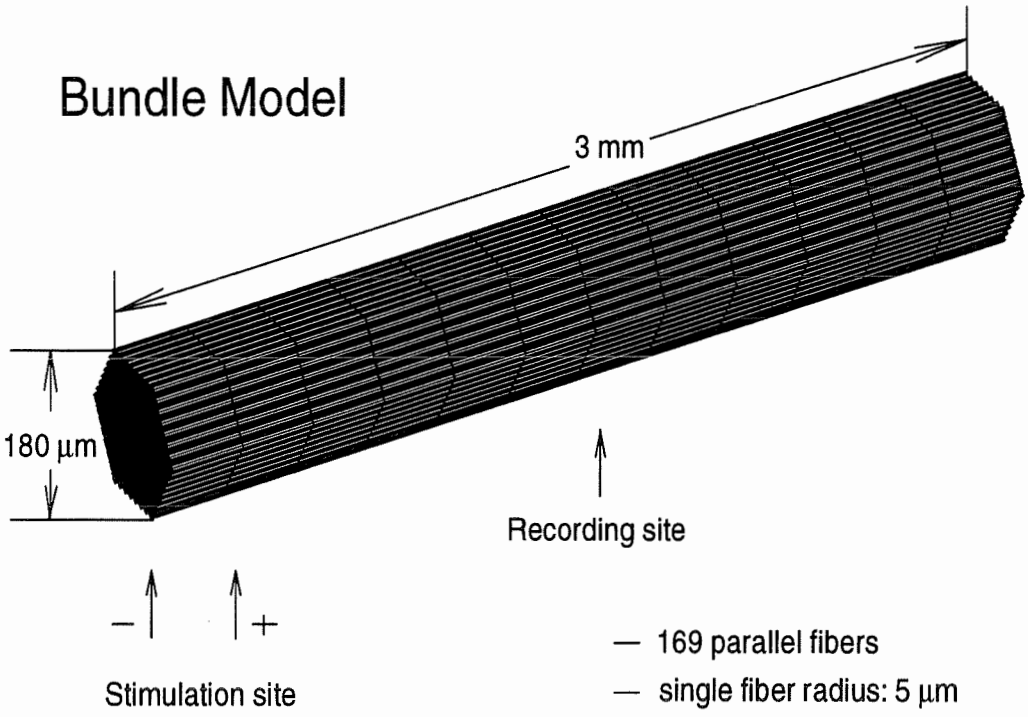

Figure 2.2: The bundle configuration. Individual fibers are oriented in parallel and arranged symmetrically into an hexagonal bundle. Each individual fiber is a closed volume. The stimulation site is located at the proximal end. Action potentials are recorded at mid-length to avoid end-effects.

figuration makes it possible to subdivide the bundle into 12 equal triangular segments, thereby allowing us to simulate only one of these segments and to extrapolate the results to the rest of the bundle through application of symmetry. Simulations were performed on the SGI-4D 280 IRIS computer server (Silicon Graphics Inc. Mountain View, California). Programs implementing the model were written in C. The software package is divided into three separate parts. In the first one, the surface integrals (see Eq.(2.15)) are calculated and stored. The second part serves to construct matrices $\mathbf{A}_c$, $\mathbf{B}_c$, $\mathbf{C}_c$ and $\mathbf{D}_c$ (see Eq.(2.16)) using the results from the first step. The third part is the final simulation stage.

2.3 The four-electrode measurement technique

Biological electrical impedance measurements date back to the late 1800s [1]. In general, the purpose is to investigate the fundamental electrical properties of cardiac tissue [13] or to correlate these properties with the myocardial structure [79, 80, 81]. In earlier studies, current was injected through a bipolar electrode to determine the bulk resistivity of the tissue. In this case, the polarization impedance at the metal-electrolyte interface alters the charge distribution [1] and causes a significant distortion of measurements [61, 75]. The four-electrode technique was introduced to avoid this problem [13, 72]. A diagram (Fig.2.4) shows the principle of the technique. It utilizes a linear array of four equally spaced electrodes, the exterior pair to carry the applied current, and the interior pair to measure the resulting

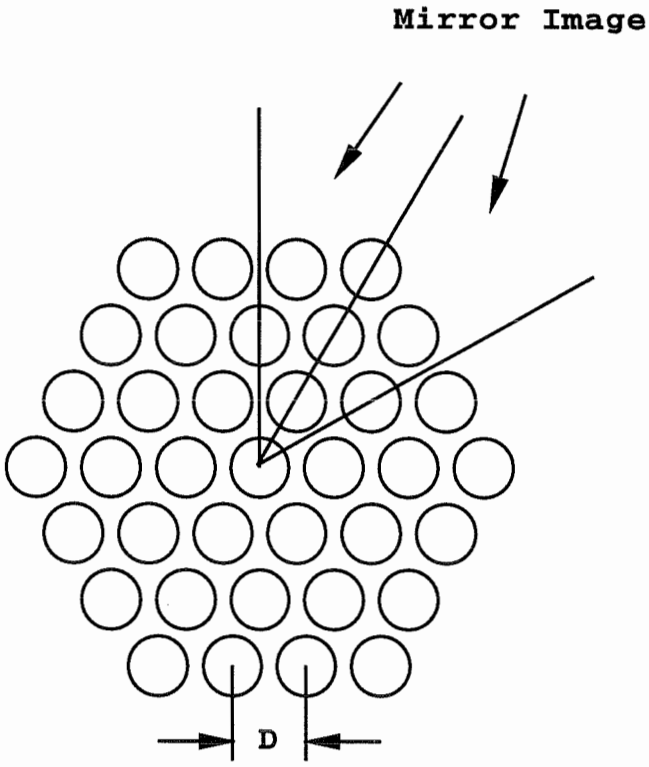

Figure 2.3: Diagram of a cross-section of the bundle. The symmetric hexagonal organization of the bundle consists of 12 triangular segments. D, the distance between fibers, is the factor that controls the packing density of the bundle.

voltage. Since the potential sensing electrodes are connected to an amplifier with high input impedance there is no significant current passing through the electrodes, thus electrode polarization impedance can be eliminated entirely [1].

2.3.1 Combination with the bidomain model

Plonsey and Barr [61] have described a method to estimate tissue conductivities in the anisotropic bidomain model using the four-electrode measurement technique, under the condition of equal anisotropy ratio and point source stimulation. Assuming the medium to be anisotropic, uniform, and infinite in extent, they obtained the following analytical solutions for the intracellular and interstitial potentials of cardiac tissue:

$$\phi_i = -\frac{I_s}{4\pi\sigma}\left(\frac{k}{1+k}\right)\frac{e^{-R/\lambda}}{R} + \left(\frac{k}{1+k}\right)\frac{I_s}{4\pi\sigma R} \tag{2.23}$$

$$\phi_e = \frac{I_s}{4\pi\sigma}\left(\frac{k^2}{1+k}\right)\frac{e^{-R/\lambda}}{R} + \left(\frac{k}{1+k}\right)\frac{I_s}{4\pi\sigma R}\,. \tag{2.24}$$

with

$$\sigma = \sqrt{\sigma_{ix}\sigma_{iy}\sigma_{iz}}\,, \quad k = \frac{\sigma_{ix}}{\sigma_{ex}} = \frac{\sigma_{iy}}{\sigma_{ey}} = \frac{\sigma_{iz}}{\sigma_{ez}} \tag{2.25}$$

and

$$\lambda = \sqrt{R_{\mathrm{m}}/(1+k)\beta}\,, \quad R = \sqrt{x^2/\sigma_{ix} + y^2/\sigma_{iy} + z^2/\sigma_{iz}} \tag{2.26}$$

where I_s is the amplitude of the point current source in interstitial space, σ_{ql}, with $q = i, e$ and $l = x, y, z$, is the conductivity along three principal axes for the intracellular and the interstitial spaces, respectively, k represents the equal anisotropy

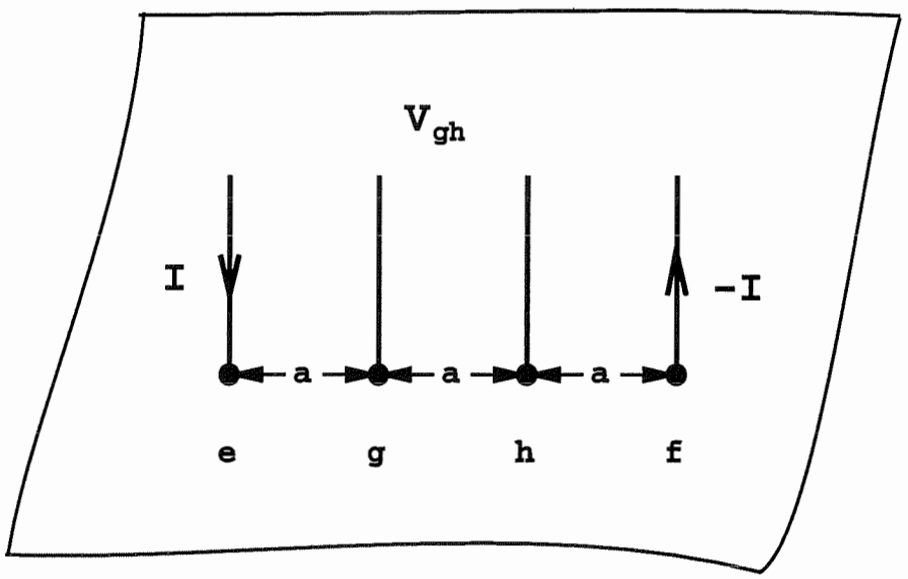

Figure 2.4: Four-electrode device for impedance measurement. Current I is passed between outer electrodes e and f, and potential is measured between inner electrodes g and h. Interelectrode spacing **a** is constant.

ratio of the tissue, $R_{\rm m}$ the membrane resistivity ($\Omega \cdot cm^2$), β the surface-to-volume ratio which links the membrane current $I_{\rm m}$ and the transmembrane potential $V_{\rm m}$ by $I_{\rm m} = \beta(V_{\rm m}/R_{\rm m})$, λ the space constant of the tissue, and R normalized distance between the source and field points.

Let l represent any of the coordinate directions, $\mathbf{a}$ the spacing between the electrodes, $\Delta\phi_{el}$ the interstitial voltage measured by the inner electrodes along the l direction, and $\Delta\phi_{il}$ the voltage measured intracellularly, then the following equations are obtained based on Eqs (2.23) and (2.24):

$$\frac{\Delta\phi_{el}}{I_s} = \frac{\sqrt{\sigma_{il}}}{4\pi\mathbf{a}\sigma}\frac{k}{1+k}\left\{1 + k\left[2exp\left(\frac{-\mathbf{a}}{\lambda_l}\right) - exp\left(\frac{-2\mathbf{a}}{\lambda_l}\right)\right]\right\} \tag{2.27}$$

and

$$\frac{\Delta\phi_{il}}{I_s} = \frac{\sqrt{\sigma_{il}}}{4\pi\mathbf{a}\sigma}\frac{k}{1+k}\left\{1 - 2exp\left(\frac{-\mathbf{a}}{\lambda_l}\right) + exp\left(\frac{-2\mathbf{a}}{\lambda_l}\right)\right\} \tag{2.28}$$

where $\lambda_l = \sqrt{\sigma_{il}}\,\lambda$. When $\mathbf{a} \ll \lambda_l$, the exponential term $exp(-\mathbf{a}/\lambda_l) \rightarrow 1$, according to Eq.(2.28), $\Delta\phi_{il} \rightarrow 0$, and Eq.(2.27) becomes

$$\frac{\Delta\phi_{el}}{I_s} \approx \frac{k}{4\pi\mathbf{a}}\frac{\sqrt{\sigma_{il}}}{\sigma}\,. \tag{2.29}$$

If the electrodes are placed along the x axis, the subscript l in above equation is replaced by x. Substituting σ and k as defined in Eq.(2.25) and linking $\Delta\phi_{ex}$ directly to the interstitial conductivity, this equation becomes

$$\sqrt{\sigma_{ey}\sigma_{ez}} = \frac{I_s}{4\pi\mathbf{a}\Delta\phi_{ex}}\,. \tag{2.30}$$

By changing the orientation of the electrodes to the y or z direction, respectively, and making measurements with the same electrode spacing yields

$$\sqrt{\sigma_{ex}\sigma_{ez}} = \frac{I_s}{4\pi \mathbf{a}\Delta\phi_{ey}}, \quad and \quad \sqrt{\sigma_{ex}\sigma_{ey}} = \frac{I_s}{4\pi \mathbf{a}\Delta\phi_{ez}}. \tag{2.31}$$

Solving Eqs (2.30) and (2.31) simultaneously will give unique values for σ_{ex}, σ_{ey} and σ_{ez}. In summary, the interstitial conductivity in each direction can be determined by measuring the voltage between the inner electrodes, provided that the interelectrode distance is much smaller than the space constant of the tissue in that direction.

For the intracellular conductivities, considering $\mathbf{a} \gg \lambda_l$, the term $exp(-\mathbf{a}/\lambda_l) \rightarrow 0$, so that Eqs (2.27) and (2.28) are equal to

$$\frac{\Delta\phi_{ql}}{I_s} = \frac{\sqrt{\sigma_{il}}}{4\pi \mathbf{a}\sigma}\left(\frac{k}{1+k}\right) \tag{2.32}$$

where $q = i, e$ can represent either the intracellular or the interstitial medium. If the electrodes are oriented along the x axis, for the intracellular medium, the above equation becomes:

$$\sqrt{\sigma_{iy}\sigma_{iz}} = \frac{I_s}{4\pi \mathbf{a}\Delta\phi_{ix}}\left(\frac{k}{1+k}\right),$$

for the interstitial medium, it is

$$\sqrt{\sigma_{ey}\sigma_{ez}} = \frac{I_s}{4\pi \mathbf{a}\Delta\phi_{ex}}\left(\frac{1}{1+k}\right).$$

Since $\Delta\phi_{ix} = \Delta\phi_{ex}$, adding the two equations, we have

$$\sqrt{\sigma_{iy}\sigma_{iz}} + \sqrt{\sigma_{ey}\sigma_{ez}} = \frac{I_o}{4\pi \mathbf{a}\Delta\phi_x}. \tag{2.33}$$

In the same way, we can obtain the following expressions by putting the electrodes along the y and z axes, respectively:

$$\sqrt{\sigma_{ix}\sigma_{iz}} + \sqrt{\sigma_{ex}\sigma_{ez}} = \frac{I_o}{4\pi \mathbf{a} \Delta\phi_y} \tag{2.34}$$

and

$$\sqrt{\sigma_{ix}\sigma_{iy}} + \sqrt{\sigma_{ex}\sigma_{ey}} = \frac{I_o}{4\pi \mathbf{a} \Delta\phi_z} \, . \tag{2.35}$$

As the interstitial conductivity components have been obtained from measurements under the assumption $\mathbf{a} \ll \lambda_l$, the intracellular conductivities can be determined independently from the above procedures.

The intracellular and interstitial potentials are identical under the last condition, and either Eq.(2.27) or Eq.(2.28) can be used to characterize the impedance measurements in this case. Since Eq.(2.28) goes to zero when $\mathbf{a} \ll \lambda_l$, only Eq.(2.27) is needed to represent the bidomain model impedance measurements with the four-electrode technique. For the general utilization, the subscript e is eliminated from the equation so that

$$\frac{\Delta\phi_l}{I_s} = \frac{\sqrt{\sigma_{il}}}{4\pi \mathbf{a} \sigma} \frac{k}{1+k} \left\{ 1 + k \left[2exp\left(\frac{-\mathbf{a}}{\lambda_l}\right) - exp\left(\frac{-2\mathbf{a}}{\lambda_l}\right) \right] \right\} \, . \tag{2.36}$$

This is the formula which is often seen in the literature [62].

2.3.2 Sinusoidal stimulation

The above measurement procedure involves repeating the current injection along the different axes, first with small and then with larger interelectrode distances. In some practical experiments, the space between electrodes is fixed [46] and an

alternative approach is needed to apply the four-electrode technique. One solution is to use *a.c.* current stimulation. In this case the space constant of a cardiac bundle, λ, is [33]:

$$\lambda_0 = \sqrt{\frac{b\,R_{\rm m}}{2\,[\rho_i + \beta\,\rho_e]}} \tag{2.37}$$

and

$$\lambda(\omega) = \sqrt{\frac{b\,Z_{\rm m}}{2\,[\rho_i + \beta\,\rho_e]}}\,, \tag{2.38}$$

where ω is the angular frequency, b the radius of fibers in the bundle, ρ_i the intracellular resistivity, β the ratio of the intracellular and interstitial cross-sectional areas, ρ_e the interstitial resistivity, $R_{\rm m}$ the membrane resistance, and $Z_{\rm m}$ the membrane impedance defined by

$$Z_{\rm m} = \frac{R_{\rm m}}{1 + j\omega R_{\rm m} C_{\rm m}} \tag{2.39}$$

Substituting $Z_{\rm m}$ into Eq.(2.38):

$$\lambda(\omega) = \lambda_0 \sqrt{\frac{1 - j\omega R_{\rm m} C_{\rm m}}{1 + \omega^2\,R_{\rm m}^2\,C_{\rm m}^2}}\,. \tag{2.40}$$

Considering that the attenuation of the potential difference between measurement electrodes is dependent on λ_l (*e.g.* Eq.(2.36)), in the case of sinusoidal stimulation, only the real part of $\lambda(\omega)$ is useful in relation to the four-electrode impedance measurements. We use $Re(\lambda_\omega)$ to denote the real part of $\lambda(\omega)$ in the following discussion. Theoretically, $Re(\lambda_\omega) \rightarrow \lambda_0$ at low frequency and decreases as the frequency increases. For a fixed interelectrode spacing, $\mathbf{a}$, and as long as $\mathbf{a} \ll \lambda_0$ at low frequency, one has $\mathbf{a} \gg Re(\lambda_\omega)$ if the frequency is high enough. In this case the interstitial conductivities will be determined by Eqs (2.30) and (2.31)

at low frequencies (where $\mathbf{a} \ll Re(\lambda_\omega)$), and the intracellular conductivities can be obtained from Eqs (2.33) to (2.35) at higher frequencies (where $\mathbf{a} \gg Re(\lambda_\omega)$).

In other words, because the membrane impedance ($R_\mathrm{m} \| C_\mathrm{m}$) is very high at low frequency due to very high value of R_m, the current flow is restricted to the interstitial space. Then the potential measured by the inner electrode pair depends only on the interstitial conductivities. When the signal frequency increases, the impedance $R_\mathrm{m} \| C_\mathrm{m}$ decreases and more and more current flow through the membrane into the intracellular medium. If the frequency is high enough, the amount of current going into the cells cannot be ignored, and the potential measured by the two inner electrodes reflects the combined intracellular and interstitial conductivities. The advantage of this method is that high spatial resolution can be achieved by keeping the interelectrode spacing as small as possible.

Chapter 3

Action Potential Propagation in a Tissue Bundle

There are two main factors which affect the propagation of the action potential wavefront in cardiac tissue. One is the set of membrane properties governing the flow of membrane current, including ionic channel kinetics, active transport processes, and ionic concentration gradients. The other is the tissue conductivity regulating the flow of axial current, as determined by the microstructural organization of the tissue, including the number of cellular interconnections and the packing density of cells.

There is a great deal of recent evidence to suggest that the characteristics of propagating cardiac action potentials do not match the predictions of linear cable theory. The curved wavefronts described in strands of cardiac muscle [83] are believed to be associated with larger interstitial potentials at the center of the strand [34, 71]. It has been shown also [45] that current flow into the interstitial space can modify the conduction velocity, the shape of the action potential and the anisotropic

conductivities. These factors are governed by the microstructure of the bundle. This influence on the conduction properties and shape of the propagated action potential is examined in this chapter.

3.1 Packing density of the bundle

The structure of the cardiac bundle model used in our simulations is shown in Fig.2.2 and 2.3. The bundle is composed of several identical cylindrical fibers, hexagonally packed in radial layers. To investigate the effects of the bundle organization on wavefront propagation, we changed the radius of the fibers in the bundle, the distance between fibers, and the number of fibers. The bundle radius and the number of fibers are determined by the number of radial layers. This number was limited by the storage capacity of the computer used in our simulations (a Silicon Graphics 4D-280 computer server). The largest bundle we could simulate was composed of 169 fibers arranged into 8 radial layers.

In the bidomain model, the fiber packing density is represented by f_i: the fraction of the bundle cross-section occupied by the intracellular space. In many cases, f_i is equivalent to the intracellular volume fraction [70]. In our simulations, the volume fraction f_i is controlled by D, the distance between fibers (see Fig.2.3), through the following equation:

$$f_i = \frac{\pi N_f}{6\, sin(\pi/6)\, cos(\pi/6)\, [(nr - 1/2)\, D]^2}$$

where N_f is the number of fibers in the bundle and nr is the number of radial layers. The relation between the bundle surface-to-volume ratio (β) and f_i is given by

Table 3.1

Physical parameters		
fiber radius	b (μm):	5
fiber length	l (mm) :	3
number of radial layers	n_r:	8
number of fibers in the bundle	N_f:	169
intracellular volume fraction	f_i:	0.75
Electrical parameters		
intracellular conductivity	$\sigma_i(m\mho/cm)$:	5.0
interstitial conductivity	$\sigma_e(m\mho/cm)$:	66.66
membrane capacitance	$C_{\mathrm{m}}(\mu F/cm^2)$:	1.0

Table 3.1: Physical and electrical parameters of the bundle

$$\beta = \frac{2f_i}{b}$$

where b is the fiber radius.

3.2 Conduction properties of activation wavefront

3.2.1 Transmembrane potential V_{m}

The physical and electrical parameters of the bundle model, based on the previous work [10, 40], are presented in Table 3.1. Although we used various tessellations in the verification process, for all of the simulations described in this Chapter, each fiber was discretized into 504 patches, 480 identical cylindrical patches and 24

planar end patches. The discretized cylindrical patch length, Δx, was $75\mu m$, each patch had a 30 degree arc. According to Sommer's observations [78] that the length of cardiac ventricular working myocytes are between $30 \sim 130\,\mu m$ and that most of them make at least one contact with a neighboring cell laterally, we included transverse resistive connections of $2M\Omega$ at every $150\mu m$ on the bundle. The bundle was stimulated at its proximal end with a pair of extracellular point electrodes applied near the bundle surface (see Fig.2.2). Representative action potential wavefronts are shown in Fig.3.1, we assume that the intracellular potential ϕ_i is a constant inside a cell. The action potential at the surface of the bundle at the proximal end is contaminated by the stimulus artifact (large negative deflection). While the wavefront stabilizes within $2\,msec$, there remains a significant difference in the shape of the action potential at the center and at the surface of the bundle during stable propagation.

A map of the transmembrane potential V_{m} at one instant in time (during stable propagation) is shown in Fig.3.2. Red corresponds to high values of V_{m} (above $25\,mV$), with the potential close to the resting value (less than $-75\,mV$) represented by blue. It was found that the distribution of action potentials in the bundle is three-dimensional, which means that changes in V_{m} not only occur in the longitudinal direction, but also in the transverse direction. The distribution of transmembrane potential in a cross-section perpendicular to the bundle axis is illustrated in Fig.3.3. The variation from red to blue is $10\,mV$. The cross-section shown in this figure exhibits a variation of about $7 \sim 8\,mV$. This supports the previous

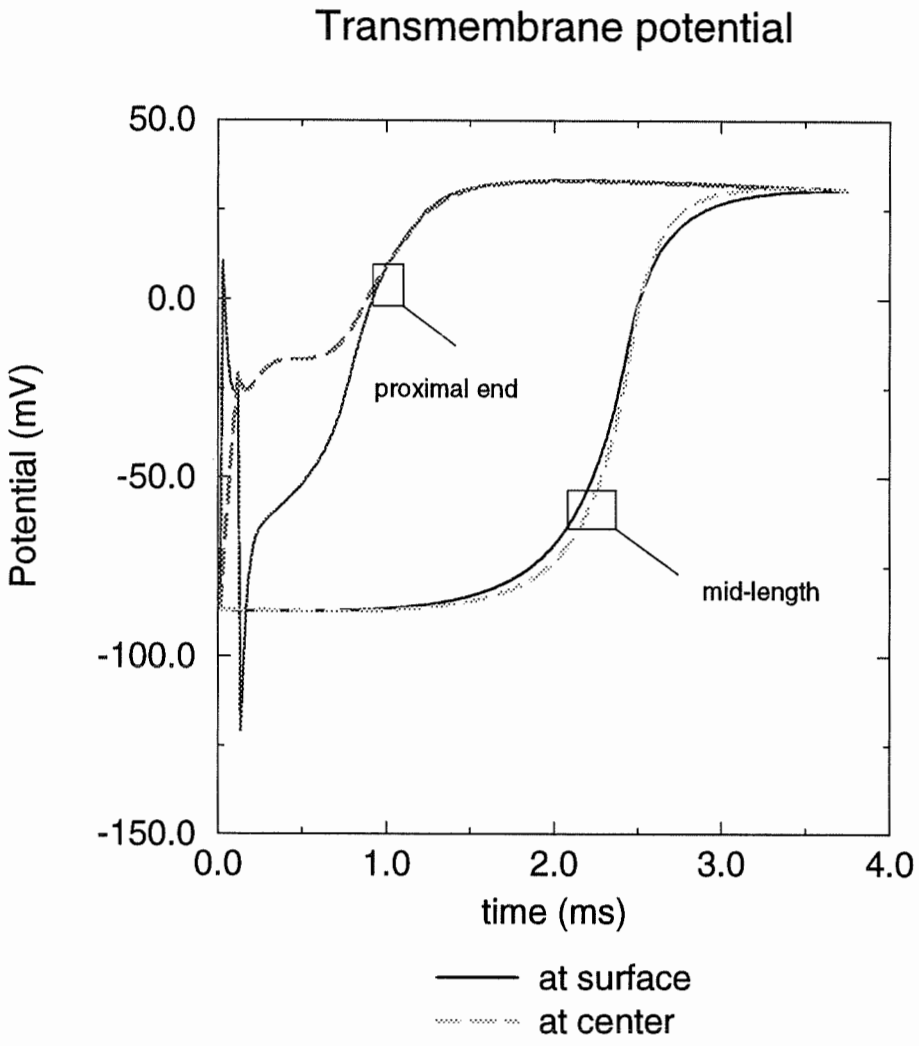

Figure 3.1: Two pairs of transmembrane potential recordings at two locations on the bundle. One recording is at the center (broken curve) and the other at the surface (solid curve) of the bundle.

assertions [34, 71, 83] that, even in this relatively thin bundle, the propagating wave front is curved.

3.2.2 Interstitial potential ϕ_e

The bidomain simulations suggest that changes in V_{m} from the center to the surface of the bundle (Fig.3.1 and Fig.3.3) are caused by the interstitial potential ϕ_e [34, 71]. This is in agreement with the result of Fig.3.4 a) where ϕ_e is seen to vary significantly from the center to the surface of the bundle, while the intracellular potential ϕ_i remains unchanged (Fig.3.4 b).

The deviation of ϕ_e at the center from that the surface of the bundle is evident as a function of time and of space. Figs 3.5 and 3.6 show the distribution of ϕ_e along the bundle at a specific time instant, at various radial positions with 4 different intracellular volume fractions. It is important to note that the change in ϕ_e with depth (Fig.3.5) is similar to its variation with packing density (Fig.3.6). That is ϕ_e at the bundle surface ($r = 82.5\,\mu m$) is similar to that at low f_i values (loose packing density), and *vice versa*. This link between ϕ_e, the packing density and radial distance can also be seen by comparing Fig.3.6 with the behavior of a much thicker (radius of $5mm$) cardiac strand (Henriquez [34], Fig.3).

These results suggest that one may use a small bundle to study changes in transmembrane potential occurring in a large bundle. In this case the tight packing density corresponds to the center of the large bundle, and the loose packing to its

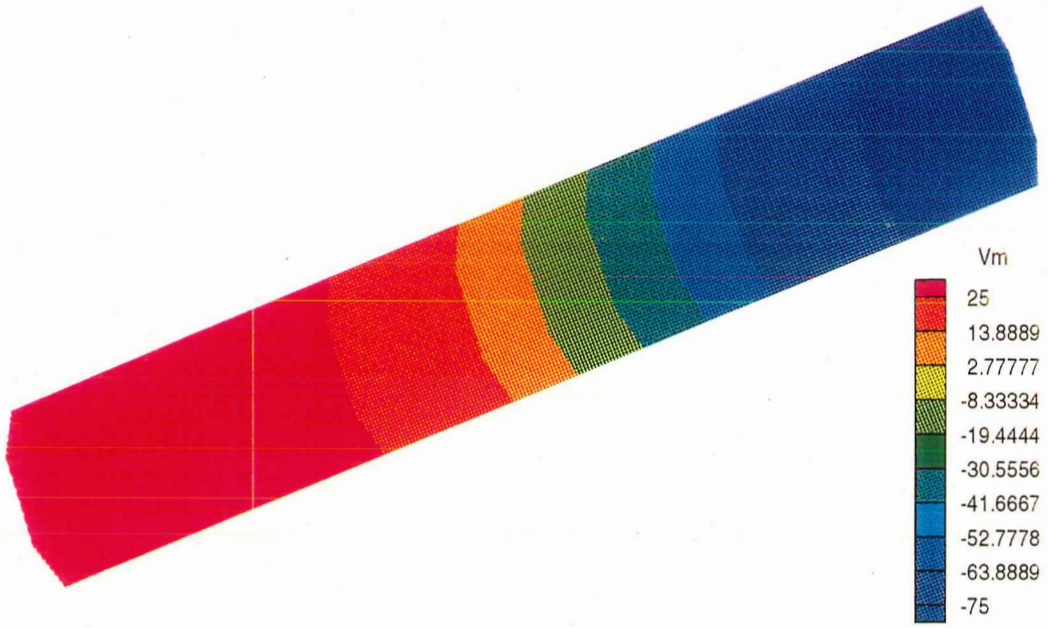

Figure 0.1: Distribution of transmembrane potentials along the bundle. The recording was taken at a randomly chosen time instant during stable propagation.

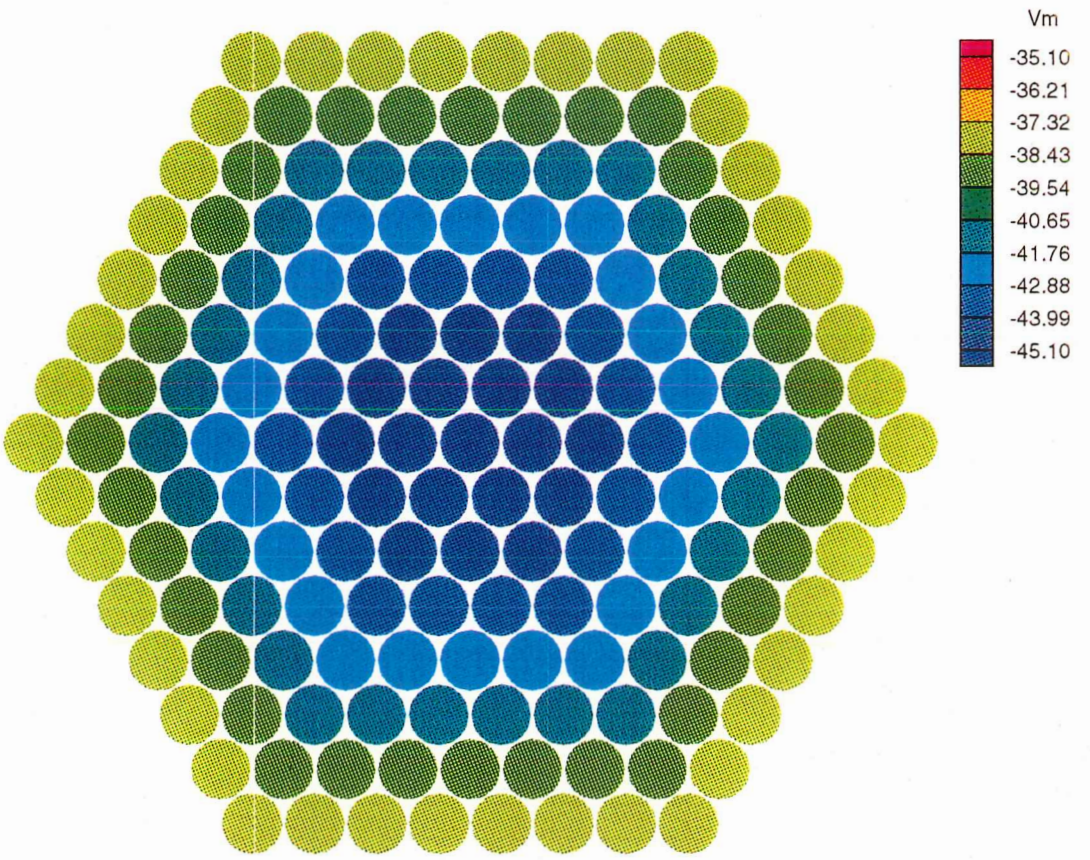

Figure 0.2: Distribution of transmembrane potentials on a cross-section of the bundle during stable propagation. Colors from blue to red corresponds to 10 mV variation. At this cross-section the variation of the membrane potential is about $7 \sim 8\,mV$.

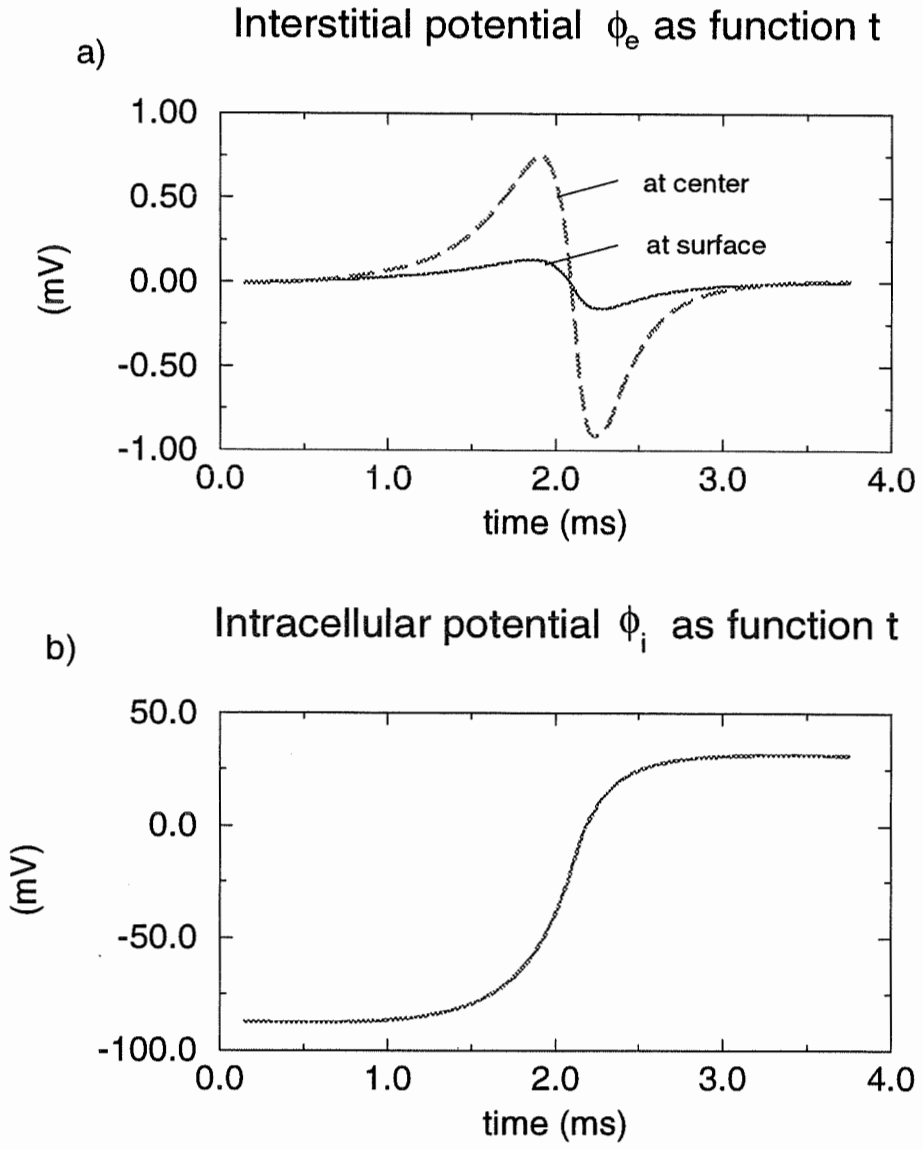

Figure 3.4: Interstitial potential ϕ_e and intracellular potential ϕ_i as function of time during stable propagation (at mid-length). The solid and broken curves correspond to recordings at the surface and the center of the bundle, respectively.

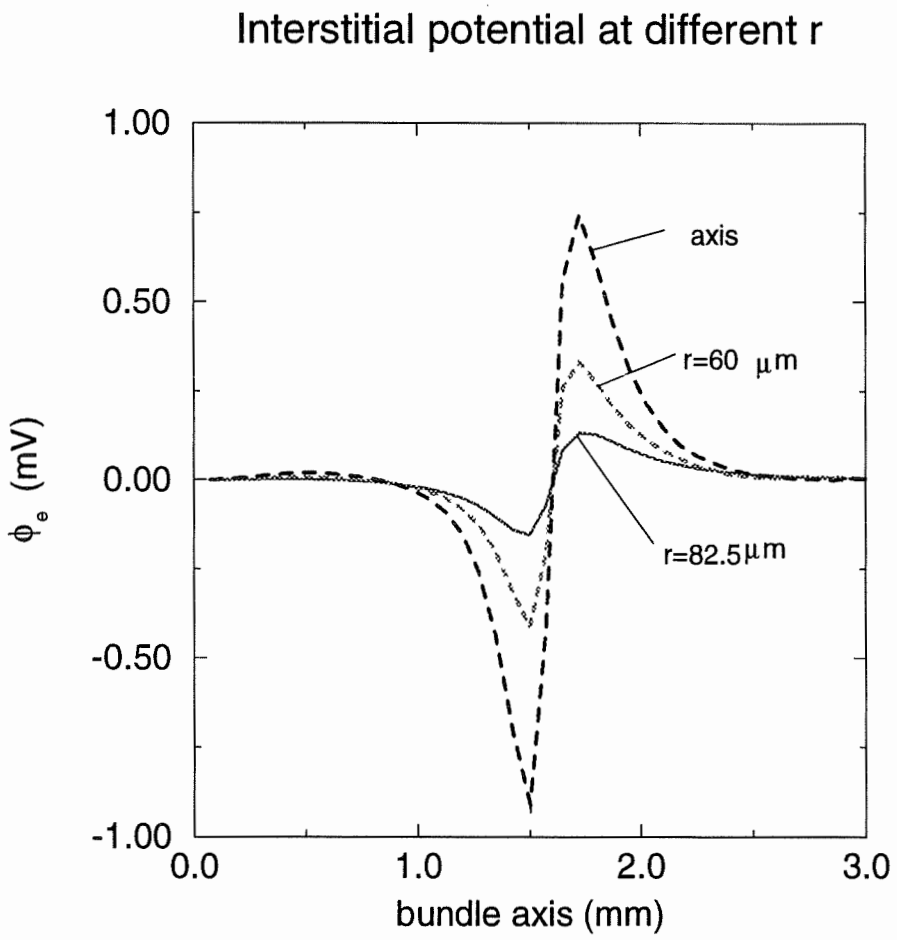

Figure 3.5: The interstitial potential distribution along the bundle for different radial positions and $f_i = 0.75$ at a specific time instant. $r = 82.5\mu m$ corresponds to the bundle surface.

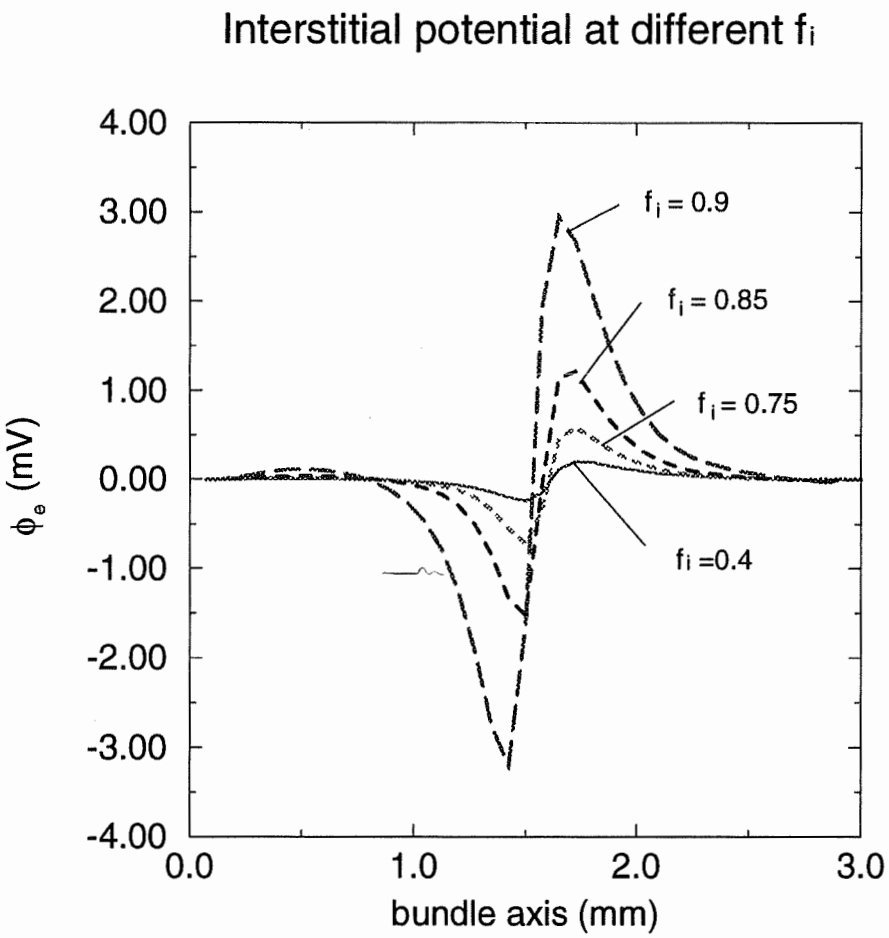

Figure 3.6: The distribution of interstitial potential (ϕ_e) at the center along the bundle axis for different values of the intracellular volume fraction f_i, measured at the same time instant.

surface, *i.e.* ϕ_e increases similarly as you move towards the center or as you increases f_i.

3.2.3 Conduction Velocity

Fig.3.7 shows the relationships between the propagation velocity and intracellular volume fraction f_i. The broken curve corresponds to the bundle and the solid curve to a single fiber of the same radius. For very low f_i values (loosely packed fibers), the conduction velocity approaches the single fiber limit. As f_i increases, the conduction velocity of the bundle decreases. This behavior agrees with published results [34, 71] where f_i was varied by changing the number of cells in the strand, while holding the bundle radius constant. To compare our results with those of the bidomain model, we varied f_i by changing the number of fibers in the bundle. The two simulations yielded almost identical results.

We found that the conduction velocity varied from $63.3\,cm/sec$ at $f_i = 0.4$ to $60.2\,cm/sec$ at $f_i = 0.9$. This variation is smaller than that predicted by Roth [71] who observed $65\,cm/sec$ at $f_i = 0$ and $40\,cm/sec$ at $f_i = 1$. This discrepancy can be explained, in part, by the different parameters used in the two models, such as bundle size, the intracellular and interstitial conductivity values, membrane parameters and so on.

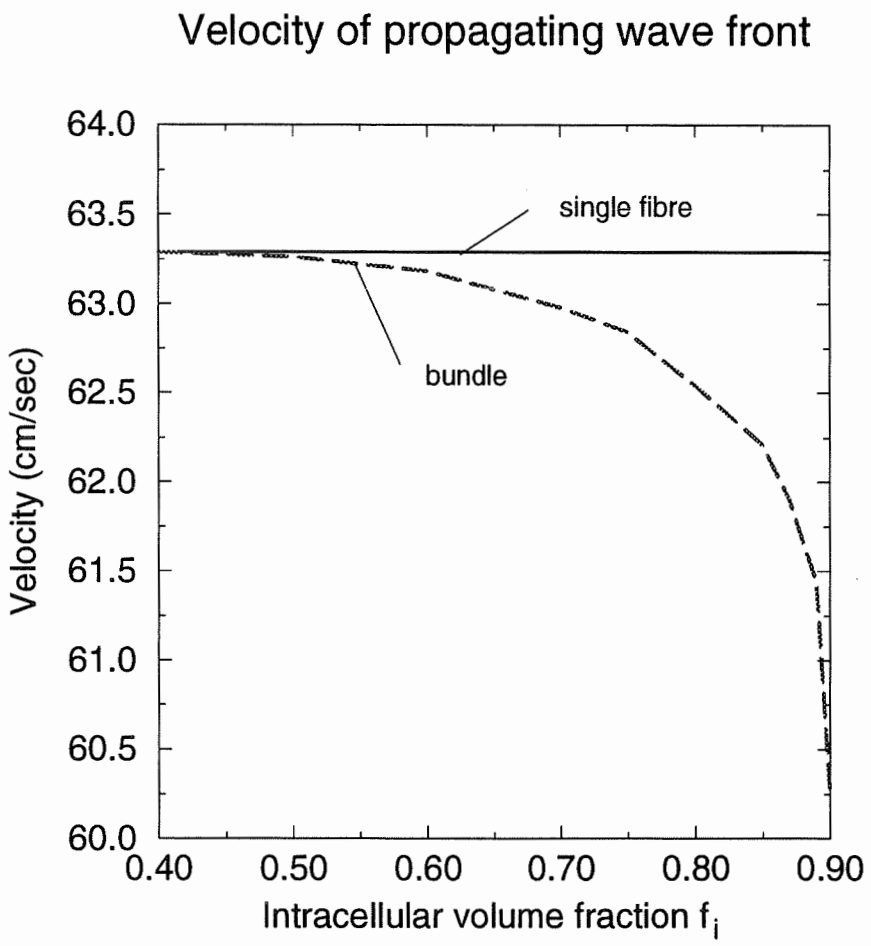

Figure 3.7: Conducting velocity as function of f_i for bundle (broken curve) and single fibre (solid curve). The fiber radius is $0.5\,\mu m$. The bundle radius varies from $62.5\,\mu m$ to $82.5\,\mu m$ corresponding to the variation of f_i.

3.3 The action potential upstroke

The action potential upstroke is usually described by two parameters, $\dot{V}_{max}$ and τ_{foot}. $\dot{V}_{max}$ is the maximum rate of rise and τ_{foot} is the time constant of the foot of the action potential. In our simulations, $\dot{V}_{max}$ was calculated using a difference formula with Matlab (The Math Works Inc., South Natick, MA.) and τ_{foot} was obtained using a numerical curve fitting algorithm [18, 19].

Fig.3.8 shows τ_{foot} and $\dot{V}_{max}$ as a function of the transverse position in the bundle during stable propagation. We can see that τ_{foot} is almost constant in the radial direction, even near the bundle surface. $\dot{V}_{max}$ decreases from the center to the bundle surface. The decrease of $\dot{V}_{max}$ near the surface implies that the high extracellular conductivity has a significant influence. The estimated τ_{foot} and $\dot{V}_{max}$ values are comparable to those obtained by Roth [71] at the center of the bundle. At the bundle surface, these values are far from those predicted by the bidomain model.

Variations of $\dot{V}_{max}$ from the center to the surface increase as the packing density increases, as illustrated in Fig.3.9 b). Meanwhile, τ_{foot} remains constant along the radial direction, even at very tight packing density as seen in Fig.3.9 a). This indicates that the high packing density increases the difference in the rate of rise of the action potential between the center and the surface of the bundle.

Figure 3.10 shows τ_{foot} a) and $\dot{V}_{max}$ b) plotted as a function of the intracellular volume fraction f_i at center and at surface. τ_{foot} varies proportionally with f_i at the center and surface of the bundle, and there is a dramatic increase at very

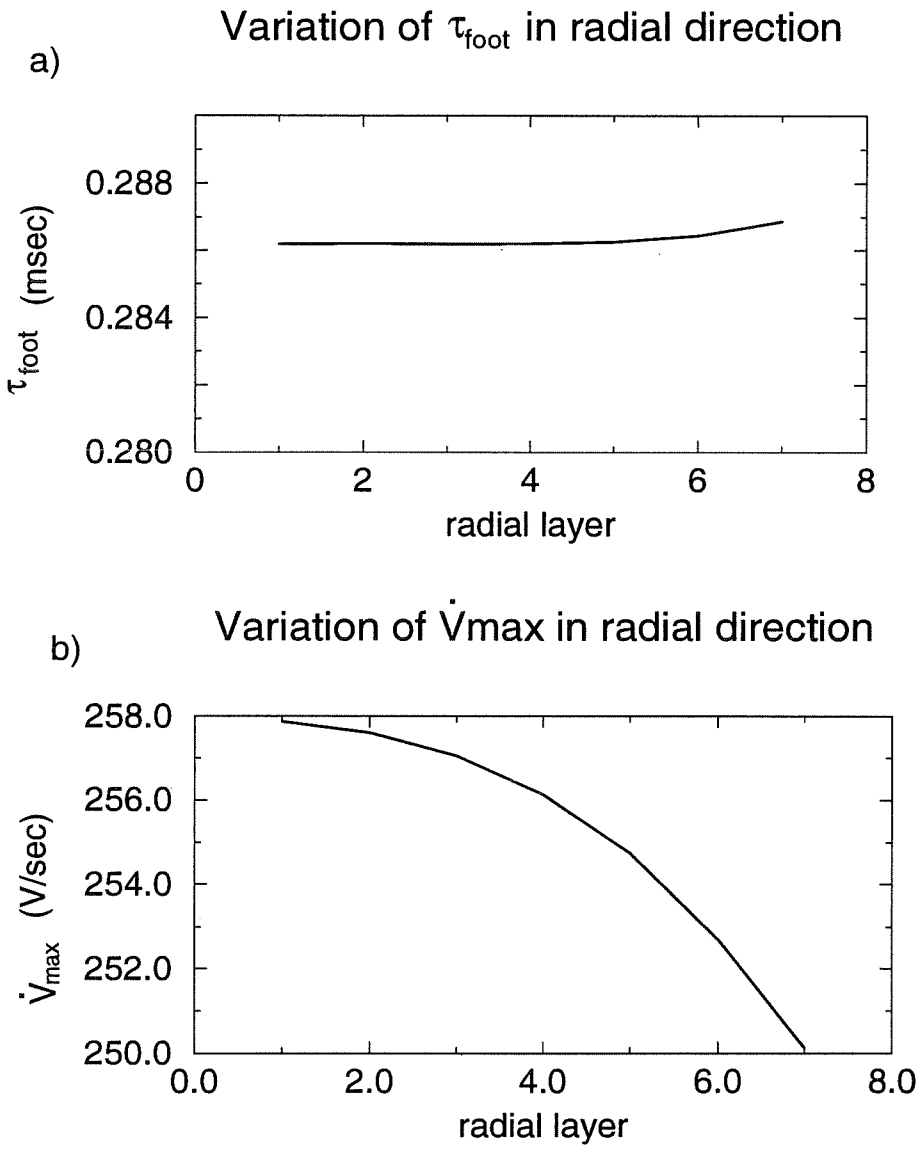

Figure 3.8: Variations of τ_{foot} a) and $\dot{V}_{max}$ b) with radial distance. The abscissa indicates the number of radial layers of the bundle, from the center (left) to the surface (right) of the bundle ($f_i = 0.75$).

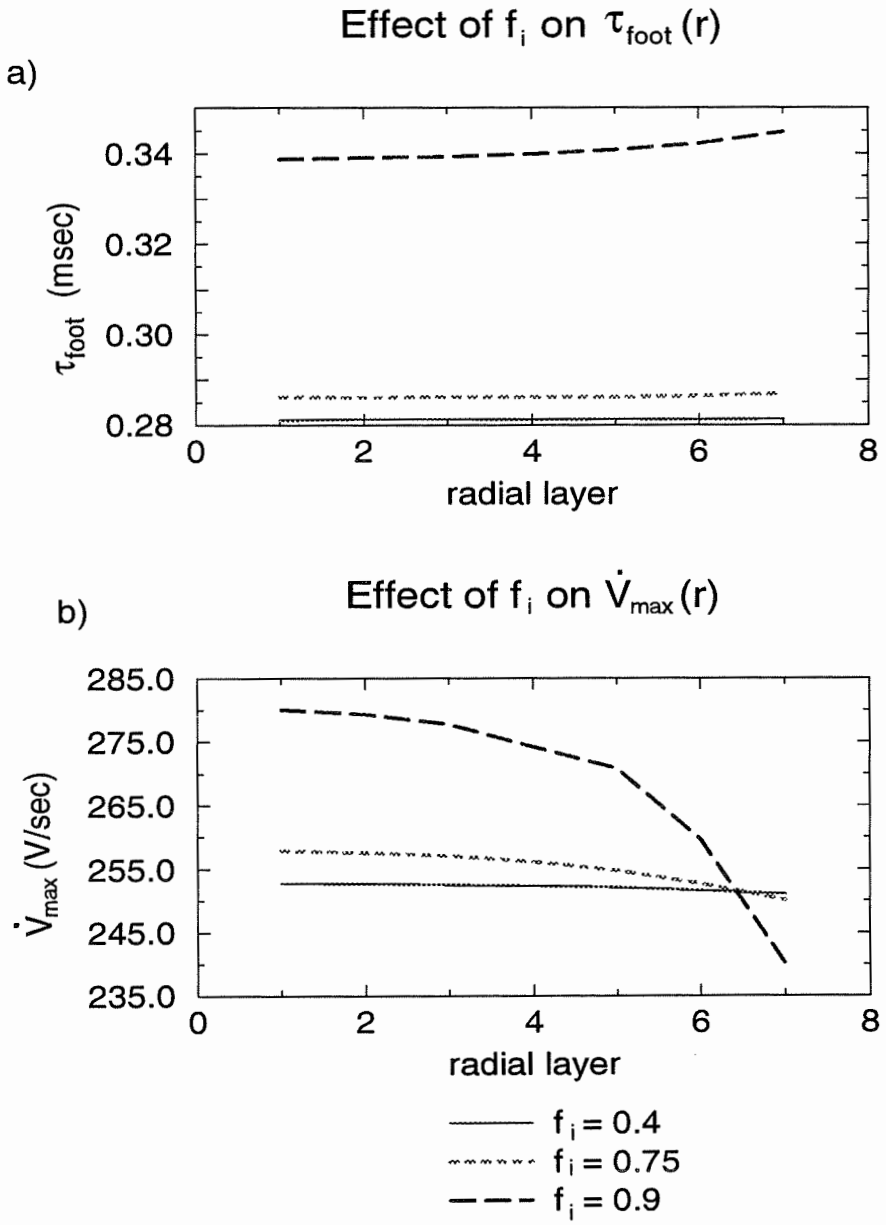

Figure 3.9: The effect of the intracellular volume fraction f_i on τ_{foot} a) and $\dot{V}_{max}$ b) with radial distance r. The abscissa is the same as in Fig.3.8.

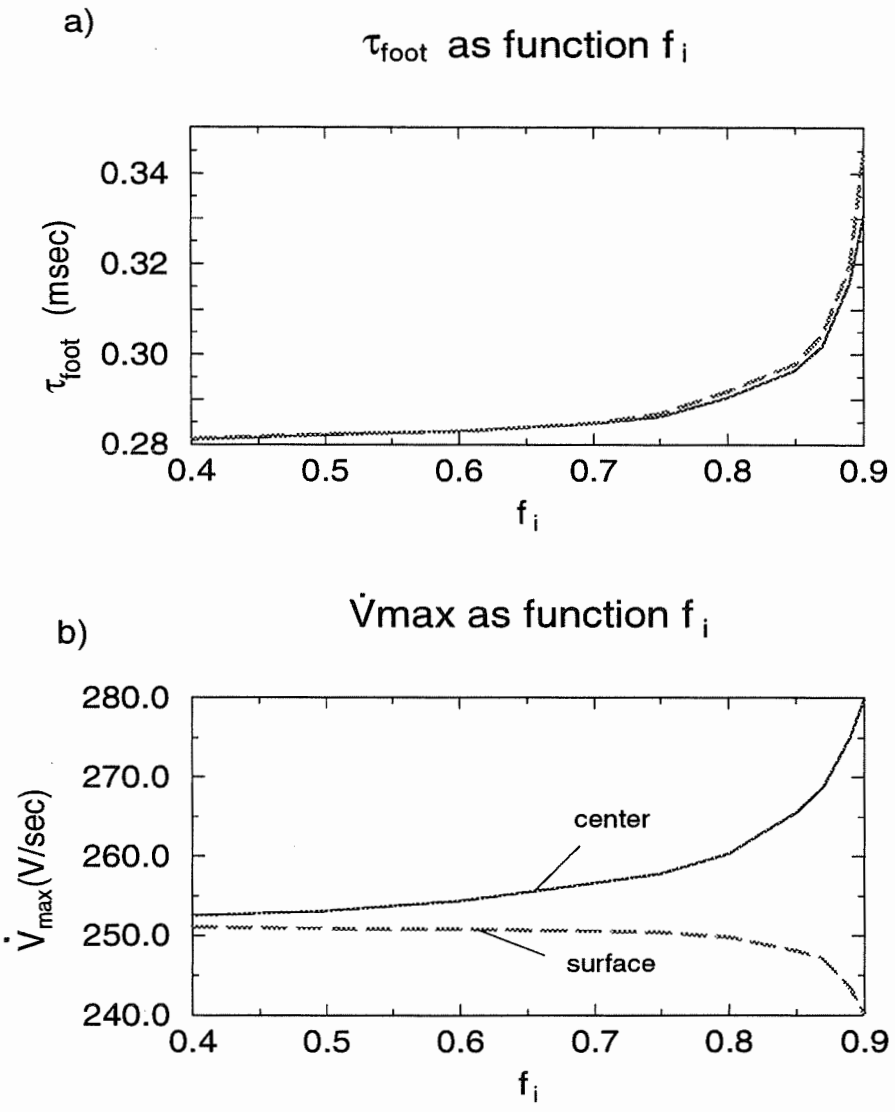

Figure 3.10: τ_{foot} a) and $\dot{V}_{max}$ b) as function of f_i at the center (solid curve) and surface (broken curve) of the bundle.

tight packing density. The direction of change of $\dot{V}_{max}$ with the packing density are opposite at the center and at surface of the bundle. Here we also observe an abrupt increase or decrease of $\dot{V}_{max}$ as the packing density approaches unity.

To further investigate these variations in $\dot{V}_{max}$, we measured $d\phi_e/dt_{max}$ (Fig.3.11 a) and $d\phi_i/dt_{max}$ (Fig.3.11 b) as function of f_i at the center and at the surface of the bundle. The absolute value of $d\phi_i/dt_{max}$ for most packing densities is much larger than that of $d\phi_e/dt_{max}$, it yields

$$\dot{V}_{max} = \frac{d\phi_i}{dt}_{max} - \frac{d\phi_e}{dt}_{max} \approx \frac{d\phi_i}{dt}_{max}.$$

Thus $\dot{V}_{max}$ is dominated by $d\phi_i/dt_{max}$ when $f_i < 0.8$ for both surface and center. As the packing density increases, both values of $d\phi_i/dt_{max}$ and $|d\phi_e/dt_{max}|$ decrease. At the surface, there is only minor increase in $|d\phi_e/dt_{max}|$, and because it is so small compared to $d\phi_i/dt_{max}$, it doesn't affect $\dot{V}_{max}$. When $f_i > 0.8$, the change in $|d\phi_e/dt_{max}|$ at the center of the bundle is larger than the change in $d\phi_i/dt_{max}$ (see Fig.3.11), so that $d\phi_e/dt_{max}$ modifies the behavior of $\dot{V}_{max}$ at the center. In this case

$$\dot{V}_{max} = \frac{d\phi_i}{dt}_{max} - \frac{d\phi_e}{dt}_{max} = \frac{d\phi_i}{dt}_{max} + \left|\frac{d\phi_e}{dt}_{max}\right|.$$

The dramatic increase in $|d\phi_e/dt_{max}|$ at the center of the bundle when the packing density is high ($f_i > 0.8$) is caused by the large peak-to-peak value of ϕ_e (see Fig.3.6). At loose packing ($f_i = 0.4$), the peak-to-peak value of ϕ_e is about $0.8\,mV$, whereas it increases approximately 10 times as the packing density increases

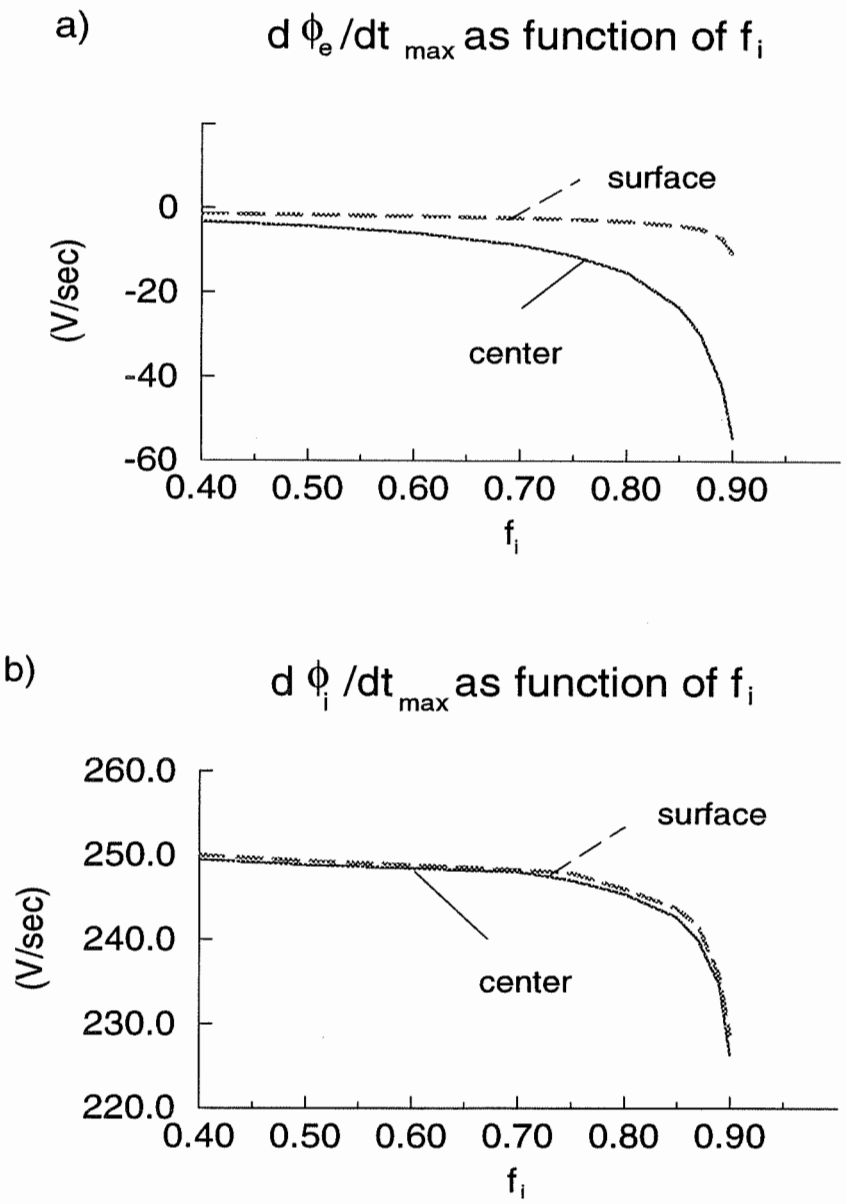

Figure 3.11: $d\phi_e/dt_{max}$ a) and $d\phi_i/dt_{max}$ b) as function of the intracellular volume fraction f_i.

to $f_i = 0.9$, meanwhile the time duration of peak-to-peak remains constant, resulting the dramatic increase in $|d\phi_e/dt_{max}|$.

3.4 Discussion

We simulated the wavefront propagation and upstroke of the action potential in a small cardiac bundle using the BEM and examined the effect of packing density on propagation and waveshape of the action potential. Our bundle consists of 8 radial layers and 169 circular cylindrical fibers. Each has been discretized into 504 pathes during simulations with $\Delta x = 75\,\mu m$. To ensure that this discretization adequate, we used smaller bundles (6 radial layers) with finer discretizations of $\Delta x = 60\,\mu m$ and $\Delta x = 50\,\mu m$. We found that the results from these simulations were consistent with those using $\Delta x = 75\,\mu m$.

Our simulation results reveal that the propagated wavefront in the bundle deviates from a plane normal to the longitudinal axis because of the restricted interstitial space. $\dot{V}_{max}$ is smaller and τ_{foot} larger at the surface than at the center of the bundle (see Fig.3.8). These observations are consistent with bidomain simulation results published by Henriquez [34], where they simulated a larger cardiac bundle representation under the assumption of equal anisotropy ratio of the intracellular and interstitial conductivities. Our results are also consistent with the experimental observations of Suenson [83], who observed these phenomena in a study of source-load interaction during impulse propagation of excited and unexcited cells in the working myocardium.

Table 3.2

Packing density	Model	$\dot{V}_{max}$ (V/sec)	τ_{foot} (m sec)	Velocity (cm/sec)
$f_i = 0.60$	Bidomain	211.0	0.32	64.2
	BEM(EJ)	200.9	0.324	63.3
	BEM(DR)	250.6	0.283	63.3
$f_i = 0.80$	Bidomain	195.2	0.48	62.1
	BEM(EJ)	199.9	0.331	62.5
	BEM(DR)	249.1	0.289	62.5

Table 3.2: Comparison between the electrical properties at surface of bundle predicted by the BEM and by the bidomain model

The conduction velocity and upstroke parameters of the action potential at the surface of the bundle for two different packing densities $f_i = 0.6$ and $f_i = 0.8$ were compared with their counterparts obtained from the bidomain model simulations published by Henriquez [34], and listed in Table 3.2. We also repeated the simulations at $f_i = 0.6$ and $f_i = 0.8$ with the Ebihara-Johnson membrane model used by Henriquez. In this table, BEM denotes the boundary element method simulations, (EJ) represents the simulations with the Ebihara-Johnson model [24] and (DR) corresponds to the Drouhard-Roberge model [23].

The two methods predict similar behavior for the upstroke of the action potential and conduction velocity as the packing density increases. The conduction velocity values obtained with the boundary element method and the two different membrane models are essentially identical. They are slightly less than those obtained with the bidomain model at $f_i = 0.6$. The values of τ_{foot} predicted by BEM

at $f_i = 0.6$ are close to those predicted by the bidomain model, but very different at $f_i = 0.8$. When the packing density increases from $f_i = 0.6$ to $f_i = 0.8$, our model predicted that τ_{foot} would increase slightly for both membrane models, whereas the bidomain model gives a much greater increase (50 %). This phenomenon also occurs with $\dot{V}_{max}$. With either membrane model, the boundary element method indicates very small decrease in $\dot{V}_{max}$ ($0.5 \sim 0.6$ %) as the intracellular volume fraction f_i increases from 0.6 to 0.8, while the bidomain model yields a much larger reduction (7.5 %). In addition, the value of $\dot{V}_{max}$ is affected greatly by the ionic membrane model (25 % lower in the EJ model), while the conduction velocity and τ_{foot} are nearly equal ($f_i = 0.6$).

Possible reasons for differences between BEM and the bidomain model with respect to the values of $\dot{V}_{max}$ and τ_{foot} may be related to the following factors:

1. Different boundary conditions at the bundle surface used by the two methods. In the boundary element method, no specific boundary condition on the bundle surface is required, since Green's theorem only requires the boundary conditions at each membrane surface and at the surface of the unbounded extracellular medium. In the bidomain model, however, there have been long standing arguments about boundary conditions. Henriquez favored the following boundary conditions [33]:

$$\phi_e(r,x)|_{r=s} = \phi_o(r,x)|_{r=s} \tag{3.1}$$

$$\sigma_{er}\frac{\partial \phi_e}{\partial r}\bigg|_{r=s} = \sigma_o \frac{\partial \phi_o}{\partial r}\bigg|_{r=s} \tag{3.2}$$

and

$$\sigma_{ir} \frac{\partial \phi_i}{\partial r} |_{r=s} = 0 \tag{3.3}$$

where subscript o refers to the surrounding extracellular medium, s is the boundary between the bidomain bundle and monodomain 'bathing' space. Other investigators used alternative boundary conditions [63, 67], which usually produced different values for $\dot{V}_{max}$ and τ_{foot} [71].

2. The restriction of equal anisotropy ratio of the intracellular and interstitial resistivities in the bidomain simulations.

3. The different values of anisotropic resistivities used in the two methods. Henriquez assumed $\rho_{ir} = 1200\,\Omega\,cm$, $\rho_{ix} = 400\,\Omega\,cm$, $\rho_{er} = 150\,\Omega\,cm$ and $\rho_{ex} = 50\,\Omega\,cm$ for both $f_i = 0.6$ and $f_i = 0.8$ cases. In our simulations (see Chapter 4 and 5), we found $\rho_{ex} = 56\,\Omega\,cm$, $\rho_{er} = 110\,\Omega\,cm$, $\rho_{ix} = 285\,\Omega\,cm$ and $\rho_{ir} = 1330\,\Omega\,cm$ for $f_i = 0.6$, and $\rho_{ex} = 76\,\Omega\,cm$, $\rho_{er} = 227\,\Omega\,cm$, $\rho_{ix} = 245\,\Omega\,cm$, $\rho_{ir} = 1340\,\Omega\,cm$ for $f_i = 0.8$.

4. The effect of the bundle size, which is much larger in the bidomain than in BEM simulations, and fiber radius.

It should be emphasized that the bidomain simulation results presented in Table 5.3 were obtained assuming the equal anisotropy ratio condition. In recent work, Pollard *et al.* [64] and Henriquez [35] have simulated the propagation behavior of the cardiac tissue using the bidomain model with the equal anisotropy ratio, the nominal anisotropy ratio and the reciprocal anisotropy ratio. They found that the

behavior ahead of the wavefront for the nominal anisotropy simulation was different from the behavior ahead of the wavefront for the equal anisotropy case. The behavior in the upstroke region was similar in both cases, and the propagation velocities in longitudinal and transverse directions were also essentially same for two cases. The most striking differences between the potential distributions from the reciprocal anisotropy simulation and the other two simulations were regions of hyperpolarization ahead of isopotential line $V_{\mathrm{m}} = -80\,mV$, the propagation velocities in the two perpendicular directions were the same, however, there was additional influence of the interstitial volume conductor on the foot of the action potential during depolarization. They concluded that the major waveform shape changes caused by the interstitial volume conductor with unequal anisotropy ratios were confined to the foot of the action potential. In general τ_{foot} for unequal anisotropy ratios was higher than when the equal anisotropy ratio condition was assumed, the upstroke of the action potential $\dot{V}_{max}$ and the variation of conduction velocities were similar for both equal and nominal anisotropy ratios.

Remember that the above comparisons were carried out at the surface of the bundle. Both simulation and experimental results [71, 83] have shown that the upstroke of the propagating action potential at the surface differ from those at the center of the bundle. There is, however, no experimental information available on how the upstroke of an action potential at the center of the bundle varies with the packing density. In our simulations, we observed that the difference in the upstroke between the center and the surface of the bundle was very significant at higher pack-

ing density (see Fig.3.9 and Fig.3.10). This difference is reflected in the parameter $\dot{V}_{max}$. Since there is little difference in τ_{foot} between the center and the surface, both increase when the packing density increases. However, as the packing density increases, $\dot{V}_{max}$ at the center of the bundle varies in the direction opposite to that at the bundle surface (see Fig.3.10 b). This is caused by the interstitial potential, which is negligible at the bundle surface, but very large at the center of the bundle, especially when the packing is tight (see Fig.3.11).

The packing density used in our simulations varies from $f_i = 0.4$ to $f_i = 0.9$. In the early 70's, Mobley and Page [54] observed that in Purkinje fibers the intracellular volume fraction ranges between 0.7 and 0.995 , depending on the density of myofibrils, mitochondria and the number of nexus per cell. The high intracellular volume fraction, which is directly related to the surface to volume ratio of cells, can be accounted for by the highly folded surface of the individual cells. They also found that the external surface appeared to be less folded than the internal surface. Considering the extremely varied geometry of cardiac myocytes [77, 78], our simulations for $f_i = 0.6 \sim 0.9$ should provide a realistic representation of electrical behavior of cardiac tissue.

Chapter 4

Anisotropic Bidomain Conductivities

Cardiac tissue is made up of interdigitating myocardial fibers. The fibers are actually strings of cells joined end-to-end by intercalated disks which provide low-resistance electrical coupling [85]. The geometry of individual cardiac myocytes is extremely varied, but they have a general cylindrical shape averaging $30 \sim 130\,\mu m$ in length and $8 \sim 20\,\mu m$ in diameter. Sommer and Scherer [78] have shown that cardiac myocytes are in general connected to their neighbors through nexus junctions, not only in the longitudinal direction but also in the lateral direction. The density of cell junctions is substantially larger in the longitudinal direction, thus giving rise to a larger average intracellular conductivity along the fiber axis. Cell packing occurs in the form of fiber bundle which also favors a larger longitudinal interstitial conductivity. As a result, myocardial tissue displays anisotropic electrical conductivity, leading to substantial directionally-dependent effects on action potential waveform and propagation [13, 21, 22, 79].

Considering that the intracellular and interstitial spaces can be regarded as continuous, there are three conductivities in each domain, corresponding to the three principal axes of the tissue. In general, it is assumed that the intracellular conductivities in the two directions perpendicular to the principal fiber axis are equal [13, 70]. This assumption is also made for the corresponding interstitial conductivities. Therefore, at the macroscopic level, there are four conductivity parameters: the intracellular and interstitial longitudinal and transverse conductivities (σ_{il}, σ_{it}, σ_{el} and σ_{et}). In this chapter, we will investigate whether these bidomain conductivities are homogeneous and how they are affected by cell packing using a cylindrical cardiac bundle model with the boundary element method.

4.1 Basic Theory

The bidomain model assumes that cardiac tissue is composed of uniform conductors. In the tissue, the relationship between uniform conductivity (σ), the current density ($\vec{J}$) and potential (ϕ) is described mathematically by the following equation,

$$\vec{J} = -\sigma \bigtriangledown \phi \, .$$

In a cylindrical coordinate system, with x and r representing respectively the axial and radial directions, the intracellular and extracellular current densities are

$$\vec{J}_i(P) = -\sigma_{ir} \frac{\partial \phi_i}{\partial r} \vec{a}_r - \sigma_{ix} \frac{\partial \phi_i}{\partial x} \vec{a}_x \tag{4.1}$$

and

$$\vec{J}_e(P) = -\sigma_{er} \frac{\partial \phi_e}{\partial r} \vec{a}_r - \sigma_{ex} \frac{\partial \phi_e}{\partial x} \vec{a}_x \tag{4.2}$$

where $\vec{a}_r$ and $\vec{a}_x$ are unit vectors along the radial and longitudinal directions, e and i represent the interstitial and intracellular volumes, respectively, and P is an observation point within the bundle. Since the bundle is symmetric (see Fig.2.2), there is no angular variation of potential.

Denoting the source current per unit volume as I_v, requiring conservation of current:

$$\vec{\nabla} \cdot \vec{J}_i = -I_v \tag{4.3}$$

and

$$\vec{\nabla} \cdot \vec{J}_e = I_v \tag{4.4}$$

In cylindrical coordinates these equations become

$$\frac{1}{r}\frac{\partial}{\partial r}(rJ_{ir}) + \frac{\partial J_{ix}}{\partial x} = -I_v \tag{4.5}$$

and

$$\frac{1}{r}\frac{\partial}{\partial r}(rJ_{er}) + \frac{\partial J_{ex}}{\partial x} = I_v \ . \tag{4.6}$$

Substituting Eqs (4.1) and (4.2) into (4.5) and (4.6), we obtain the following equations,

$$\sigma_{ix}\frac{\partial^2 \phi_i}{\partial x^2} + \sigma_{ir}\left(\frac{1}{r}\frac{\partial \phi_i}{\partial r} + \frac{\partial^2 \phi_i}{\partial r^2}\right) = -I_v \tag{4.7}$$

and

$$\sigma_{ex}\frac{\partial^2 \phi_e}{\partial x^2} + \sigma_{er}\left(\frac{1}{r}\frac{\partial \phi_e}{\partial r} + \frac{\partial^2 \phi_e}{\partial r^2}\right) = I_v \ . \tag{4.8}$$

Since the only source (except at injecting locations) in the bundle is the membrane current I_{m}, I_v in Eqs (4.7) and (4.8) should be replaced by βI_{m}, where β is the

surface-to-volume ratio. In order to relate our simulation results to those of earlier experimental and theoretical studies [13, 34, 45, 62], we have chosen to use resistivities instead of conductivities in the rest of this report. Substituting $\rho_{ql} = 1/\sigma_{ql}$ ($q = i, e$ and $l = x, r$) into Eqs (4.7) and (4.8) and assuming $I_{\rm m}$ to be positive out of cells, it yields

$$\frac{1}{\rho_{ix}}\frac{\partial^2\phi_i}{\partial x^2} + \frac{1}{\rho_{ir}}\left(\frac{1}{r}\frac{\partial\phi_i}{\partial r} + \frac{\partial^2\phi_i}{\partial r^2}\right) = \beta\, I_{\rm m} \tag{4.9}$$

and

$$\frac{1}{\rho_{ex}}\frac{\partial^2\phi_e}{\partial x^2} + \frac{1}{\rho_{er}}\left(\frac{1}{r}\frac{\partial\phi_e}{\partial r} + \frac{\partial^2\phi_e}{\partial r^2}\right) = -\beta\, I_{\rm m}\,. \tag{4.10}$$

These are the governing equations, which relate the bidomain resistivities to potentials and transmembrane current. For our purpose, Eq.(4.9) and Eq.(4.10) each define linear equations with the potential derivatives being known coefficients and the resistivities being the unknown factors to be solved for.

1) Least squares method

We can use two different sets of potential and membrane current to obtain the resistivities in both volumes by solving the above linear system. In order to obtain more generalized resistivities, the system will be overdetermined and solved in the least square sense. There are two possible approaches to overdetermine this system; one option is to take different values of ϕ and $I_{\rm m}$ along the axial direction $(x_1, \cdots, x_m)$ at one specific time instant (t_p) and for one specific radial layer (r_j). This is expressed by the following equations:

$$\frac{1}{\rho_{kx}}\frac{\partial^2\phi(r_j, x, t_p)_k}{\partial x^2}\bigg|_{x_1} + \frac{1}{\rho_{kr}}\left(\frac{1}{r}\frac{\partial\phi(r, x_1, t_p)_k}{\partial r} + \frac{\partial^2\phi(r, x_1, t_p)_k}{\partial r^2}\right)\bigg|_{r_j} = \pm\beta\, I_{\rm m}(r_j, x_1, t_p) \tag{4.11}$$

$$\vdots$$

$$\frac{1}{\rho_{kx}}\frac{\partial^2\phi(r_j,x,t_p)_k}{\partial x^2}\bigg|_{x_m}+\frac{1}{\rho_{kr}}\left(\frac{1}{r}\frac{\partial\phi(r,x_m,t_p)_k}{\partial r}+\frac{\partial^2\phi(r,x_m,t_p)_k}{\partial r^2}\right)\bigg|_{r_j}=\pm\beta\, I_{\mathrm{m}}(r_j,x_m,t_p) \tag{4.12}$$

where $m > 2$ is the number of values for ϕ and I_{m} to be chosen, $k = i, e$ represent intracellular and interstitial volumes, respectively, and $j = 1, 2, \cdots$ indicates the radial layer number from the center to the surface of the bundle.

The second possibility is to measure different values of ϕ and I_{m} at several time instants $(t_1, \cdots, t_n)$ at a fixed axial position (x_l) and radial layer (r_j). This procedure can be represented by the following equations:

$$\frac{1}{\rho_{kx}}\frac{\partial^2\phi(r_j,x,t_1)_k}{\partial x^2}\bigg|_{x_l}+\frac{1}{\rho_{kr}}\left(\frac{1}{r}\frac{\partial\phi(r,x_l,t_1)_k}{\partial r}+\frac{\partial^2\phi(r,x_l,t_1)_k}{\partial r^2}\right)\bigg|_{r_j}=\pm\beta\, I_{\mathrm{m}}(r_j,x_l,t_1) \tag{4.13}$$

$$\vdots$$

$$\frac{1}{\rho_{kx}}\frac{\partial^2\phi(r_j,x,t_n)_k}{\partial x^2}\bigg|_{x_l}+\frac{1}{\rho_{kr}}\left(\frac{1}{r}\frac{\partial\phi(r,x_l,t_n)_k}{\partial r}+\frac{\partial^2\phi(r,x_l,t_n)_k}{\partial r^2}\right)\bigg|_{r_j}=\pm\beta\, I_{\mathrm{m}}(r_j,x_l,t_n) \tag{4.14}$$

where subscripts n, k and j have the same meaning as above.

The potential derivatives as well as the membrane current in the above equations are computed with the BEM. Since the BEM does include the boundary effects, both the matrix coefficients and the right-hand side of the overdetermined system will be radially dependent. Consequently, the unknown resistivities will also depend on the radial position in the bundle. It is not contradictory to the original

Eqs. (4.1) and (4.2) which are based on the assumption that σ_{ix}, σ_{ir}, σ_{ex} and σ_{er} are constants in space, since it is expected that boundary effects will only exist in the outermost layers of muscle fibers. Thus it is plausible that constant, radially independent resistivity estimates can be obtained throughout the deeper layers of the bundle.

2) Volume fraction approach

Previously, Cole and Curtis [14] have attempted to relate bidomain resistivities ρ_{ix}, ρ_{ir}, ρ_{ex} and ρ_{er} to the bulk intracellular resistivity (ρ_i) and the bulk interstitial resistivity (ρ_e) by means of the intracellular volume fraction f_i. The proposed relationships are:

$$\rho_{ix} = \rho_i / f_i \tag{4.15}$$

$$\rho_{ex} = \rho_e / (1 - f_i) \tag{4.16}$$

$$\rho_{er} = \frac{1 + f_i}{1 - f_i} \rho_e \, . \tag{4.17}$$

It is less clear how the intracellular radial resistivity ρ_{ir} relates to the microscopic resistivity parameters. According to theoretical [70, 79] and experimental [13] considerations, the anisotropy ratio of the intracellular space is about 10, so that

$$\rho_{ir} \cong 10 \, \rho_{ix} \, . \tag{4.18}$$

It is difficult to develop simple expressions like Eqs (4.15) to (4.17) if we use a more complex model of the tissue structure. We shall demonstrate, using simulation, that this conventional method to evaluate bidomain resistivities is very limited.

4.2 Simulations

Since uniform and stable electrical activity is necessary for good estimates of the bidomain resistivities, a propagating action potential was elicited at the proximal end of the bundle and ϕ_i, ϕ_e and I_{m} computed with the BEM at mid-length were used to avoid end effects. The evaluation of resistivity parameters based on Eqs (4.11) to (4.14) was carried out using Matlab. The estimates were separated into two groups. One group, based on Eqs (4.11) and (4.12), is used to estimate $\rho_{ix}, \rho_{ir}, \rho_{ex}$ and ρ_{er} at each radial layer by taking simulated potential and membrane current values at different longitudinal positions and at a specific time instant. The other group, based on Eqs (4.13) and (4.14), serves to estimate $\rho_{ix}, \rho_{ir}, \rho_{ex}$ and ρ_{er} at each transverse layer by taking simulated potential and membrane current values at different time durations and at a fixed axial position. We compared the results of the two methods and noted that there is no significant difference between the two groups of estimates.

To determine the quality of the numerical estimates, the estimated values of $\rho_{ex}, \rho_{er}, \rho_{ix}$ and ρ_{ir} were substituted back into Eqs (4.9) and (4.10) to fit the membrane current on limited longitudinal segments. $I_{\mathrm{m\_e}}$ and $I_{\mathrm{m\_i}}$ will be used to represent the fit membrane current from ρ_{ex}, ρ_{er} and from ρ_{ix}, ρ_{ir}, respectively. The results at different layers show an excellent fit (Fig.4.1).

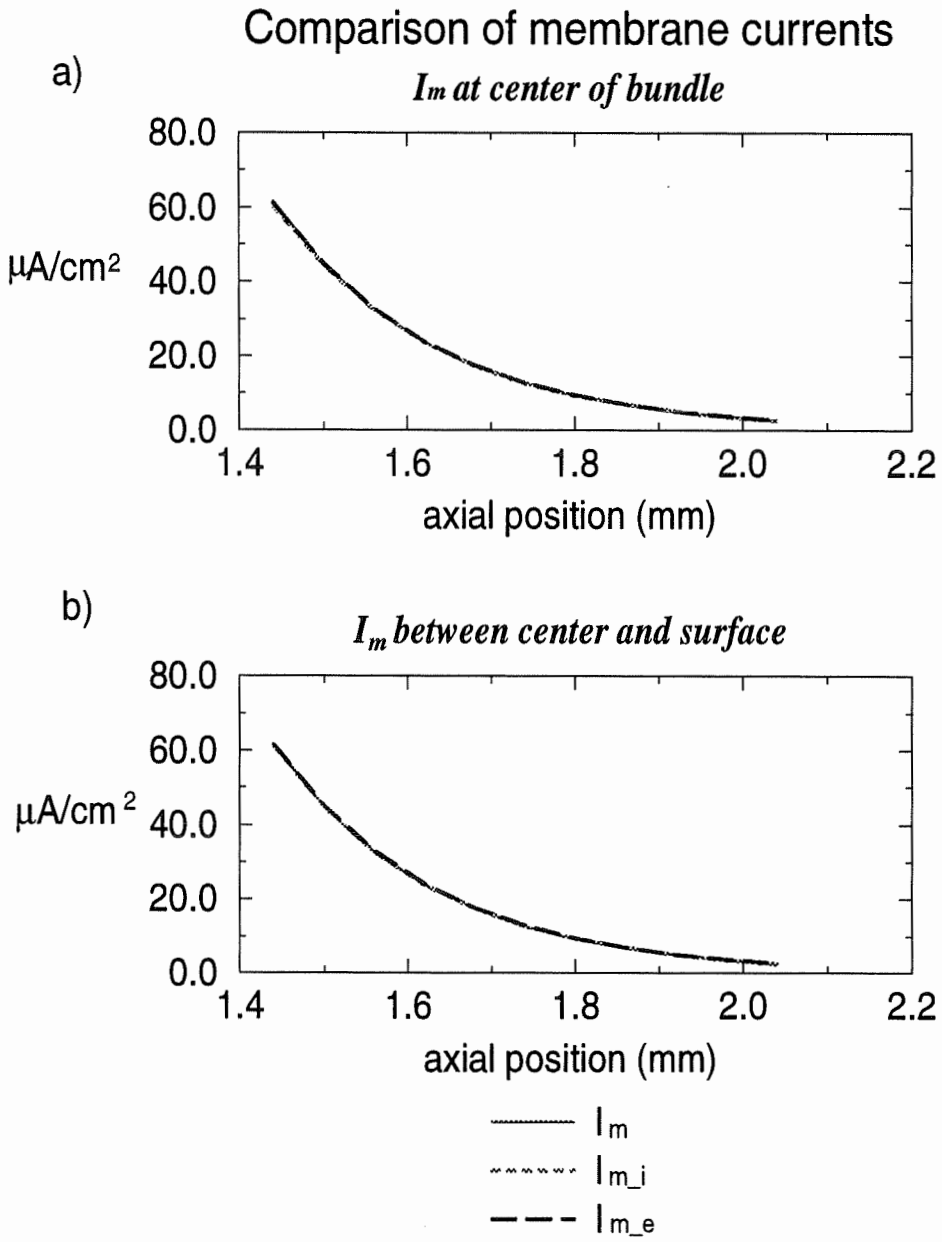

Figure 4.1: Comparison of membrane currents on a limited longitudinal bundle segment at the center of the bundle a) and between the center and the surface of the bundle b). The abscissa corresponds to a part of the bundle axis.

4.3 Validation of estimated resistivity parameters

Our first concern was to show that the estimates were position- and time-independent. Fig.4.2 shows that the fit of I_{m_e} and I_{m_i} to I_m at different radial positions are excellent except at positions close to the stimulation site. This can be attributed to numerical inaccuracies of the second derivatives of potential near the singularities (sharp changes in potential and its first derivative), and to the effects of current injection in the vicinity of the proximal end of the bundle.

To verify that the estimates were time-independent, the membrane current was fitted at several randomly chosen time instants using resistivities estimated at previous time instants, simulated intracellular and interstitial potentials and their derivatives. Again the fits are excellent as shown in Fig.4.3 which illustrates the results from two simulations at $t = 0.75\,ms$ and $t = 3.75\,ms$.

Finally we examined the uniqueness of the resistivity estimates. We changed resistivity parameters ρ_{ql} ($q = i, e$ and $l = x, r$) one at a time, by $\pm 5\%$, $\pm 10\%$, $\pm 15\%$ and $\pm 20\%$ respectively and leaving the other parameters at their estimated values. We then fit to the transmembrane current using Eq.(4.9) or (4.10) at randomly chosen time instants and positions in the bundle. We found that perturbations of ρ_{ex} and ρ_{ix} within $\pm 10\%$ and ρ_{er} within $\pm 5\%$, changed I_{m_q} ($q = i\,, e$) by an equal amount. For ρ_{ir}, however, the perturbation in I_{m_i} was not as the same amount as that in ρ_{ir}, suggesting that we failed to obtain a stable unique value of ρ_{ir} using the least squares method in this case. This was because of the small radial gradient of

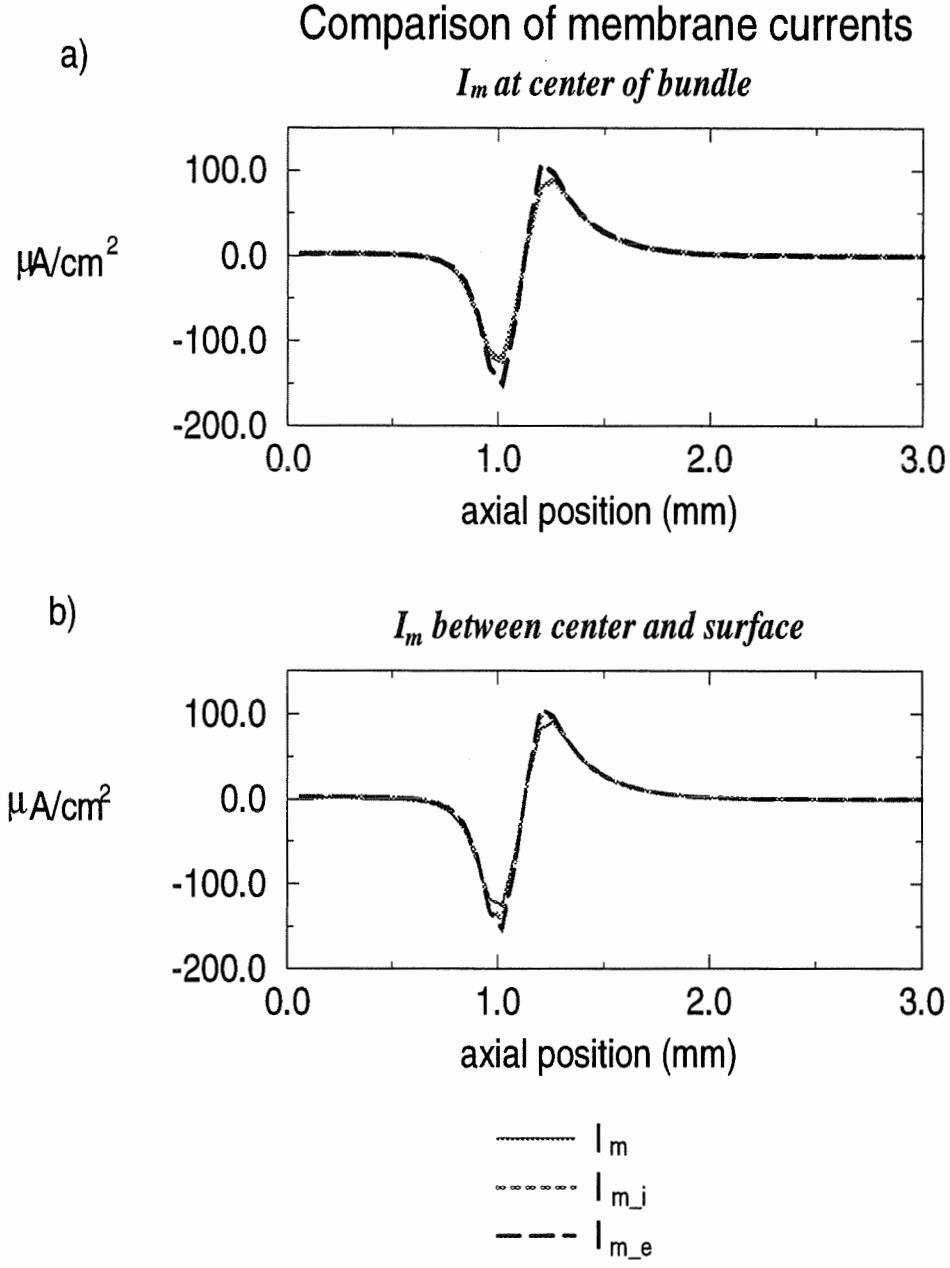

Figure 4.2: Comparison of membrane currents on the bundle axis. a) taken at the center of the bundle, b) between the center and the surface of the bundle.

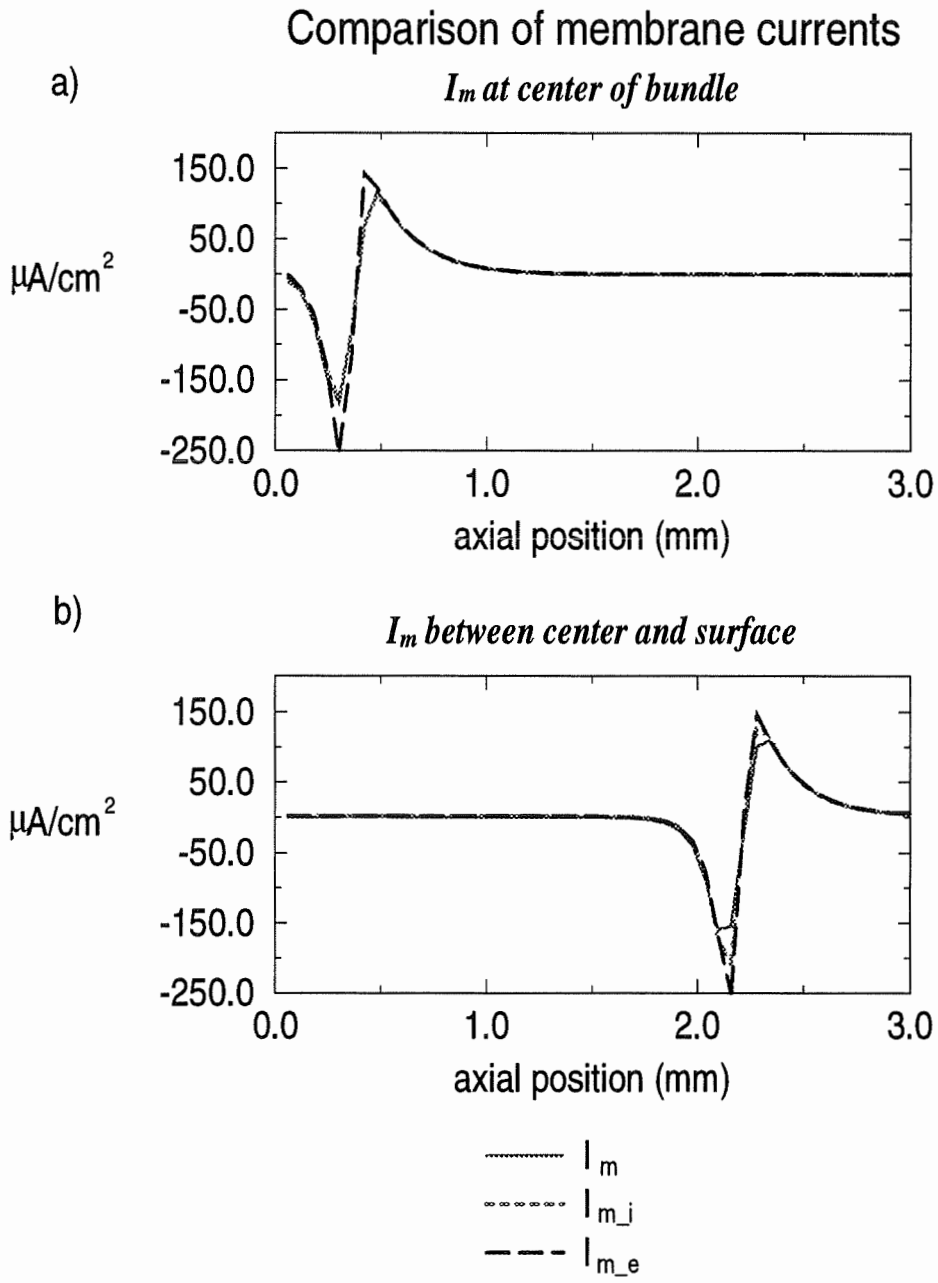

Figure 4.3: Comparison of membrane currents at randomly chosen time instants. a) at $t = 0.75\,msec$ and b) at $t = 3.75\,msec$. $I_{\rm m}$ is the membrane current obtained from BEM. $I_{\rm m\_i}$ is calculated from the estimated intracellular resistivities (ρ_{ix}, ρ_{ir}) based on Eq.(4.9). $I_{\rm m\_e}$ is from the estimated interstitial resistivities (ρ_{ex}, ρ_{er}) using the same method.

intracellular potential during action potential propagation.

4.4 Bidomain resistivities of the bundle

4.4.1 Distribution of resistivities on different radial layers

Bidomain resistivities ρ_{ex}, ρ_{er} and ρ_{ix} of the bundle were evaluated using the method described in the previous subsection. Since ρ_{ir} estimated using this method is not unique, it is not discussed here. In next chapter, we will see that ρ_{ir} can be determined uniquely using the impedance measurement method. Fig.4.4 shows the changes in ρ_{ex} along the radial direction, and its distribution for different values of the intracellular volume fraction. For a given packing density, the calculated ρ_{ex} is almost constant except in the outermost layers where it drops quickly to attain the low resistivity of the surrounding volume conductor. When the packing density was increased, the shift became more significant since ρ_{ex} at the center of the bundle was then substantially larger. ρ_{er} also increases as f_i increases but it shows little change as the bundle boundary is approached (Fig.4.5).

Considering the constant assumption of ρ_{ex}, ρ_{er}, ρ_{ix} and ρ_{ir} in deduction of the linear system from Eq.(4.11) to (4.14), the changes in ρ_{ex} and ρ_{er} in the radial direction shown in Fig.4.4 and Fig.4.5 are artificial due to the boundary effect and should not be attributed to cause any effects.

Fig.4.6 shows the distribution of ρ_{ix} as a function of depth into the bundle for different intracellular volume fractions. As in the case of ρ_{ex}, ρ_{ix} displays a substantial change with f_i, but, as expected, negligible bundle boundary effects.

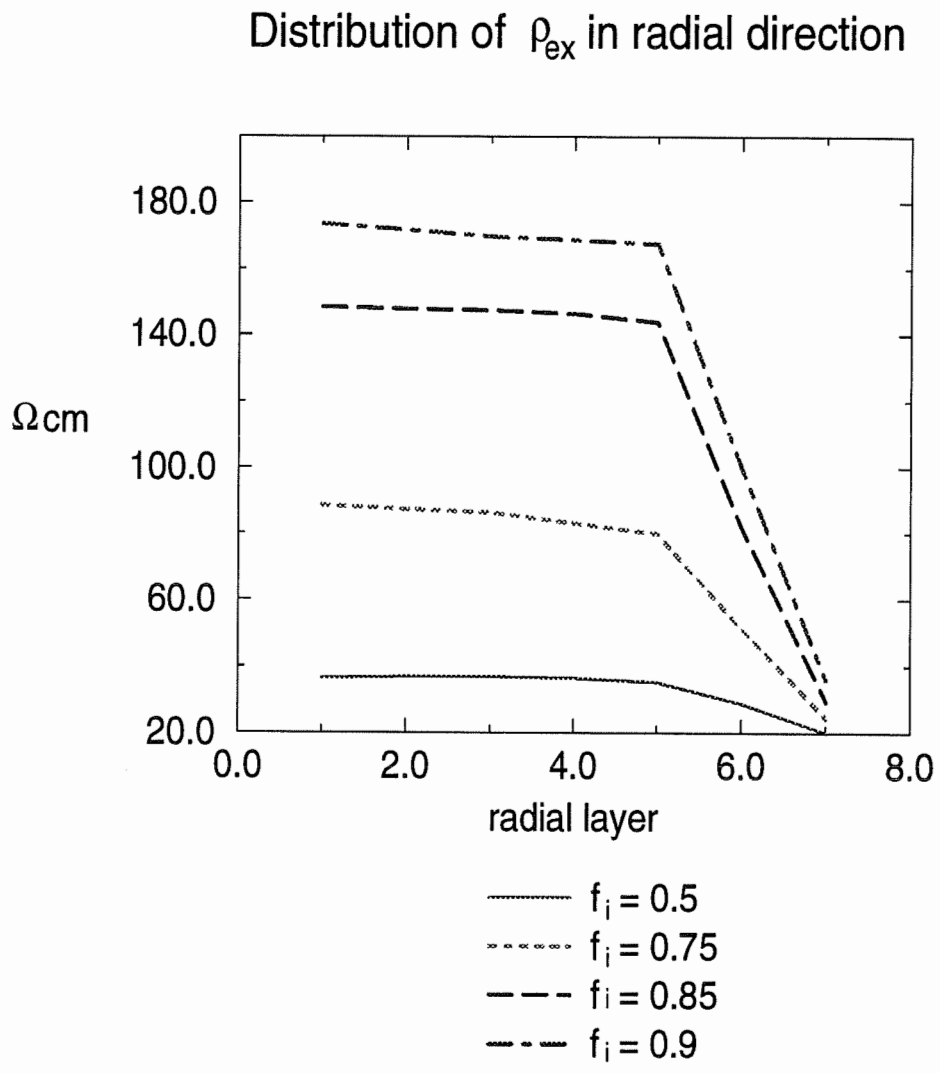

Figure 4.4: Distribution of the interstitial axial resistivity ρ_{ex} along the radial direction with different values of f_i. The abscissa represents different layers of the bundle from 1 to 7, corresponding the center towards the surface of the bundle.

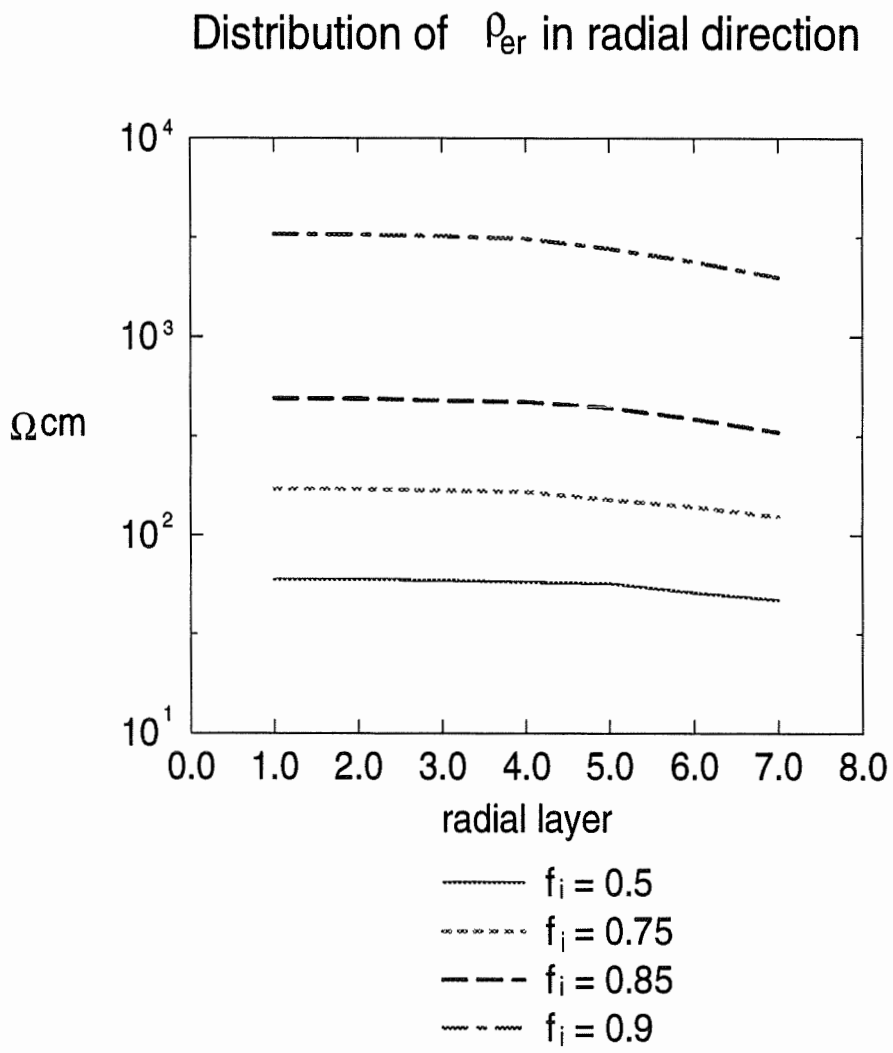

Figure 4.5: Distribution of the interstitial axial resistivity ρ_{ex} along the radial direction for different f_i values. Same abscissa as in Fig.4.4.

Therefore, away from the surface of the bundle, the interstitial resistivities ρ_{ex} and ρ_{er} are constant for a given packing density. Near the bundle surface, the abrupt reduction of ρ_{ex} is caused by the boundary effects, which dominate the potential distributions ϕ_i and ϕ_e. As expected, there is little boundary effect on ρ_{ix}. As the packing density is reduced, the interstitial resistivities in both directions decrease, whereas ρ_{ix} increases. These phenomena are consistent with the fact that tight packing hinders the local circuit current flow, leading to increased interstitial resistivities and reduced conduction velocity (see Fig.3.7).

4.4.2 Effect of the intracellular volume fraction f_i on resistivities

In the previous chapter, we discussed the effect of the packing density of the bundle on the propagating action potential. It is interesting to examine the role played by the microstructure in determining the passive properties of the bundle. In this subsection, the effect of the packing density on the bundle resistivities, estimated using the least squares method based on simulated potentials and membrane current with the boundary element method, are investigated and compared to the predictions of the volume fraction method used in the bidomain model Eqs (4.15) to (4.17).

Fig.4.7 to 4.9 illustrate the variations of the interstitial resistivities (ρ_{ex} and ρ_{er}) and intracellular axial resistivity (ρ_{ix}) with the intracellular volume fraction f_i estimated by the least squares method. To compare with their counterparts predicted by the volume fraction method, these estimates from the volume fraction

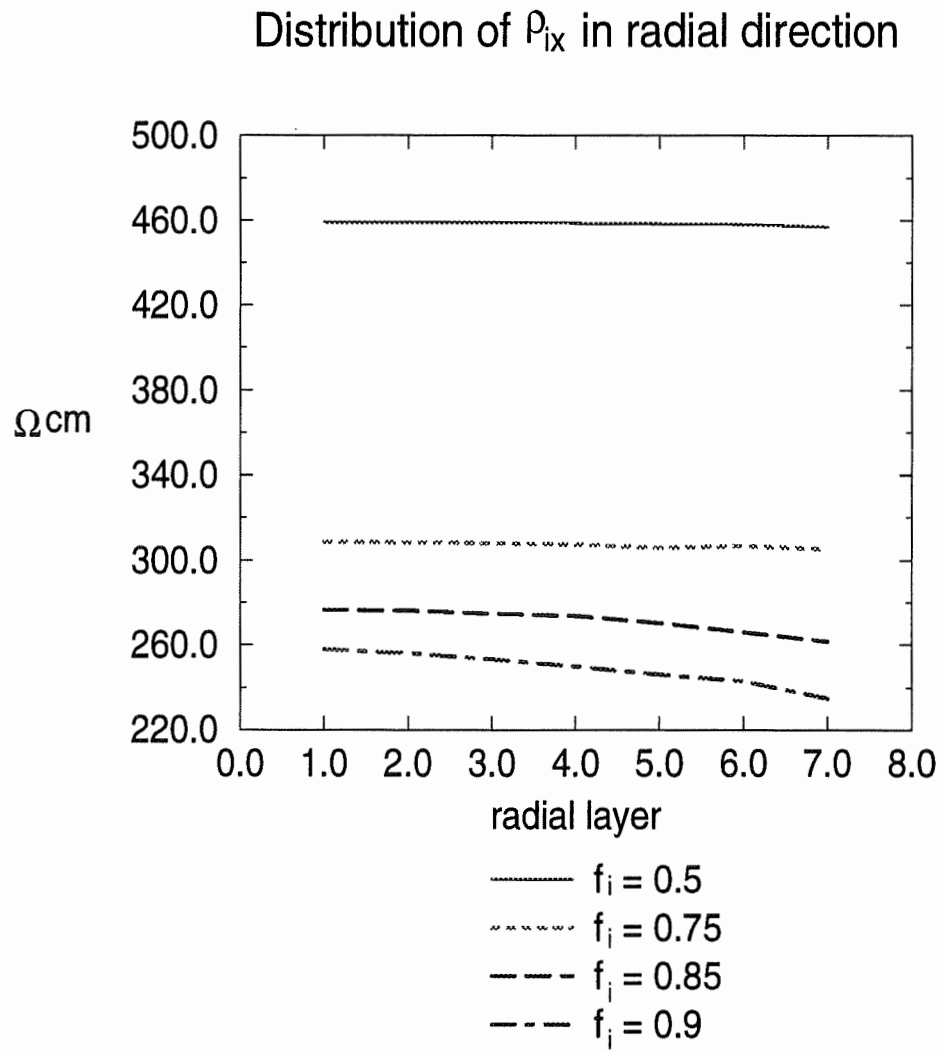

Figure 4.6: Distribution of the intracellular axial resistivity ρ_{ix} along radial direction with different f_i. Same abscissa as in Fig.4.4.

method are shown in these figures also. In all cases, the values obtained from the volume fraction method are lower than those computed by the least squares method, although the general patterns of change are similar. One main difference between the results from the volume fraction method and from the least squares method is reflected in ρ_{er}. The increase in ρ_{er} with the packing density predicted by the least squares method is much greater than that predicted by the bidomain model (see Fig.4.8). The higher interstitial resistivities ρ_{ex} and ρ_{er} at tight packing are caused by reduced interstitial space, which reduces the amplitude of the local current flowing through the neighbor cells to activate them, resulting in more current entering the intracellular space.

4.5 Discussion

Unlike our model which considers a detailed description of the microstructure of the tissue, the bidomain model gives a macroscopic view of the electrical behavior of the cardiac tissue. In this model the discrete structure of tissue in both the intracellular and interstitial media is replaced by homogeneous, anisotropic, resistive domains occupying the same space. Then the tissue is characterized by four passive electrical parameters ρ_{ex}, ρ_{er}, ρ_{ix} and ρ_{ir}. In this chapter, these parameters and their relationship with a very simple regular bundle structure were examined. We developed an approach which used the intracellular and interstitial potentials, their spatial derivatives and membrane currents simulated by the boundary element

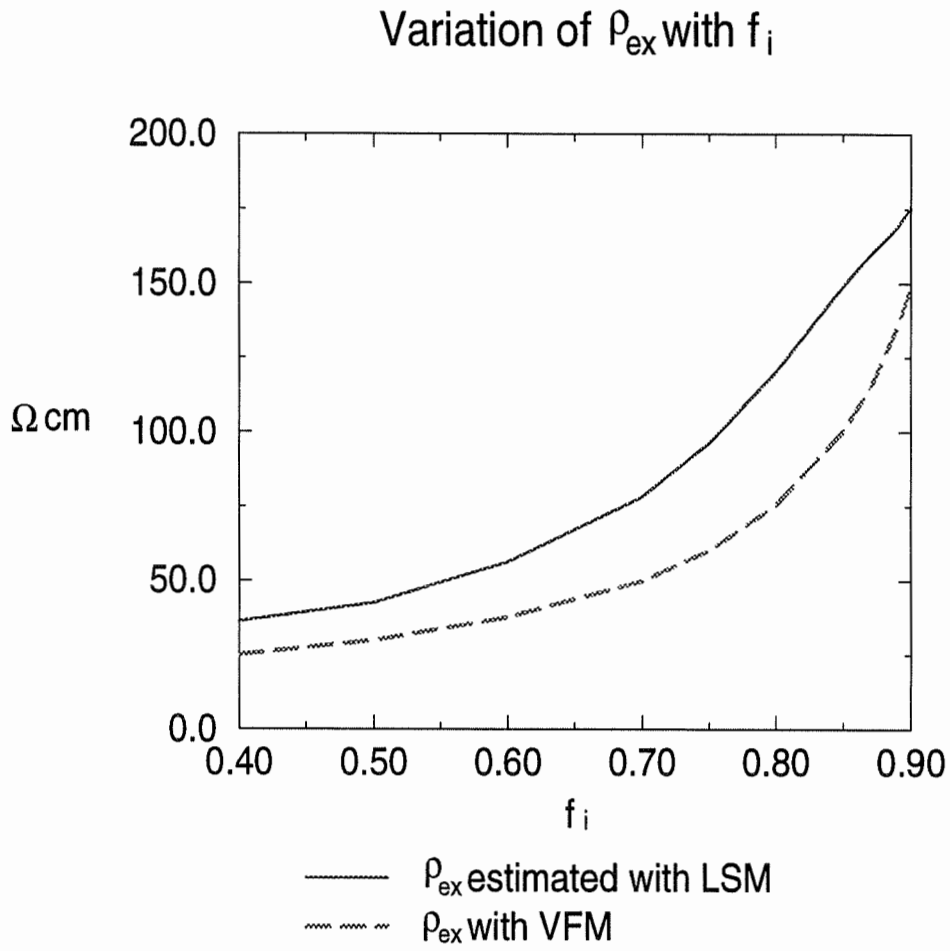

Figure 4.7: Variation of the interstitial axial resistivity ρ_{ex} with the intracellular volume fraction f_i. LSM is the abbreviation of the least squares method, VFM the volume fraction method. The radius of the bundle changes from 62.5 μm to 82.5 μm corresponding to the variation of f_i.

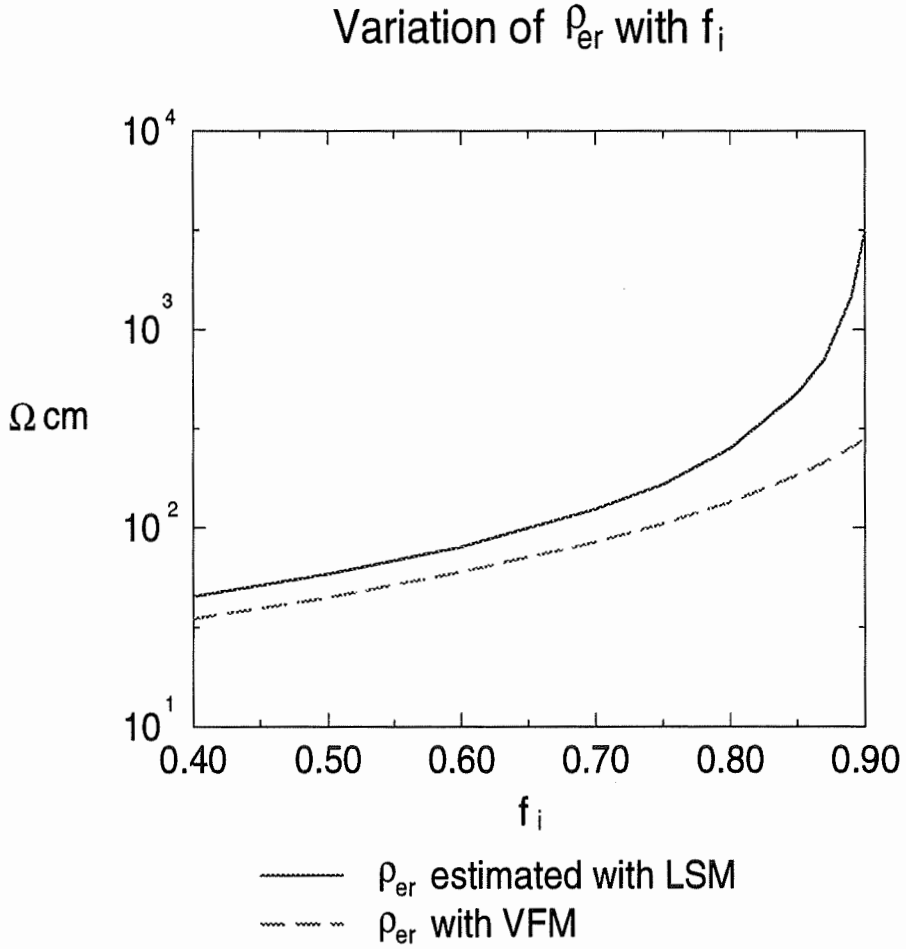

Figure 4.8: Variation of the interstitial radial resistivity ρ_{er} with the intracellular volume fraction f_i. LSM and VFM are the same as Figure 4.7.

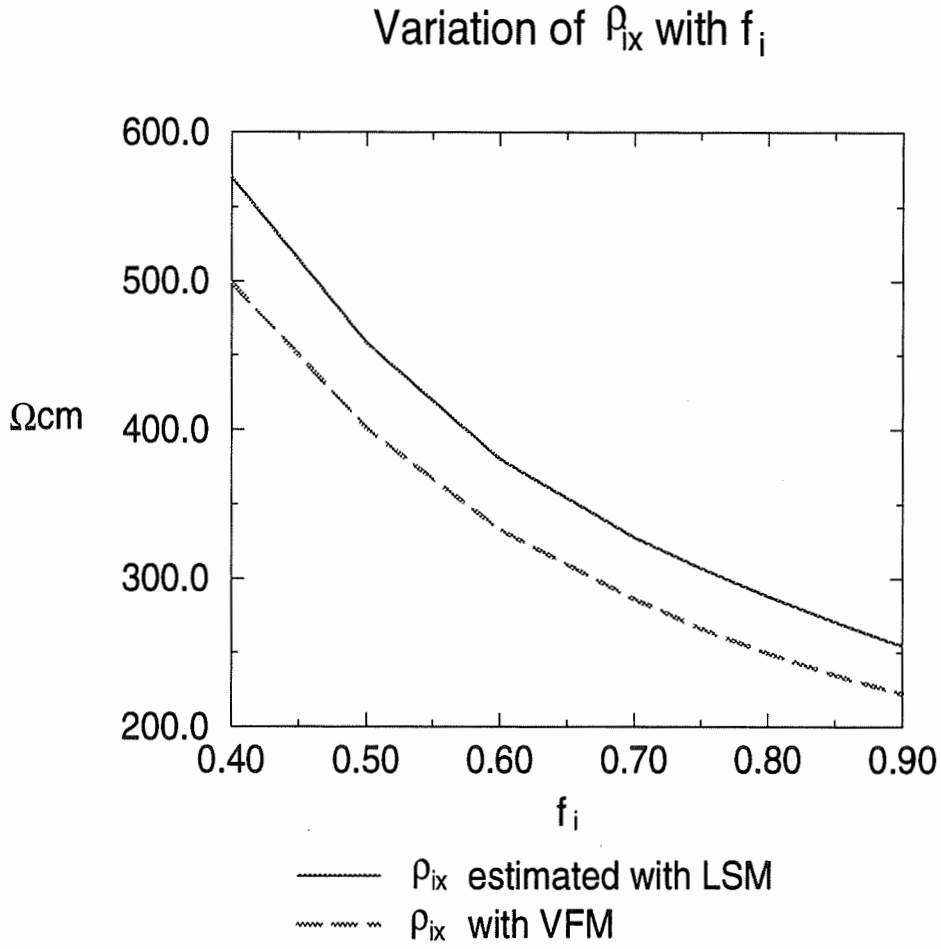

Figure 4.9: Variation of the intracellular axial resistivity ρ_{ix} with the intracellular volume fraction f_i. LSM and VFM are the same as Figure 4.7.

method, and ionic current stimulation to estimate these four passive parameters.

Using this technique, we obtained estimates of ρ_{ex} and ρ_{ix} similar to those predicted by previous investigators. On the other hand, the classical approach seriously underestimated ρ_{er} for tight packing, although the predictions for ρ_{er} at loose packing ($f_i < 0.75$) by these two different methods was in agreement.

This difference is caused by the microstructure arrangement. The interstitial radial resistivity ρ_{er} depends on the resistance of the current path from the center of the bundle to the bundle surface in the interstitial space. In the standard volume fraction formula, ρ_{er} is proportional to the ratio $(1 + f_i)/(1 - f_i)$, which is determined by a constant width zig-zag path that lies exclusively in the interstitial space [68, 69]. The resistance of this zig-zag path depends on the average width of the space between the fibers. As the packing density increases, the average width between fibers reduces smoothly, so that ρ_{er} does not increase dramatically. On the other hand, the resistance of the current pathway in our configuration of the bundle, which is a suspension of parallel cylinders (see Fig.2.3), is mainly dependent on the minimum distance between fibers. At loose packing density, this distance is relatively large so that the resistance of the pathway does not change significantly with the packing. At tight packing, however, the minimum distance between fibers is very small, as a result the pathway resistance at this junction is much greater than elsewhere, thus dominating resistivity ρ_{er}.

Our simulation results indicate that the standard volume fraction method (Eqs (4.15) to (4.17)) used in the bidomain model, give good estimates of the longi-

tudinal resistivities in both the intracellular and interstitial media (ρ_{ix} and ρ_{ex}) for any packing, and it provides a reasonable estimate of interstitial radial resistivity (ρ_{er}) for loose packing ($f_i < 0.75$).

Chapter 5

Estimation of Resistivities Using Extracellular Measurements

The classical approach to measure impedance, the four-electrode technique, was first described by Bouty in 1884 [11]. Since then it has been widely used for electrophysiological measurements [29]. The advantage of this approach is that it creates a uniform current density distribution between the potential electrodes, so that resistivity measurements can be made without introducing errors due to electrode polarization [1]. A thorough discussion of the approach can be found in Nyboer [57, 58] and Bagno [6].

In early impedance studies of cardiac muscle, the tissue was assumed to be a uniform, isotropic, and continuous medium referred to as an isotropic monodomain. Schwan and Kay used this simple model to interpret their two-electrode measurements [74]. Rush *et al.* [72] significantly improved on the measurement of cardiac tissue impedance in two ways: 1) instead of a single pair of electrodes, they used a four-electrode arrangement; 2) they recognized that cardiac tissue resistivity is

anisotropic. The four-electrode technique was later used to determine the resistivities in relation to an isotropic bidomain model [77], and to the anisotropic bidomain model [61, 62].

As noted in Chapter 2, Eq.(2.36) governs the resistivity measurements in the anisotropic bidomain model presented by Plonsey and Barr [61], and is limited by the assumption of an equal anisotropy ratio, *i.e.*, $\rho_{ix}/\rho_{iy} = \rho_{ex}/\rho_{ey} = k$. In this chapter, we describe and evaluate a method to evaluate the anisotropic resistivity parameters of a cardiac fiber bundle, which only uses the interstitial potential, and does not rely on the assumption of equal anisotropy ratio.

5.1 Theory

In section (2.3), we discussed two ways of measuring the anisotropic bidomain resistivities: 1) application of direct current with different interelectrode spacing, or 2) application of sinusoidal current with a fixed interelectrode distance. In our simulation study, we chose the latter approach to estimate the bidomain resistivities.

Considering Eq.(4.10) (see section (4.1)) at the positions where the two potential-measurement electrodes are located (denoted as x_1 and x_2, see Fig.5.1,), we can write

$$\frac{1}{\rho_{ex}}\frac{\partial^2\phi_e}{\partial x^2}\bigg|_{x_1} + \frac{1}{\rho_{er}}\left(\frac{1}{r}\frac{\partial\phi_e}{\partial r} + \frac{\partial^2\phi_e}{\partial r^2}\right)\bigg|_{x_1} = -\beta\, I_{\mathrm{m}}(x_1)\,, \tag{5.1}$$

$$\frac{1}{\rho_{ex}}\frac{\partial^2\phi_e}{\partial x^2}\bigg|_{x_2} + \frac{1}{\rho_{er}}\left(\frac{1}{r}\frac{\partial\phi_e}{\partial r} + \frac{\partial^2\phi_e}{\partial r^2}\right)\bigg|_{x_2} = -\beta\, I_{\mathrm{m}}(x_2)\,. \tag{5.2}$$

Subtracting Eq.(5.2) from Eq.(5.1), we obtain

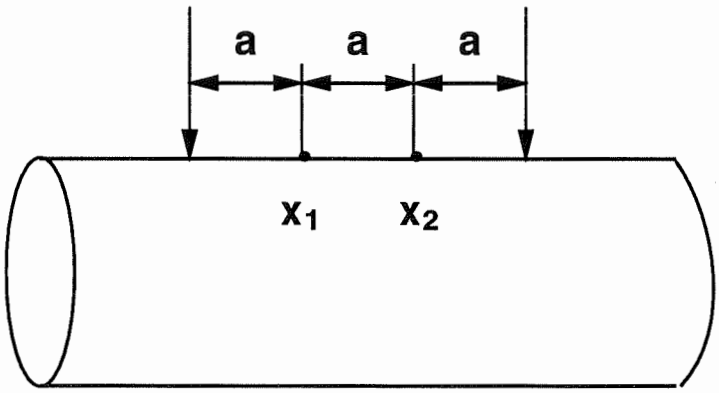

Figure 5.1: Diagram of the impedance measurement. The two arrows point out the current source electrode positions. x_1 and x_2 indicate the potential-measurement electrode positions. The distance between the source electrodes and the measurement electrodes is **a**.

$$\frac{1}{\rho_{ex}}\left(\frac{\partial^2\phi_e}{\partial x^2}\bigg|_{x_1}-\frac{\partial^2\phi_e}{\partial x^2}\bigg|_{x_2}\right)+\frac{1}{\rho_{er}}\left[\frac{1}{r}\frac{\partial}{\partial r}\left(r\frac{\partial\phi_e}{\partial r}\right)\bigg|_{x_1}-\frac{1}{r}\frac{\partial}{\partial r}\left(r\frac{\partial\phi_e}{\partial r}\right)\bigg|_{x_2}\right]=-\beta\,\Delta I_{\mathrm{m}} \tag{5.3}$$

where we use Δ to represent the difference measured between the two potential-measurement electrodes, so that $\Delta I_{\mathrm{m}} = I_{\mathrm{m}}(x_1) - I_{\mathrm{m}}(x_2)$ is the membrane current difference at the site of the two electrodes. It is proportional to the difference in membrane voltage:

$$\Delta I_{\mathrm{m}} = \frac{V_{\mathrm{m}}(x_1) - V_{\mathrm{m}}(x_2)}{Z_{\mathrm{m}}} = \frac{\Delta V_{\mathrm{m}}}{Z_{\mathrm{m}}}\,.$$

According to Plonsey and Barr [61], as long as the interelectrode distance is chosen small enough, *i.e.*, $\mathbf{a} << \lambda_0$ ($\mathbf{a}$ is the distance between source electrodes and potential-measurement electrodes, λ_0 the resting-state space constant of the bundle), the intracellular voltage difference ($\Delta\phi_i$) between the measurement electrodes is negligible (see section 2.3.1), so that

$$\Delta V_{\mathrm{m}} = \Delta\phi_i - \Delta\phi_e \approx -\Delta\phi_e\,.$$

Thus Eq.(5.3) can be written as

$$\frac{1}{\rho_{ex}}\left(\frac{\partial^2\phi_e}{\partial x^2}\bigg|_{x_1}-\frac{\partial^2\phi_e}{\partial x^2}\bigg|_{x_2}\right)+\frac{1}{\rho_{er}}\left[\frac{1}{r}\frac{\partial}{\partial r}\left(r\frac{\partial\phi_e}{\partial r}\right)\bigg|_{x_1}-\frac{1}{r}\frac{\partial}{\partial r}\left(r\frac{\partial\phi_e}{\partial r}\right)\bigg|_{x_2}\right]\approx\beta\,\frac{\Delta\phi_e}{Z_{\mathrm{m}}}\,. \tag{5.4}$$

If the two potential-measurement electrodes are located symmetrically about the axis of the bundle, the potential ϕ_e and its derivatives are antisymmetric at x_1

and x_2. Eq.(5.4) can then be replaced by

$$\frac{1}{\rho_{ex}}\frac{\partial^2\phi_e}{\partial x^2}\bigg|_{x_i} + \frac{1}{\rho_{er}}\left(\frac{1}{r}\frac{\partial\phi_e}{\partial r} + \frac{\partial^2\phi_e}{\partial r^2}\right)\bigg|_{x_i} \approx \beta\,\frac{\phi_e(x_i)}{Z_{\rm m}}\,, \tag{5.5}$$

where $i = 1$ or 2, denotes positions of the measurement electrodes. Thus, the resistivities of the interstitial medium (ρ_{ex}, ρ_{er}) can be obtained by measuring the interstitial potentials in many different positions (to obtain the derivatives) and overdetermining this linear system using the least squares method (Eqs (4.13) and (4.14)).

Using a low frequency *a.c.* source, we have $\mathbf{a} << 1/Re(\gamma(f))$ (see next section), where $1/\gamma(f) = \lambda(f)$ is the space constant of the bundle at frequency f. In this case, $Z_{\rm m} = R_{\rm m}\|C_{\rm m} \approx R_{\rm m}$, the high membrane resistance $R_{\rm m}$ prevents the current from flowing through the intracellular space.

When the frequency of the injected current is increased, the magnitude of $Z_{\rm m}$ is reduced, so that more and more current passes through the membrane into the interior of the cells. Beyond a certain frequency, the intracellular potential, ϕ_i, has increased to a level where it cannot be ignored. In this case, ϕ_e can also be used to estimate the intracellular resistivities. Substituting values of ρ_{ex} and ρ_{er} estimated using Eq.(5.4) or (5.5) into Eq.(4.10), the membrane current, $\hat{I}_{\rm m}$, can be calculated using only the measured ϕ_e (we use the sign $\hat{}$ to represent variables calculated from estimated parameters). Recalling that $V_{\rm m} = \phi_i - \phi_e$ and $V_{\rm m} = Z_{\rm m}\, I_{\rm m}$, we have

$$\hat{\phi}_i = \phi_e + V_{\rm m} = \phi_e + Z_{\rm m}\hat{I}_{\rm m}\,, \tag{5.6}$$

where $Z_{\rm m}$ is defined by Eq.(2.39). Assuming that $R_{\rm m}$ and $C_{\rm m}$ are known, the in-

tracellular potential $\hat{\phi}_i$ is available from Eq.(5.6), and ρ_{ix} and ρ_{ir} can be evaluated using the same approach (Eqs (4.13) and (4.14)).

Experimental application of the above procedure requires to measure the interstitial potential and its spatial derivatives. This can be achieved with many measurements along the same axis if using only a single four-electrode system. LeGuyader [46] utilized a two dimensional square matrix of 8×8 electrodes with equal interelectrode distance for their impedance mapping. It is possible to obtain two dimensional spatial derivatives of the interstitial potential in a flat tissue using this multi-electrode system. Since the system can be decomposed into many conventional four-electrode systems, the resistivity estimations can still be carried out according to the four-electrode measurement theory. In order to distinguish our approach discussed above with the conventional four-electrode technique, we denote this approach 'impedance measurement' in the rest of the thesis. It is similar to the conventional four-electrode technique, since the resistivities are estimated at two fixed positions, the current source and sink electrodes are located at their two extremities, along the same axis with the distance equal to that between the two inner measurement positions.

5.2 Space constant of the bundle

The determination of the optimal distance between electrodes requires knowledge of the resting-state space constant of the bundle. Initially, it can be estimated from a single fiber of infinite length using linear cable theory [42]. This approach is

briefly described below (see [42], p29 for details):

- A prolonged step current change is applied to an infinite cable at $t = 0$;
- far away from the current source ($x \rightarrow \infty$), the transmembrane voltage $V_{\mathrm{m}} \rightarrow 0$;
- when $t \rightarrow \infty$, the response of the infinite cable to this step current source is

$$\frac{V_{\mathrm{m}}(x)}{V_0} = exp\left(-\frac{x}{\lambda_x}\right) ,$$

or

$$ln\left(\frac{V_{\mathrm{m}}(x)}{V_0}\right) = -\frac{x}{\lambda_x} \tag{5.7}$$

where V_0 is the maximum membrane voltage.

Equation (5.7) indicates that the membrane potential V_{m} decays exponentially towards zero along the cable axis, falling to e^{-1} of its initial value in one space constant. On a semilogarithmic plot, the relationship is a straight line with slope $-1/\lambda_x$.

Once the space constant of this single fiber was determined, the membrane resistance R_{m} can be extracted using the following expression ([42], p27)

$$R_{\mathrm{m}} = 2\pi b_r r_i \lambda_x^2 ,$$

where b_r is the cable radius and r_i is the tissue's intracellular resistance. Based on this membrane resistance, the resting space constant of the bundle, λ_0, should be modified by Eq.(2.37).

These simulations were carried out with the aid of Matlab. The radius of the fiber is the same as that of the bundle, but the length was chosen to be three times longer ($9\,mm$) in order to reduce the boundary effects. The prolonged step current was injected at the middle of the fiber. The membrane voltage $V_{\rm m}$ and its exponential fit as $t \rightarrow \infty$ are shown in Fig.5.2. The estimated membrane resistance $R_{\rm m}$ is $5.73\,K\Omega cm^2$ and the resting space constant of the bundle is $690\mu m$.

With a sinusoidal current source, the space constant of the bundle, λ, varies in both amplitude and phase as a function of frequency (f) (see Eq.(2.38) or (2.40)). The exponential term in Eq.(2.36), which is the base to determine the interelectrode spacing, becomes complex valued. Recognizing that $\gamma(\omega) = 1/\lambda(\omega)$ is made up real and imaginary parts:

$$\gamma(\omega) = \gamma_r + j\gamma_i \ .$$

The expression

$$V(x) = V_0 e^{-x/\lambda}$$

is equal to

$$V(x) = V_0 e^{-x(\gamma_r + j\gamma_i)} = V_0 e^{-x\gamma_r} e^{-jx\gamma_i} \ .$$

The reciprocal of the real part of γ, $(1/\gamma_r)$, represents the voltage decay along the bundle axis, and the imaginary part of γ, (γ_i), corresponds to the phase shift of the voltage. Expressing Eq.(2.40) into real and imaginary parts:

$$\lambda(\omega) = \lambda_0 \sqrt{R - jX} \ ,$$

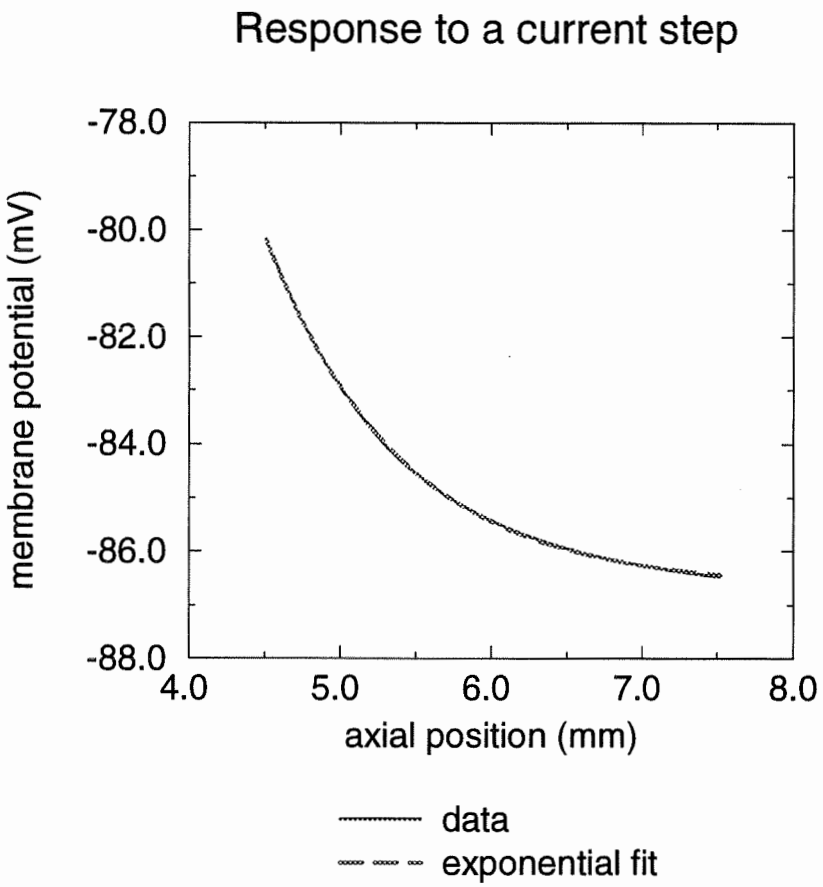

Figure 5.2: Transmembrane potential (solid curve) in response to a prolonged step current as $t \rightarrow \infty$. The length of the cable is $9\,mm$. The stimulating current is injected at $x = 4.5\,mm$ and $t = 0$. The broken curve shows the exponential fit of the data. This is used to calculate the space constant of the cable (see section 5.2).

where

$$R = \frac{1}{1+\omega^2 R_{\rm m}^2 C_{\rm m}^2}\,, \quad X = \frac{\omega R_{\rm m} C_{\rm m}}{1+\omega^2 R_{\rm m}^2 C_{\rm m}^2}\,;$$

thus

$$\gamma_r = \frac{cos(\alpha/2)}{\lambda_0 (R^2+X^2)^{3/4}}$$

$$\gamma_i = \frac{sin(\alpha/2)}{\lambda_0 (R^2+X^2)^{3/4}}$$

$$\alpha = arctan\frac{X}{R}\,.$$

Fig.5.3 shows γ as function of f for $R_{\rm m} = 5.73\,K\Omega cm^2$ and $C_{\rm m} = 1\,\mu F/cm^2$.

5.3 Simulations

To estimate the anisotropic bidomain resistivities, we used a bundle of 800 μm in length with 6 radial layers. The bundle was discretized into 60 longitudinal elements. As Plonsey and Barr [61] suggested, the interstitial resistivities can be measured accurately for $\mathbf{a} < 0.667\,\lambda$, and the intracellular parameters can be obtained when $\mathbf{a} > 3.33\,\lambda$. We used a sinusoidal current source with frequencies varying between $10\,Hz$ and $50\,kHz$. Considering that the resting space constant of the bundle is approximately $690\mu m$, the initial interelectrode distance in our simulations was chosen as $100\,\mu m$. At $10\,Hz$, we have $1/\gamma_r(10\,Hz) \approx \lambda_0$ (where $1/\gamma_r$ corresponds to the real part of $\lambda(f)$), so that $\mathbf{a} \approx 0.15\lambda_0$. In this case, the intracellular potential difference measured by the two potential-measurement electrodes ($\Delta\phi_i$) should be negligible, so that the interstitial resistivities can be estimated by measuring ϕ_e.

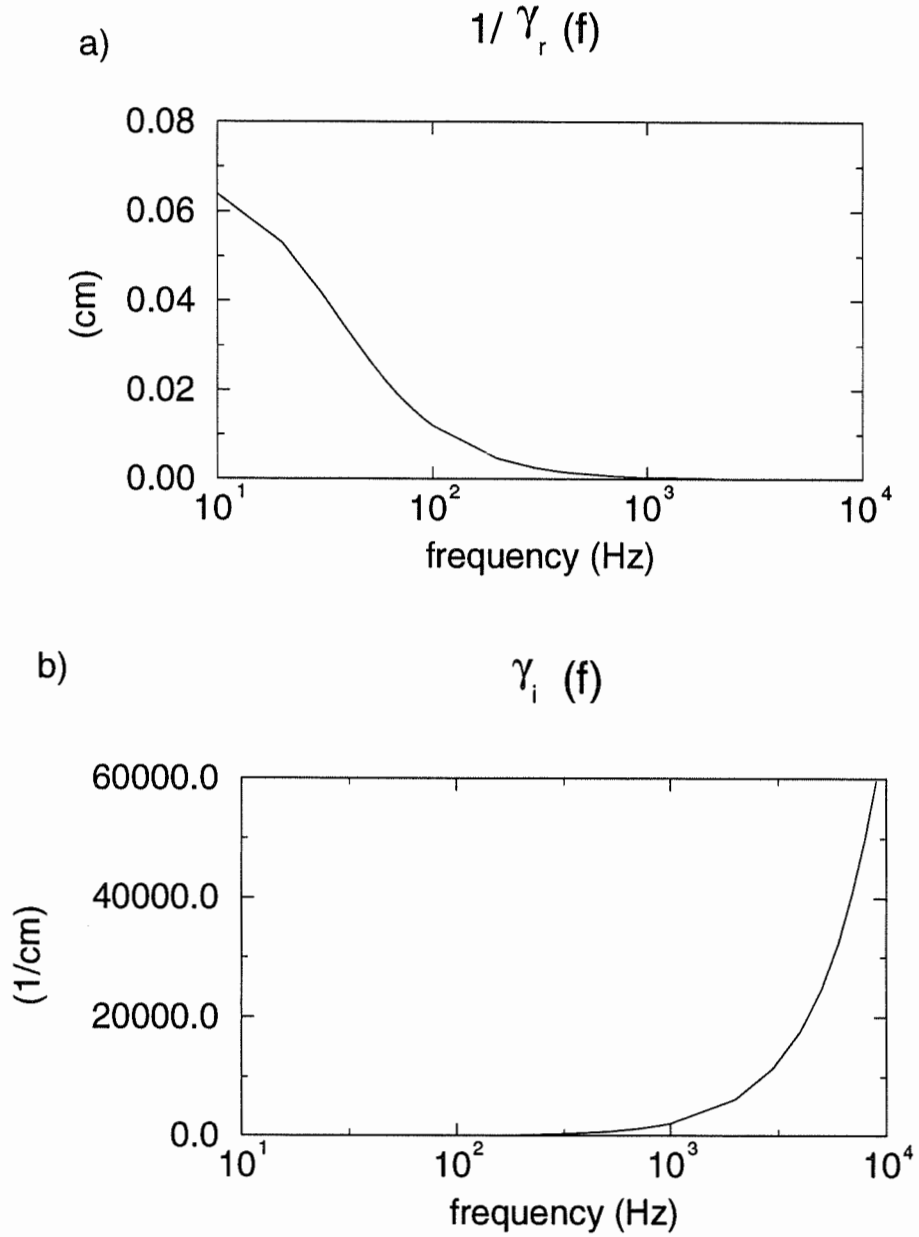

Figure 5.3: Variation of parameter γ with frequency (f) of sinusoidal current for $R_{\mathrm{m}} = 5.73\, K\Omega cm^2$ and $C_{\mathrm{m}} = 1\, \mu F/cm^2$. a) $1/\gamma_r(f)$. b) $\gamma_i(f)$.

As the frequency increases, $1/\gamma_r(f)$ decreases. With $f = 300\,Hz$, $1/\gamma_r(300\,Hz) = 26.1\mu m$, $\mathbf{a} = 4.5/\gamma_r(300\,Hz) > 3.333\,\lambda$, so that the intracellular resistivities can also be estimated.

5.3.1 Estimation of interstitial resistivities (ρ_{ex}, ρ_{er})

One of the key factors in the estimation of ρ_{ex} and ρ_{er} using measured interstitial potential is $\Delta V_{\mathrm{m}} \sim -\Delta\phi_e$. Now let us examine the behavior of ϕ_i, ϕ_e and V_{m} between the two outer electrodes at $10\,Hz$ (Fig.5.4 a). The current electrodes are located at $\pm 0.22\lambda_0$ (interelectrode distance $\mathbf{a} \approx 0.15\lambda_0$) and the measurement electrodes at $\pm 0.07\lambda_0$. ϕ_i and V_{m} are shifted upward by $87\,mV$ in this figure. The voltage differences ΔV_{m}, $\Delta\phi_e$ and $\Delta\phi_i$ between the two potential-measurement electrodes for a current of $10\,Hz$ are shown in Fig.5.4 b).

Comparing Fig.5.4 a) with Fig.1 of Plonsey and Barr [61], we see that the two results are identical, that is, the intracellular potential ϕ_i is very small in comparison to ϕ_e at the potential-measurement electrode positions, and $\Delta\phi_i \approx 0$, $\Delta V_{\mathrm{m}} \approx -\Delta\phi_e$. This phenomenon occurs only at low frequencies ($< 100\,Hz$ in our case). ΔV_{m} and $\Delta\phi_e$ are very different in both phase and magnitude at high frequencies (Fig.5.5 and 5.6), because $|\Delta\phi_i|$ is no longer negligible and its phase shifts with frequency. These simulation results are concordant with experimental results [46].

If the interelectrode spacing $\mathbf{a}$ is increased, the values of the interstitial potentials at potential-measurement electrode positions become smaller (see Fig.5.4). Once $\mathbf{a}$ increases beyond a certain level, very small interstitial potentials at mea-

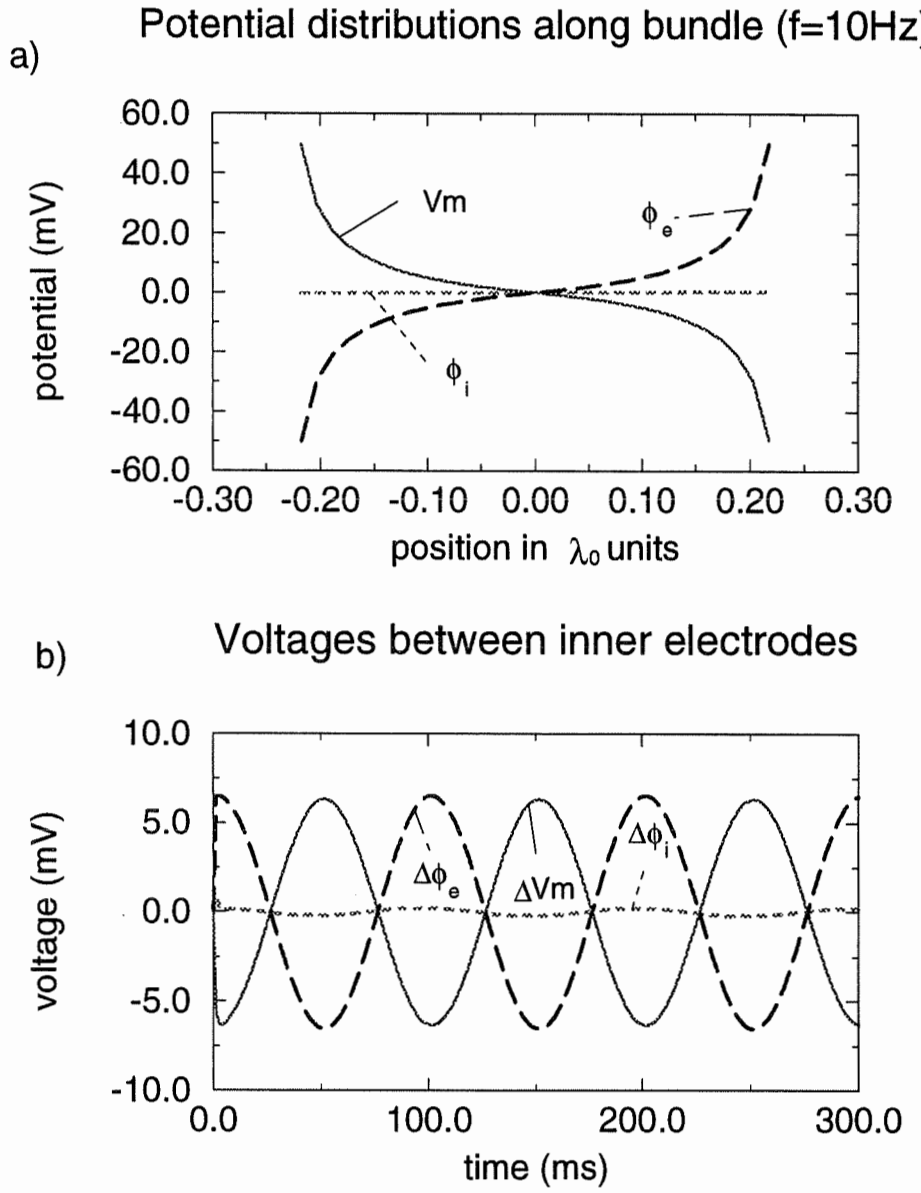

Figure 5.4: a) The distributions of V_{m}, ϕ_i and ϕ_e along the bundle axis during $10\,Hz$ stimulation. The abscissa is in units of the resting space constant of the bundle λ_0. The current sources are located at sites $\pm 0.22\,\lambda_0$. The measurement electrodes are at $\pm 0.07\,\lambda_0$. Both V_{m} and ϕ_i are shifted upward by $87\,mV$. Note that V_{m} is dominated by ϕ_e because of the very small ϕ_i. b) Voltages ΔV_{m}, $\Delta\phi_e$ and $\Delta\phi_i$ between the two potential-measurement electrodes as a function of time at $10\,Hz$.

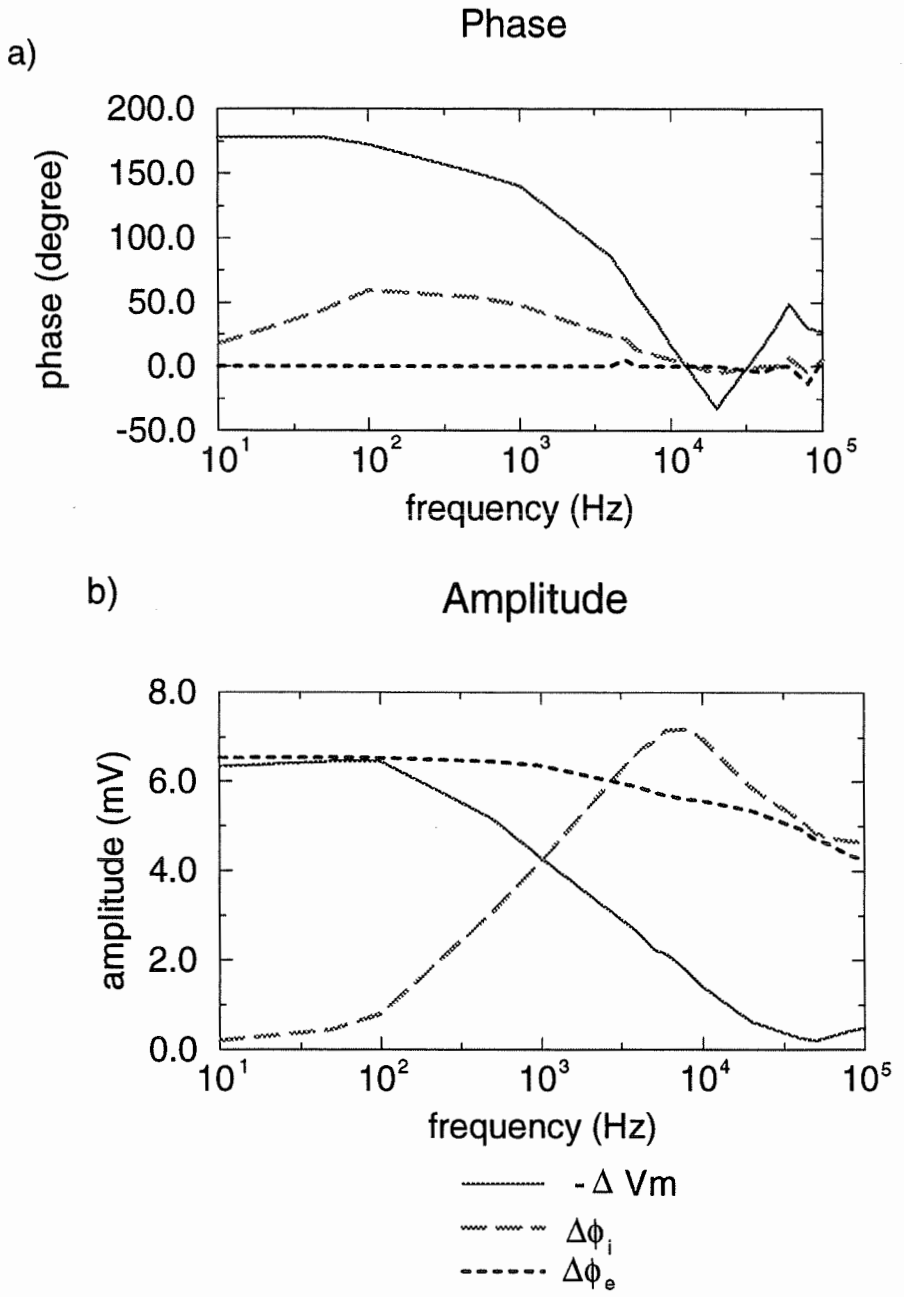

Figure 5.5: $-\Delta V_{\mathrm{m}}$, $\Delta\phi_i$ and $\Delta\phi_e$ as function of frequency for the interelectrode distance $\mathbf{a} = 100\,\mu m$. a) Phase shifts, b) magnitude variations.

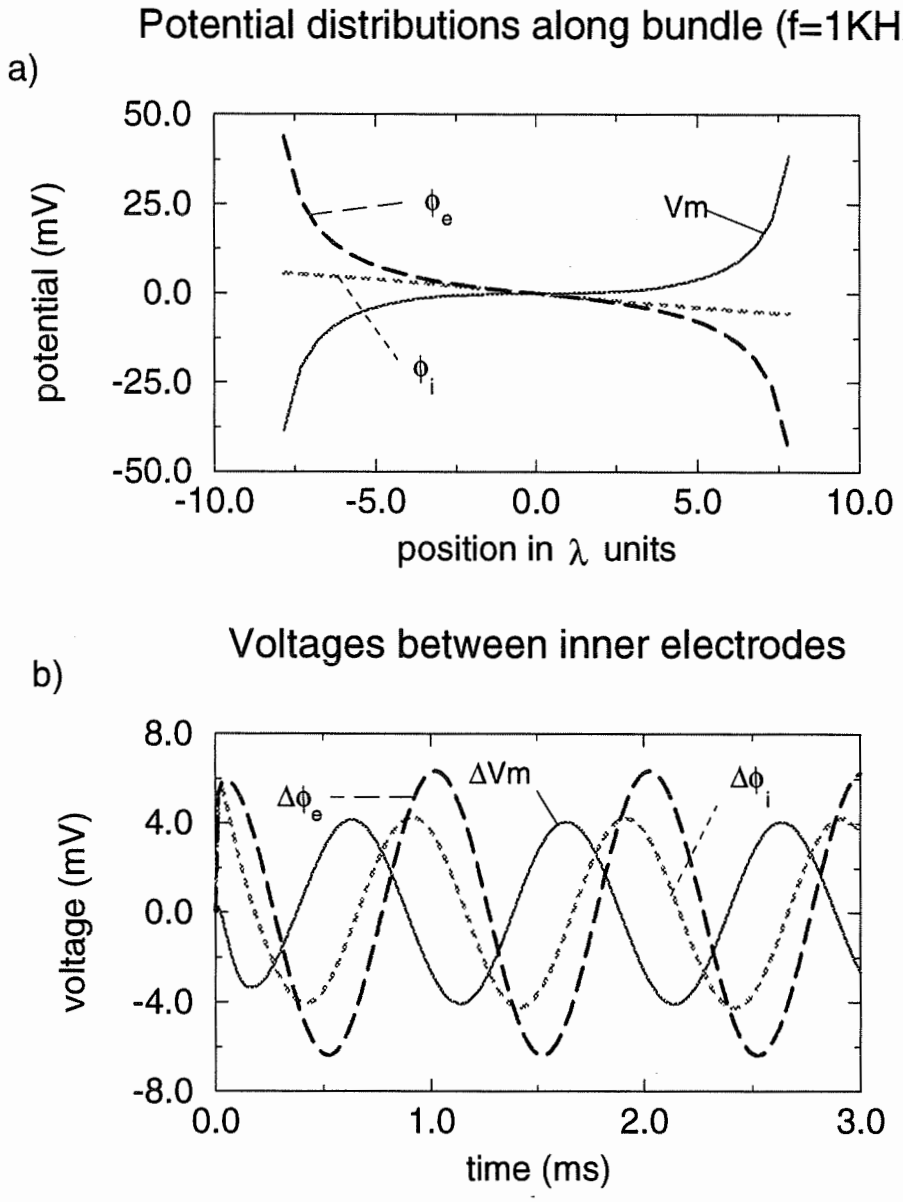

Figure 5.6: a) V_{m}, ϕ_i and ϕ_e at $1\,kHz$ along the bundle axis for $f = 1\,kHz$. The abscissa is in units of the space constant of the bundle at $1\,kHz$. The current sources are located at the sites $\pm 7.8\,\lambda$. The measuring electrodes are at $\pm 2.6\,\lambda$. b) ΔV_{m}, $\Delta\phi_i$ and $\Delta\phi_e$ between the two potential-measurement electrodes as a function of time at $1\,kHz$.

Table 5.1

Resistivity	'Impedance measurement'	Least squares method	Bidomain
ρ_{ex} (Ωcm)	115	128	116
ρ_{er} (Ωcm)	626	697	217

Table 5.1: Interstitial resistivities of the bundle ($f_i = 0.87$)

surement positions will affect the measurement quality. In our simulations, we found that **a** should be less than $130\,\mu m$ (less than $0.2\,\lambda_0$) to assure the quality of measurements.

Using Eq.(5.4) or (5.5) combined with the least squares method, the interstitial resistivities (ρ_{ex}, ρ_{er}) of the bundle were estimated at $10\,Hz$ with the intracellular volume fraction $f_i = 0.87$. The estimated values using impedance measurement are listed in Table 5.1.

To verify the quality of the measurements of ρ_{ex} and ρ_{er}, the values were substituted back into Eq.(4.10) to calculate the estimated transmembrane current $\hat{I}_{\mathrm{m}}$ and to compare it with I_{m} obtained from the original simulation. The results are displayed in Fig.5.7. The values in Table 5.1 show an 11% differences of ρ_{ex} and ρ_{er} between predictions from the impedance measurement and the least squares method. If the interelectrode distance is increased, the error is also increased. This is caused by reduced ϕ_e (see Fig.5.4). We also found that the estimated value of ρ_{ex} from the impedance measurement is identical to what the bidomain model predicts; there is, however, a large difference for ρ_{er}. This deviation is consistent with our

earlier estimates of ρ_{er} using a *d.c.* current source (see section 4.4).

5.3.2 Determination of intracellular potential $\hat{\phi}_i$

Once ρ_{ex} and ρ_{er} were obtained, we used Z_{m} and ϕ_e to determine the intracellular potential $\hat{\phi}_i$ in two steps.

- The membrane current $\hat{I}_{\mathrm{m}}$ was calculated with Eq.(4.10) using the estimated ρ_{ex} and ρ_{er}.
- $\hat{\phi}_i$ was obtained from Eq.(5.6).

Actually, because ϕ_i is very small at low frequency, it cannot always be used to estimate resistivities. To determine the frequency region where the intracellular resistivities can be evaluated, we examined how the ratio of the interelectrode distance to the parameter $\gamma(f)$, which is related to the space constant of the bundle by $1/\gamma(f) = \lambda(f)$, varies with frequency (Fig.5.8).

According to Plonsey and Barr's [61] prediction, it is possible to estimate intracellular resistivities if $\mathbf{a} > 3.333\,\lambda$. From Fig.5.8, it is clear that the intracellular parameters can be estimated for frequencies greater than $300\,Hz$ (the ratio of $\mathbf{a}$ to $1/\gamma_r$ is about 4.5). Fig.5.9 shows the calculated $\hat{I}_{\mathrm{m}}$, $\hat{\phi}_i$ from Eqs (4.10) and (5.6), based on estimated ρ_{ex} and ρ_{er} at $1\,kHz$, and compares them with those obtained from the original simulation.

After $\hat{\phi}_i$ and $\hat{I}_{\mathrm{m}}$ are calculated, the intracellular parameters ρ_{ix} and ρ_{ir} can be estimated using Eqs (4.13) to (4.14), and the least squares method. To improve

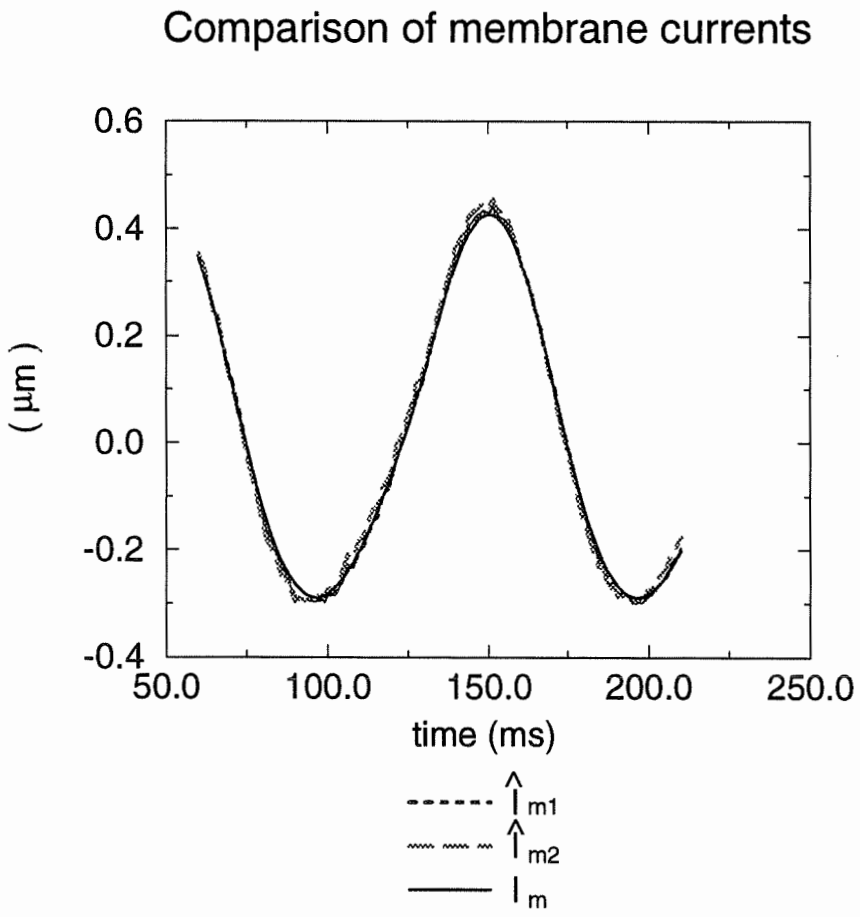

Figure 5.7: Comparison of membrane currents. $\hat{I}_{\mathrm{m1}}$: obtained from Eq.(4.10), where ρ_{ex} and ρ_{er} were estimated from Eq.(5.3), and $\hat{I}_{\mathrm{m2}}$: calculated from Eq.(4.10) using ρ_{ex} and ρ_{er} estimated from Eq.(5.4). I_{m}: original simulation.

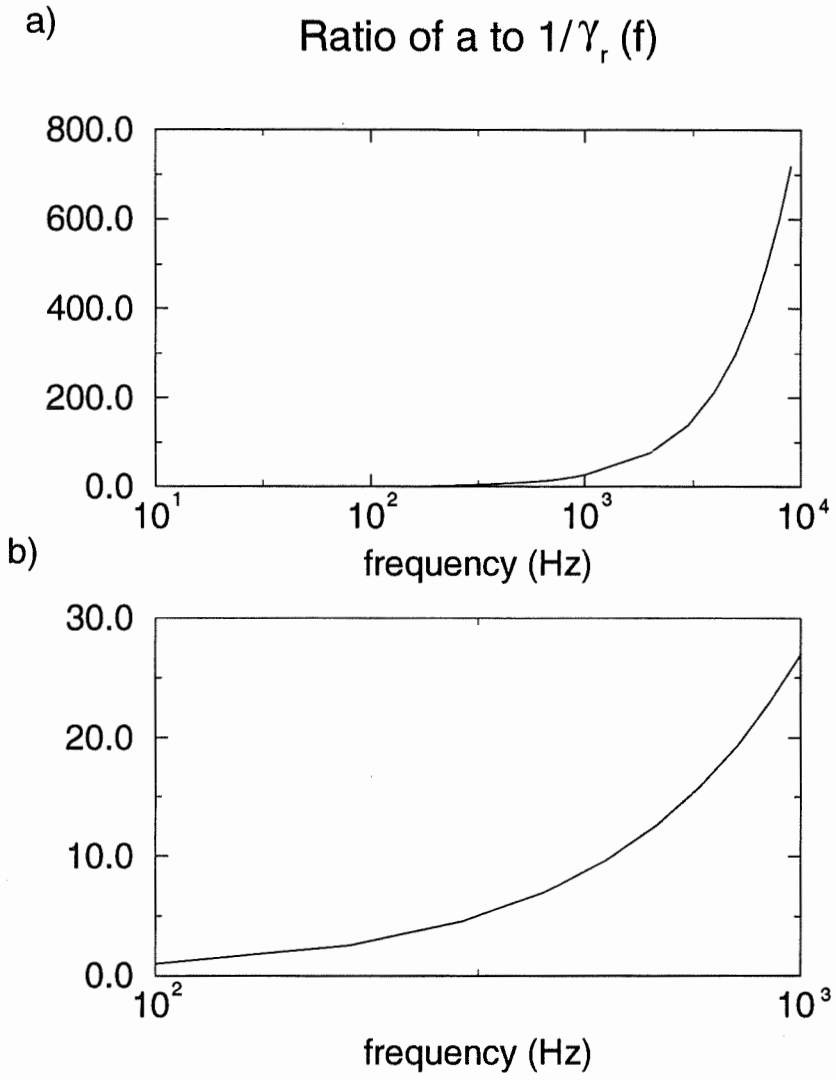

Figure 5.8: The ratio of the interelectrode spacing **a** to $1/\gamma_r(f)$. a) f from $10\,Hz$ to $10\,kHz$. b) f from $100\,Hz$ to $1\,kHz$.

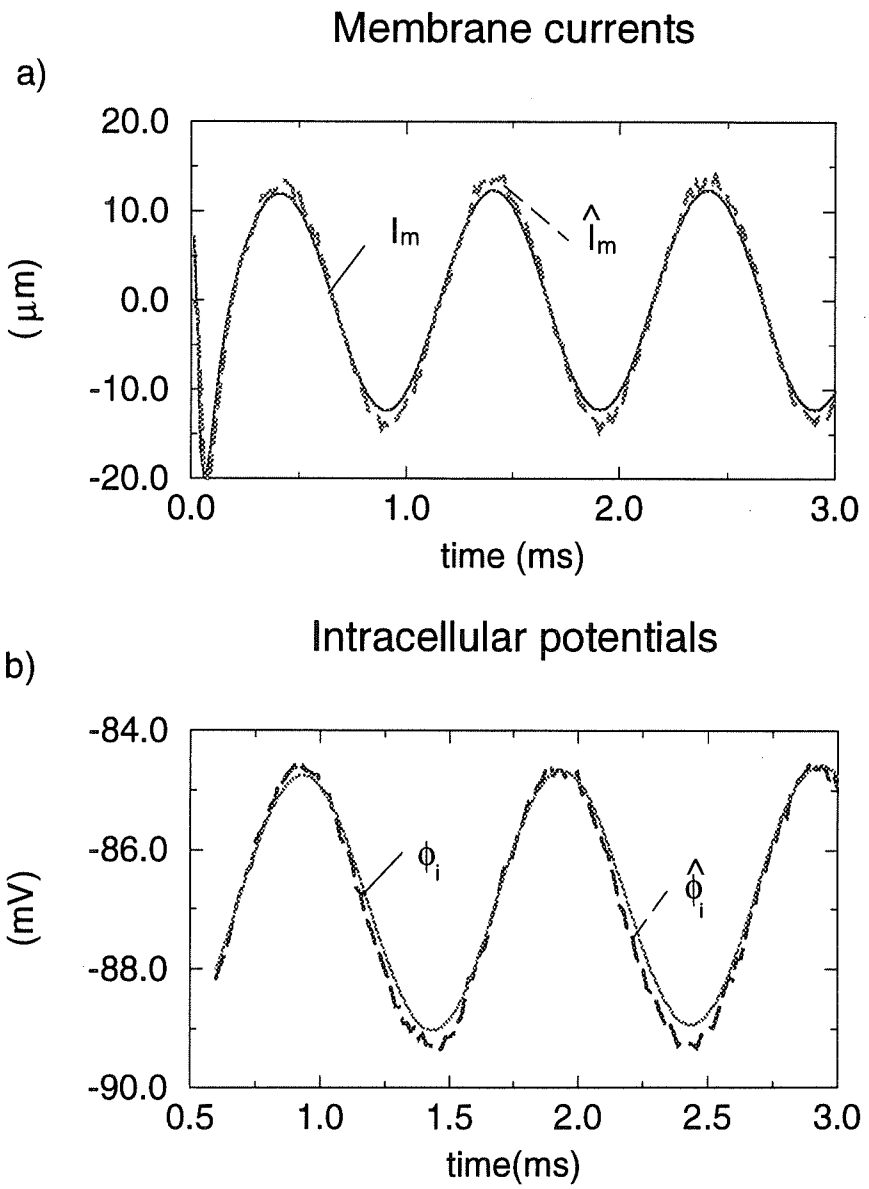

Figure 5.9: a) Membrane currents. $I_{\rm m}$ (solid curve) is obtained from the original simulation based on Eq.(2.10), $\hat{I}_{\rm m}$ (broken curve) calculated from estimated ρ_{ex} and ρ_{er} with Eq.(4.10) at $1\,kHz$. b) Intracellular potentials. ϕ_i (solid curve) is simulated by the boundary element method, $\hat{\phi}_i$ (broken curve) calculated by Eq.(5.6) based on estimated ρ_{ex}, ρ_{er} and $\hat{I}_{\rm ms}$ at $1\,kHz$.

the quality of the estimation, $\hat{I}_{\mathrm{m}}$ was smoothed to remove the numerical artifacts (see Fig.5.9) using a sinusoidal function (denoted as $\hat{I}_{\mathrm{ms}}$). Then ρ_{ix} and ρ_{ir} were estimated using $\hat{\phi}_i$ calculated from $\hat{I}_{\mathrm{ms}}$.

5.3.3 Estimation of intracellular resistivities ρ_{ix} and ρ_{ir}

The intracellular resistivities were evaluated by means of the least squares method using the previously determined $\hat{I}_{\mathrm{m}}$ and $\hat{\phi}_i$. The frequency range for the simulations was from $300\,Hz$ (where $\mathbf{a} \approx 4.5/\gamma_r$) to $1\,kHz$ ($\mathbf{a} \approx 26/\gamma_r$). Recalling the condition that Plonsey and Barr [61] suggested for the intracellular parameter measurements ($\mathbf{a} > 3.333\lambda$), we repeated our simulations for $f > 300\,Hz$. The problem at $f > 5\,kHz$ is that the magnitude of the membrane impedance $|Z_{\mathrm{m}}|$ becomes very small (around $30\,\Omega$), so that the membrane is almost transparent to current. In this case the membrane voltage or membrane current cannot be used to estimate ρ_{ix} and ρ_{ir}, because of numerical instabilities.

The quality of the estimation was examined by using calculated ρ_{ix}, ρ_{ir} and $\hat{\phi}_i$ to restore the membrane current $\hat{I}'_{\mathrm{m}}$ ($\hat{I}'_{\mathrm{m}}$ is distinct from $\hat{I}_{\mathrm{m}}$, which is calculated using the interstitial parameters ρ_{ex} and ρ_{er}), and was compared with the true I_{m}. The results at $1\,kHz$ are shown in Fig.5.10. The similarity between curves indicates that the numerical error introduced is negligible. Table 5.2 shows numerical values for estimated ρ_{ix} and ρ_{ir}, where the interelectrode spacing $\mathbf{a}$ is $120\,\mu m$ and the gap junctions connecting parallel fibers is $R_c = 2\,M\Omega/100\,\mu m$.

Table 5.2 shows that the error in estimating ρ_{ix} and ρ_{ir} using the impedance

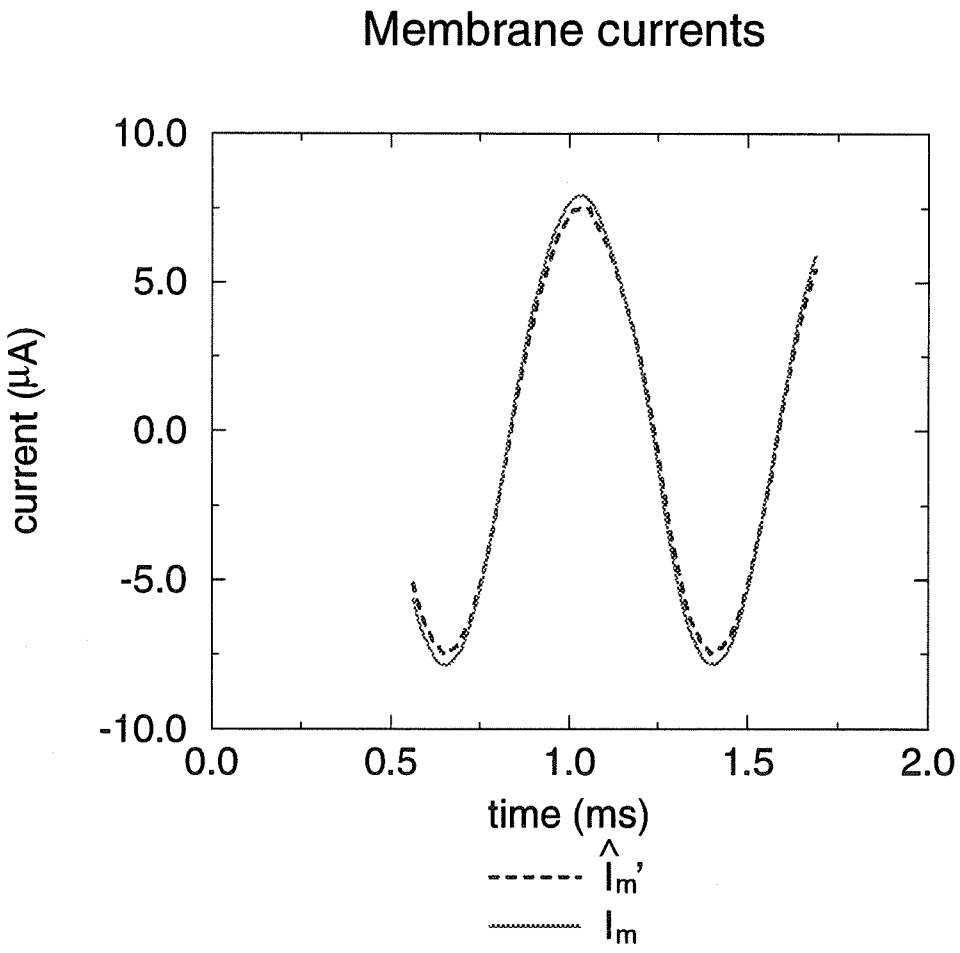

Figure 5.10: Membrane currents at $1\,kHz$. I_{m} is the membrane current from the original simulation of the boundary element method. $\hat{I}'_{\mathrm{m}}$ is restored from estimated ρ_{ix} and ρ_{ir} (see text).

Table 5.2

Resistivity	'Impedance measurement'	Least squares method	Bidomain
ρ_{ix} (Ωcm)	256	235	230
ρ_{ir} (Ωcm)	1646	1491	unavailable

Table 5.2: Intracellular resistivities of the bundle ($f_i = 0.87$)

measurement technique compared with those obtained using the least squares method was less than 10%. The numerical errors using other stimulation frequencies are on the same scale, using $\Delta t \leq 0.003ms$ and $\Delta x > 15\mu m$. Our estimated ρ_{ix} is identical to the bidomain model prediction. Since ρ_{ir} is a complicated function of the microscopic parameter ρ_i and the gap junction resistance [70], there is no standard volume fraction analytical form to calculate the intracellular radial parameter in the bidomain model. Instead, some previous studies assumed that the anisotropy ratio of the intracellular space is about 10 : 1 ($\rho_{ir} = 10\,\rho_{ix}$) [71], while others used the assumption of an equal anisotropy ratio for both the intracellular and interstitial spaces [34].

In our simulations, we found that, ρ_{ir}, like ρ_{er}, varies with the packing density (represented by the intracellular volume fraction f_i). Assuming that the anisotropy ratio of the intracellular space is about 10 in the bidomain model, we compared our results with it as in Fig.5.11. a) ρ_{ir} as function of f_i estimated by the bidomain model, b) ρ_{ir} estimated by the least squares method with $R_c = 2M\Omega/100\mu m$. We see that ρ_{ir} varies in opposite directions in the two cases. The decrease of ρ_{ir} at

Table 5.3

R_c	$2M\Omega/50\mu m$	$2M\Omega/100\mu m$	$2M\Omega/150\mu m$
ρ_{ir} (Ωcm)	1137	1492	1784

Table 5.3: Variation of estimated ρ_{ir} with R_c ($f_i = 0.87$)

tight packing as seen Fig.5.11. a) may not be true prediction according to analytical forms discussed by Roth [70] and Neu and Krassowska [56], in which ρ_{ir} is rather related to R_c the transverse connection resistance than the packing. The increase in ρ_{ir} with increased packing density (result of the least squares method, see Fig.5.11 b) is in agreement with the fact that the wavefront propagation velocity decreases as the packing density increases [34]. As expected, ρ_{ir} also varies with R_c, the transverse coupling resistance. This is shown in Table 5.3.

5.3.4 Membrane impedance Z_{m}

The membrane impedance plays a very important role in the determination of $\hat{\phi}_i$. On the other hand, ΔV_{m}, $\Delta\phi_e$ and $\Delta\phi_i$ also change when the stimulation frequency changes (see Fig.5.5) because $Z_{\mathrm{m}} = R_{\mathrm{m}}/(1 + jwR_{\mathrm{m}}C_{\mathrm{m}})$ is a function of frequency. At low frequency ($f < 100\,Hz$), jwC_{m} is much smaller than R_{m} (in our case, $C_{\mathrm{m}} = 1\mu F/cm^2$, $R_{\mathrm{m}} = 5.73K\Omega cm^2$) so that $Z_{\mathrm{m}} \approx R_{\mathrm{m}}$. As the frequency increases, jwC_{m} can no longer be ignored, so that the magnitude of Z_{m} changes and a phase shift is introduced.

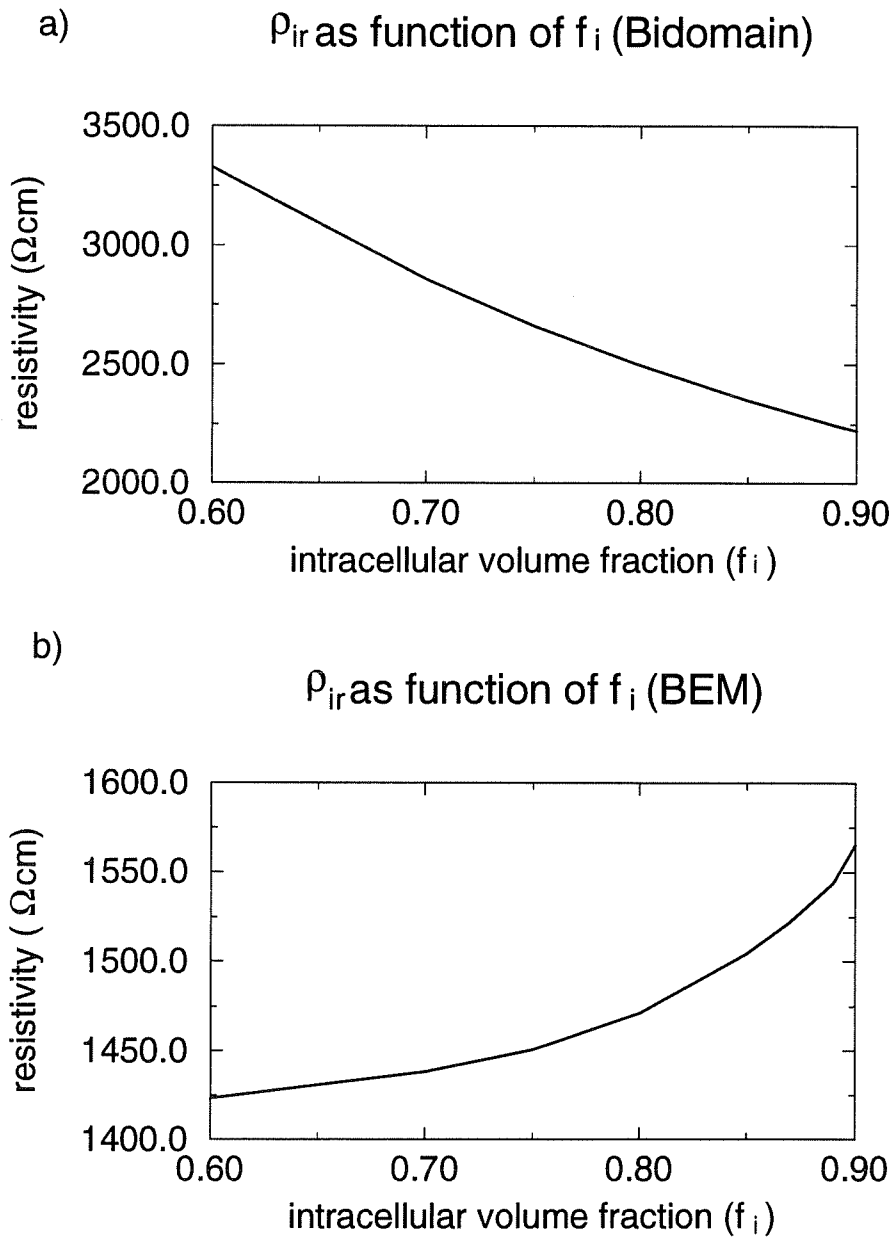

Figure 5.11: The intracellular radial resistivity ρ_{ir} as function of the intracellular volume fraction f_i. a) estimated by the bidomain model, b) predicted using the boundary element method.

In our bundle model, we assume that $C_{\rm m} = 1\,\mu F/cm^2$ and that $R_{\rm m}$ can be measured (see Section 5.2). In experimental situations, $R_{\rm m}$ and $C_{\rm m}$ are unknown. Some investigators assume the initial values of $R_{\rm m}$ and $C_{\rm m}$, and use numerical techniques to determine their true values [46]. We also tried this approach by determining $Z_{\rm m}$ iteratively using Eq.(5.6). As expected, $Z_{\rm m}$ determined in this manner was very close to the values determined by $R_{\rm m}$ and $C_{\rm m}$ using Eq.(2.39) (see Fig.5.12).

5.4 Discussion

In this chapter, we presented a numerical method, which is similar to the four-electrode technique to evaluate the bidomain anisotropic resistivities ρ_{ex}, ρ_{er}, ρ_{ix} and ρ_{ir} using only the interstitial potential and its spatial derivatives. It requires the use of a sinusoidal signal as a current source and a multi-electrode system to obtain the derivatives of the interstitial potential. The distance between the source and measurement electrodes should be determined by estimations of the interstitial resistivity parameters, and be less than $0.2\,\lambda_0$ in our bundle (shorter than suggested by Plonsey and Barr), where λ_0 represents the resting-state space constant of the bundle. Basically, two measurements are needed to determine all four bidomain resistivities. At low frequencies (where $1/Re(\gamma(f)) \approx \lambda_0$), the interstitial resistivities ρ_{ex} and ρ_{er} can be estimated with the least squares method using measured interstitial potential ϕ_e. The intracellular resistivities ρ_{ix} and ρ_{ir} can be obtained

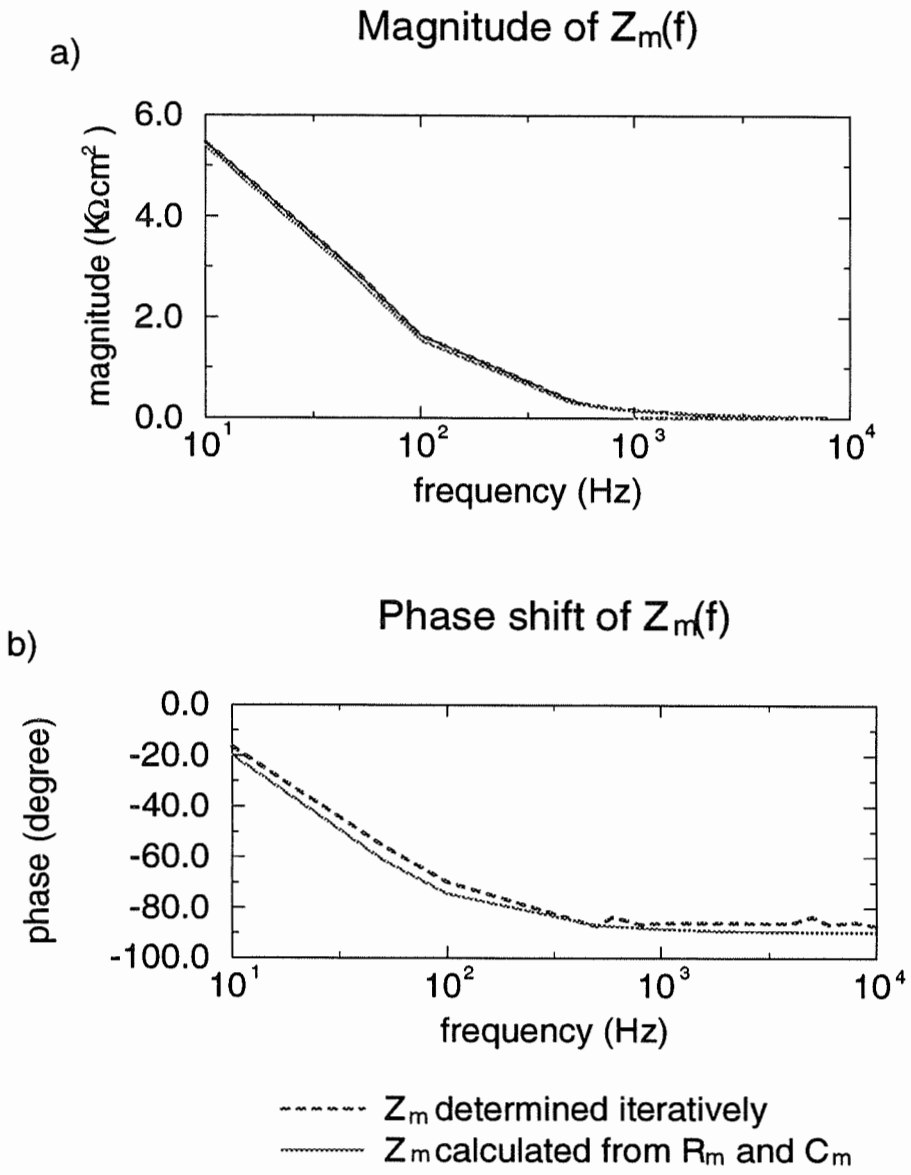

Figure 5.12: The membrane impedance Z_m as a function of frequency.

in a three step procedure by varying the frequency of the current:

- the membrane current $\hat{I}_{\mathrm{m}}$ is calculated based on the estimated ρ_{ex} and ρ_{er} at low frequency (the interstitial potential ϕ_e is always available);
- assuming that the membrane parameters R_{m} and C_{m} are known, the intracellular potential $\hat{\phi}_i$ can be determined using the previously calculated $\hat{I}_{\mathrm{m}}$ and the membrane impedance Z_{m} (see Eq.(2.39)), which is the frequency response of $R_{\mathrm{m}} \,||\, C_{\mathrm{m}}$;
- ρ_{ix} and ρ_{ir} are obtained using the same method as used to estimate ρ_{ex} and ρ_{er}.

In reality, R_{m} and C_{m} are not known. They can, however, be estimated using an iterative procedure.

In principle, this method is similar to that presented by Plonsey and Barr [61]. They suggested measuring the interstitial parameters first at small interelectrode spacing and then the intracellular parameters at large spacing. One of the main differences between our method and theirs is that the approach requires multi-electrode system or numerous measurements with a single four-electrode system along a unique axis to obtain the spatial derivatives of the interstitial potential. Another key difference is that they use the interstitial potential ϕ_e directly in both cases, while we determined ρ_{ix} and ρ_{ir} with estimated intracellular potential $\hat{\phi}_i$, which depends not only on known ϕ_e, but also on an estimate of the membrane parameters R_{m} and C_{m}. This is because the behavior of ϕ_e at different radial posi-

tions is much different from that of ϕ_i in the bundle (see section 3.2.2 Figs 3.4 and 3.5) at low frequencies. The frequency range where we evaluate ρ_{ix} and ρ_{ir} is below the critical frequency at which the cell membrane becomes transparent, so that the behavior of ϕ_i is still different from ϕ_e in this range. Thus we cannot use ϕ_e directly to estimate the intracellular resistivities.

The advantage of the impedance measurement method is that the assumption of equal anisotropy ratio is not required, improving the four-electrode method presented by Plonsey and Barr [61]. The second weakness of Plonsey and Barr's method is that a large interelectrode spacing is required to determine the intracellular resistivities, this could induce large errors into the estimate.

From a measurement point of view, high quality of biological measurements requires a good signal to noise ratio. In the bidomain model, if the interelectrode spacing increases, the current begins to split into two portions, one remains in the interstitial space, the other enters the intracellular medium. According to Plonsey and Barr, the spacing between the electrodes should be large enough so that the current equally divides between the media as if the membrane were a perfect conductor (*i.e.*, $V_{\mathrm{m}} \approx 0$). In this case, if we use the same amplitude of the current as that in the small spacing, the measured interstitial potential will be reduced considerably, which would dramatically decrease the signal to noise ratio. On the other hand, if the current is increased, the ionic current flow will be also induced, this will distort the current flowing through the interstitial space, creating new measurement error source.

The impedance measurement method has been examined by simulating a small bundle (6 radial layers and 800 μm in length). This length is very close to the resting space constant of the bundle ($\lambda_0 = 690\,\mu m$). We have increased the bundle length to $1\,mm$ and $1.2\,mm$ to examine if there is any end effect on the resistivity estimates. These simulations yielded identical results to those with $800\,\mu m$ bundle, allowing us to conclude that this length is sufficient to examine the impedance measurement method.

The distance used to estimate the spatial derivatives of the interstitial potential in the impedance measurement simulations was $15\,\mu m$. We also calculated the spatial derivatives using larger spacing ($30\,\mu m$), the errors of the estimated interstitial resistivities (ρ_{ex} and ρ_{er}) by the impedance measurement method increased to 15 % compared with the least squares simulation, there was, however, little effect on the estimates of ρ_{ix} and ρ_{ir}. The lowest frequency of current used in these simulations was $10\,Hz$, since this was the lowest frequency used by LeGuyader [46] in similar measurements. If ρ_{ex} and ρ_{er} could be estimated using lower frequencies (*e.g.* $1\,Hz$), we would expect that the distance required to measure the spatial derivatives of the interstitial potential could be increased somewhat, because the space constant at lower frequency is larger, consequently less variation of the interstitial potential between measurement-electrodes would be expected.

The distance between the current source and potential-measurement electrodes used in our simulations is about $120\,\mu m$, this is less than $200\,\mu m$ as used by LeGuyader [46]. In our simulations, this spacing was determined from estima-

tions of the interstitial resistivities at low frequency ($10\,Hz$) by injecting current far below subthreshold. If the current is increased to the value just subthreshold or by using the same current but reducing the frequency (*e.g.* $1\,Hz$, this is equivalent to increasing the space constant), the interstitial potential at measurement-electrode positions will rise (see Fig.5.4), although it may be distorted because of the induction of the ionic current. In this case, the spacing between electrodes could increase.

Next we compare the impedance measurement simulations with the results obtained by Neu and Krassowska. In a recent publication, they [56] presented an alternative theoretical approach to estimate anisotropic bidomain resistivities. It is based on the periodic structure model of tissue assumed by Hoyt *et al.* [41], where cardiac cells are modeled as hexagonal cylinders of length l_c and diameter d_c, packed into a honeycomb array. In this study, cells are assumed to be electrically connected predominantly through large gap junction. There are no end-to-end junctions or lateral connections other than those within intercalated discs of the end processes [56]. From these assumptions, Neu and Krassowska deduced new analytical formulas to estimate the bidomain resistivities. They are

$$\rho_{el} = \frac{\rho_e}{1 - f_i} \tag{5.8}$$

$$\rho_{et} = \frac{2\,\rho_e}{1 - f_i} \tag{5.9}$$

$$\rho_{il} = \rho_i \frac{1 + \frac{r_j}{3\,r_c}}{f_i} \tag{5.10}$$

$$\rho_{it} = \sqrt{3}\,l_c\,r_j \tag{5.11}$$

Table 5.4

Resistivity	IM (Ωcm)	VFM (Ωcm)	NK (Ωcm)	Experimental finding (Ωcm)
ρ_{ex}	350	333	333	$159 \sim 833$
ρ_{er}	1500	623	666	$417 \sim 1250$
ρ_{ix}	270	293	1428	$294 \sim 588$
ρ_{ir}	16330		333333	$1666 \sim 5263$

Table 5.4: Comparison of estimated resistivities of the bundle. IM: the abbreviation of the impedance measurement method, VFM: the standard volume fraction method, and NK: Neu and Krassowska's formulas.

where r_j is the junction resistance (Ω), r_c the cytoplasmic resistance ($M\Omega$) and l_c the cell length (cm). The new formulas to estimate the interstitial resistivities are almost the same as the standard volume fraction formulas (Eqs (4.15) and (4.16)) at tight packing density. Neu and Krassowska's estimates of interstitial resistivities include the effects of the transverse junctions. Table 5.4 compares the resistivity values estimated using the impedance measurement, the standard volume fraction formulas, and the new analytical formulas, respectively, based on the tissue parameters in Table 5.5, with the experimental observations.

The interstitial resistivities obtained from the standard volume fraction method and from the new formulas are similar. Our estimates of ρ_{ex} and ρ_{ix} are closer to the results of the standard volume fraction method, however ρ_{er} is much higher than the other two cases because of the difference in the assumed microstructure, (*i.e.* we assume cylindrical fibers, whereas the other two models assume fiber

Table 5.5

ρ_e	50	$\Omega\, cm$
ρ_i	250	$\Omega\, cm$
r_j	20	$M\Omega$
r_c	0.2	$M\Omega$
l_c	100	μm
f_i	0.85	

Table 5.5: Tissue parameters of simulations in Table 5.4.

to be hexagonal (see section 4.5)). Neu and Krassowska's formulas predict much higher intracellular resistivities than those obtained from our model and the experimentally observed values [13, 65]. They [56] argued that the estimates of tissue constants in Table 5.5 may not be sufficiently accurate, in particular, ρ_{ir} depends primarily on the junctional resistance r_j. Considering that standard experimental techniques to measure r_j may increase junctional resistance [56, 51], the true value of r_j may be somewhat smaller than assumed by Neu and Krassowska, which may bring estimates of ρ_{ix} and ρ_{ir} into agreement with experimental observations.

In general, our estimates of the anisotropic bidomain resistivities provide a reasonable fit to experimental measurements, although the values of radial resistivities in both media ρ_{er} and ρ_{ir} are slightly higher. There are two possible sources of this discrepancy. First, the intracellular volume fraction f_i is assumed as high as 0.85 in the simulations. From the previous study, we learned that ρ_{er} and ρ_{ir} increase dramatically as the packing density increases. In most bidomain simulations, f_i is assumed to be between 0.6 and 0.75 [34, 71]. Secondly, the transverse

junction resistance r_j used in this simulation is quite high. It is assumed that each fiber is connected to all of its neighbors through $20\,M\Omega$ connections every $100\,\mu m$. Although there is still a large variation in measured gap junction resistance, it now appears that the values of this resistance are between $1 \sim 4\,M\Omega$ [48, 89, 90], with a mean spacing of transverse connection of every $80\,\mu m$ [78]. Taking these factors account, our estimates of ρ_{er} and ρ_{ir} are in good agreement with experimental findings [13, 65].

Using this method, we found that the intracellular radial resistivity ρ_{ir} is affected not only by the packing density of the bundle, but also by the transverse resistance R_c connecting the parallel fibers inside the bundle. In the bundle structure used in our simulations, ρ_{ir} is almost proportional to $n\,R_c$, (i.e. several R_c in series), in one unit length. When the packing density is increased, the transverse distance between fibers is decreased, consequently the number of resistors in series in one unit length is increased, so that ρ_{ir} increases.

The small increase in ρ_{ir} (less than $7\,\%$ from $f_i = 0.6$ to $f_i = 0.9$) when the packing density increases is close to the prediction from the analytical form presented by Neu and Krassowska, in which they assumes that ρ_{ir} does not vary with the packing density. Comparing ρ_{ir} as function of f_i with ρ_{ir} as function of R_c as the impedance measurement simulated (see Fig.5.11), we found that the effect of the transverse connection resistance plays a more important role than the packing. Then it is reasonable for Neu and Krassowska to ignore the weak effect of the packing on ρ_{ir}. If we assume $\rho_{ir} \approx 10\,\rho_{ix}$ or assume the equal anisotropy ratio, then ρ_{ir}

decreases significantly as packing density increases, which does not agree with either our impedance measurement simulation or Neu and Krassowska's result, suggesting that it is not a good estimate of ρ_{ir}.

Chapter 6

Conclusion and Future Prospects

The goal of this thesis was to use a model of a cardiac bundle to examine the effects of microstructure on the electrical properties of cardiac tissue, and to analyse the standard technique used to measure these properties. We used the boundary element method to simulate the active and passive electrical behavior in an idealized model of uniform cardiac bundle, where each fiber is assumed to be the same physical size and the same electrical conductivity, we ignored the effects of spatial inhomogeneities introduced by collagen, blood muscle, or mitochondria. The main findings are summarized below.

- **Propagated action potential**

  Our first concern was to examine how structural factors affect the propagated action potential. In these simulations, propagation was initiated by applying a stimulus to one end of the bundle. The resultant wavefront was three dimensional, that is the transmembrane potential varied along the radius of the bundle, with the bundle surface becoming excited before its center.

There are differences also in the action potential upstroke between the center and the surface of the bundle. These differences are caused by the interstitial potential which is negligible at the bundle surface, but very large at the center. These observations are consistent with simulation results published by Henriquez [34], using a bidomain model of a much larger fiber bundle, and with the experimental results of Suenson [83] who observed similar phenomena during impulse propagation between excited and unexcited cells in the working myocardium.

Our results also demonstrate how the configuration of the early part of the propagating action potential in a cardiac bundle changes with the packing density. Increased packing density slows down propagation velocity as a result of the restricted interstitial space obstructing downstream current flow. With loose packing (intracellular volume fraction $f_i < 0.75$), the upstroke is affected only minimally by changes in the packing density, but it changes dramatically when packing is tight. This phenomenon contributes to increase in the curvature of the wavefront.

The two main features of the action potential, τ_{foot} and $\dot{V}_{max}$, behave differently with the packing density in the BEM. τ_{foot} does not demonstrate much difference between the center of the bundle and the bundle surface when the packing density varies. In both cases it increases (about 15 % from $f_i = 0.75 \sim 0.9$) with the packing density. At loose packing ($f_i < 0.75$), the difference of $\dot{V}_{max}$ between the center and the surface is very small (less than

3 %). When the packing density is increased, $\dot{V}_{max}$ decreases at the bundle surface, but increases at the center of the bundle (about 20 % difference in $\dot{V}_{max}$ at $f_i = 0.9$ between the center and the surface). At the center of the bundle, simulations of changes in the packing density using the BEM and the bidomain model yielded a similar relationship between conduction velocity and τ_{foot} (higher τ_{foot} accompanied by lower conduction velocity). Whereas a different relationship was obtained between conduction velocity and $\dot{V}_{max}$ (higher $\dot{V}_{max}$ also accompanied by lower conduction velocity).

In general, the more an excitation wavefront deviates from a flat configuration, the more the cells at the leading edge will be loaded electrically by the lagging neighboring cells [83, 79]. One then expects τ_{foot} to increase and $\dot{V}_{max}$ to decrease with a larger load (*i.e.*, with a more pronounced convexity of the wavefront). Our simulation results differ from these predictions with respect to $\dot{V}_{max}$. At the center of the bundle, both τ_{foot} and $\dot{V}_{max}$ increase with a higher curvature (tighter packing) of the wavefront, in comparison with their values at the surface. This behavior of $\dot{V}_{max}$ is caused by the interstitial potential which is negligible at the bundle surface, but very large at the center of the bundle, so that it dominates the behavior of the propagating wavefront, especially when the packing is tight (see Fig.3.11).

This behavior of the action potential upstroke at the center of the bundle may help in understanding results presented by Spach *et al* [79]. They proposed a theory of discontinuous propagation in dog myocardium in order to

explain the following findings: fast upstrokes (higher $\dot{V}_{max}$, lower τ_{foot}) were associated with low propagation velocities in the transverse direction, and slow upstrokes (lower $\dot{V}_{max}$, higher τ_{foot}) with high propagation velocities in the longitudinal direction. These experimental results were obtained at the surface of the preparation where the interstitial potential may be expected to be quite small. It is possible, therefore, that the events within the bulk of the preparation may be associated with a larger $\dot{V}_{max}$ in the longitudinal direction, due to the presence of a larger interstitial potential. One may then expect a smaller difference between longitudinal and transverse $\dot{V}_{max}$ values at a certain depth within the tissue.

In the current boundary element model of a bundle, all fibers in the bundle are uniform and with the same size, shape and electrical conductivity. In reality, cardiac tissue is far more complicated, with insulating structure such as blood vessels and collagen. To simulate more realistic cardiac tissue, we can extend our bundle model to include variations in fiber diameter and replace some fibers with insulating rods to model collagen and/or blood vessels.

- **Estimation of bidomain resistivities**

The second goal was to examine how the passive resistivities of the bundle are affected by the packing density. For this purpose, a numerical method (least squares method) was used to estimate bidomain resistivities based on simulated intracellular potential, interstitial potential, and membrane current. The method uses derivatives of potentials (either at individual time instants or

at different longitudinal positions along the bundle) to overdetermine resistivity parameters and solve them using the least squares method. The validation of the method shows that it can provide very good estimates, as long as the spatial and temporal discretizations are adequate. (*i.e.*, for the intracellular parameters $\Delta t < 0.003\,ms$, $\Delta x > 15\,\mu m$).

We concluded that all four bidomain resistivity parameters are homogeneous inside the bundle (away from the bundle surface). The predictions about the axial resistivities in both internal and external media (ρ_{ix} and ρ_{ex}), as a function of the packing density, are concordant with the predictions of the bidomain model. However, the behaviors of the radial parameters in both media (ρ_{ir} and ρ_{er}), as function of the packing density, differ from those of the bidomain model. We found that they decreased when the packing density was increased. The bidomain model also suggests a similar behavior for ρ_{er}, but much slower than what we observed. Using a bidomain model of a large cardiac strand, Henriquez [34] also found that an increase in ρ_{ir} and ρ_{er} produced more planar wavefront and faster propagation velocity, which concurs with our observations. These results suggest that the estimates of the anisotropic bidomain resistivities by the standard volume fraction formulas used in the bidomain model may not be accurate at tight packing density.

For the intracellular radial resistivity ρ_{ir}, the least square simulation shows that it increases small amount (less than 7 % from $f_i = 0.6$ to $f_i = 0.9$) when the packing density increases. In the bundle structure used in our simulations,

ρ_{ir} is almost proportional to $n\,R_c$, (i.e. several R_c in series), in one unit length. When the packing density is increased, the transverse distance between fibers is decreased, consequently the number of resistors in series in one unit length is increased, so that ρ_{ir} increases. This result is close to the prediction from the analytical form presented by Neu and Krassowska, in which they assume that ρ_{ir} does not vary with the packing density. Comparing ρ_{ir} as function of f_i with ρ_{ir} as function of R_c as the least squares simulated, we found that the effect of the transverse connection resistance on ρ_{ir} plays a more important role than the packing. Then it is reasonable for Neu and Krassowska to ignore the weak effect of the packing. The assumption of $\rho_{ir} \approx 10\,\rho_{ix}$ or the equal anisotropy ratio predicts that ρ_{ir} decreases significantly as packing density increases, which does not agree with either our least squares simulation or Neu and Krassowska's result, suggesting that it is not a good estimate of ρ_{ir}.

- **Impedance measurements**

The third goal of this thesis was to develop a method to estimate the anisotropic bidomain resistivities using only the measured interstitial potential. Based on the previously validated numerical method, we developed an approach for these measurements. In this method, the first and second spatial derivatives of the interstitial potential are needed. This requires that the potential be measured in numerous positions. It is possible to obtain two dimensional spatial derivatives of the interstitial potential in a flat tissue us-

ing a multi-electrode system [46] with this method. The method is similar to the conventional four-electrode technique, since the resistivities are estimated at two fixed positions, the current source and sink electrodes are located at the extremities, along the same axis with the distance equal to that between the two inner measurement positions. The method uses a sinusoidal signal as current source.

The distance between the source and potential measurement electrodes **a** is determined by estimations of the interstitial resistivities (in our bundle $\mathbf{a} < 0.2\,\lambda_0$, where λ_0 is the steady-state space constant of the bundle). When the frequency of the injected current changes, the electrical behavior of the membrane impedance varies and modifies the space constant of the bundle. On the other hand, the membrane impedance controls the amount of current entering into the intracellular medium. At low frequency, the membrane impedance is dominated by the membrane resistance R_{m}, because of its high value, not much current can flow into the intracellular space. In this case, the membrane voltage ΔV_{m} between the two inner potential measurement electrodes can be replaced by the measured interstitial voltage $\Delta\phi_e$. Thus the resistivities estimated by the theoretical method corresponds to the interstitial medium only. Increasing the frequency allows more and more current to pass through the membrane and the intracellular potential begins to play a role. In this case the intracellular resistivities can be determined at high frequencies with estimated intracellular potential based on previously obtained

interstitial resistivities (ρ_{ex} and ρ_{er}) and iterated membrane parameters (R_{m} and C_{m}). The frequency range to determine the interstitial resistivities is such that $\mathbf{a} < 0.5/Re(\gamma)$. In our case ($R_{\mathrm{m}} = 5.73\,K\Omega cm^2$ and $C_{\mathrm{m}} = 1\mu F/cm^2$), we have $f < 100Hz$. The range to determine the intracellular parameters is such that $4.5/Re(\gamma) < \mathbf{a} < 25/Re(\gamma)$, that is $300Hz < f < 1\,kHz$.

Theoretically, this method is similar to the approach using the bidomain model, as presented by Plonsey and Barr [61]. The advantage of our method is that it does not require the assumption of equal anisotropy ratio, as is the case with the bidomain model, and it is not limited to a specific model (as long as the interstitial potential and its derivatives are available). If the time and longitudinal discretization steps are properly chosen, the numerical errors will be within 10%.

The impedance measurement method to estimate the anisotropic bidomain resistivities established in this thesis is an improvement over the standard four-electrode method for the bidomain. However in real experimental measurements it so far can only be used in flat tissue because of the difficulty of measuring the radial spatial derivatives of the interstitial potential. In reality we feel we can extend this approach to make it applicable to a strand of cardiac muscle, by using an approximating function to replace the spatial derivatives of the interstitial potential.

The spatial derivatives of the interstitial potential are taken at each $15\,\mu m$ in our simulations. This distance between electrodes is too small to be ob-

tained experimentally. We have observed that the numerical error between the impedance measurement method and the least squares method increased by 15% if the electrode spacing is increased to $30\,\mu m$. We propose to examine the possibility of increasing this spacing. This would require estimating the interstitial resistivities at frequencies lower than $10\,Hz$.

The main contributions of this thesis are:

1. Examination of the effects of the packing density on the propagated activation wavefront, and comparison with results from bidomain model simulations.

2. Investigation of the distribution of anisotropic bidomain resistivities in the bundle in relation to the effects of the packing density.

3. Description of a numerical method to analyze the distribution of anisotropic bidomain resistivities in a cardiac bundle using simulated intracellular potential, interstitial potential and membrane current.

4. Development of an approach to evaluate the anisotropic bidomain resistivities. It is applicable to realistic measurements in a two-dimensional flat tissue. There is no assumption on the anisotropy of the tissue. Only the interstitial potential and its first and second spatial derivatives are needed for the estimations.

References

[1] Ackman JJ, Seitz MA: **Methods of complex impedance measurements in biologic tissue** , *Critical Reviews in Biomed. Eng.*, 1984; 11(4):281-311.

[2] Allessie MA, Bonke FIM, Schopman FJG: **Circus movement in rabbit atrial muscle as a mechanism of tachycardia** , *Cir.Res.*, 1973; 33:54-62.

[3] Allessie MA, Bonke FIM, Schopman FJG: **Circus movement in rabbit atrial muscle as a mechanism of tachycardia II. Role of non-uniform recovery of exitability in the occurrence of unidirectional block, as studied with micro electrodes** , *Cir.Res.*, 1976; 39:168-177.

[4] Allessie MA, Bonke FIM, Schopman FJG: **Circus movement in rabbit atrial muscle as a mechanism of tachycardia III. The 'leading circle' concept: a new model of circus movement in cardiac tissue without the involvement of an anatomical obstacle** , *Cir.Res.*, 1977; 41:9-18.

[5] Barr RC, Plonsey R: **Propagation of excitation in idealized anisotropic two-dimensional tissue** , *Biophys. J.*, 1984; 45:1191-1202.

[6] Bagno S: **Impedance measurements of living tissue** , *Electronics*, 1959; 32:62-63.

[7] Balke CW, Lesh MD, Spear JF, Kadish A, Levin JH, More EN: **Effects of cellular uncoupling on conduction in anisotropic canine ventricular myocardium** , *Cir.Res.*, 1988; 63:879-892.

[8] Beeler GW, Reuter H: **Reconstruction of the action potential of ventricular myocardial fibers**, *J. Physiol.(London)* 1977; 268:177-210.

[9] Bennett MVL, Goodenough AD: **Gap junctions, electronic coupling and intercellular communicaton** , *Neurosci. Res. Prog. Bull* (MIT press), 1978; 16:373-468.

[10] Boucher L: **Etude théorique de l'initiation et de la propagation du potentiel d'action cardiaque**, *Institut de Génie Biomédical, Ecole Polytechnique et Montréal*, Thesis, 1986.

[11] Bouty E: **Sur la conductibilité électrique de dissolutions salines très étendues** , *J. Phys.*, 1884; 2:325-355.

[12] **CRC Standard Mathematical Tables** , *CRC Press*, 1978.

[13] Clerc L: **Directional differences of impulse spread in trabecular muscle from mammalian heart**, *J. Physiol.* (London), 1976; 255:335-346.

[14] Cole KS, Curtis HJ: **Electric physiology**, *In:Glasser, O.ed.Medical Physics* Chicago: The year Book Publ. Inc.; 1950.

[15] Cranefield PF, Klein HO, Hoffman BF: **Conduction of the cardiac impulse. I. Delay, block and one-way block in depressed Purkinje fibers** , *Circ.Res.*, 1971; 28:199-219.

[16] Cranefield PF: **Conduction of the cardiac impulse. The slow response and cardiac arrhythmias** , *Mt.Kisco, New York, Futura Publishing Company*, 1975; p 304.

[17] Courant R, Hilbert D: **Methods of mathematical physics** , *Interscience Publishers*, 1962, Volume 2.

[18] Deily GR: **Exponential curve fit** , *Comm.,ACM.2* 1966; p85.

[19] Deily GR: **Algorithm 275 exponential curve fit** , *Collected Algorithms from CACM*, 1972.

[20] De Mello WC: **Cell-to-cell communication in heart and other tissues** , *Prog. Biophys. molec. Biol.*, 1982; 39:147-182.

[21] Delgado C, Steinhaus B, Delmar M, Chialvo D, Jalife J: **Directional differences in excitability and margin of safety factor for propagation in ventricular sheep epicardial muscle** , *Circ. Res.*, 1990; 67:97-110.

[22] Delmar M, Michaels D, Johnson T, Jalife J: **Effects of increasing intracellular resistance on transverse and longitudinal propagation in sheep epicardial muscle** , *Circ.Res.*, 1987; 60:780-785.

[23] Drouhard JP, Roberge FA: **Revised formulation of the Hodgkin-Huxley representation of the sodium current in cardiac cells** *Computers and Biomedical Research*, 1987; 20:333-350.

[24] Ebihara L, Johnson EA: **Fast sodium current in cardiac muscle. A quantitative description** *Biophys. J.*, 1980; 32:779-790.

[25] Eisenberg RS, Barcilon V, Mathias RT: **Electrical properties of spherical syncytia** *Biophys. J.*, 1979; 25:151-180.

[26] Fozzard HA: **Membrane capacity of the cardiac Purkinje fiber**, *J. Physiol.*, (London) 1966; 182:255-267.

[27] Geselowitz DB, Miller III WT: **A bidomain model for anisotropic cardiac muscle**, *Ann. Biomed. Eng.*, 1983; 11:191-206.

[28] Gettes LS, Buchanan JW Jr, Saito T, Kagiyama Y, Oshita S, Fujino T: **Studies concerned with slow conduction**, in Zipes DP, Jalife J (eds): *Cardiac Electrophysiology and Arrhythmias*, Orlando, FL, Grune & Stratton, 1985; pp 81-87.

[29] Geddes LA, Baker LE: **Principles of applied biomedical instrumentation**, *John Wiley & Sons*, New York, 1975; chapter 10.

[30] Hellam DC, Studt JW: **A core-conductor model for the cardiac Purkinje fiber based on strctural analysis**, *J. Physiol.*, (London) 1974; 243:637-660.

[31] Henriquez CS, Trayanova N, Plonsey R: **Potential and current distributions in a cylindrical bundle of cardiac tissue**, *Biophys. J.* 1988; 53:907-918.

[32] Henriquez CS: **Structure and volume conductor effects on propagation in cardiac tissue**, *Ph.D. Dissertation*, Duke University, 1988.

[33] Henriquez CS, Plonsey R: **Simulation of propagation along a cylindrical bundle of cardiac tissue–I: mathematical formulation**, *IEEE Trans. Biomed. Eng.*, 1990; 37:850-860.

[34] Henriquez CS, Plonsey R: **Simulation of propagation along a cylindrical bundle of cardiac tissue–II: results of simulation**, *IEEE Trans. Biomed. Eng.*, 1990; 37:861-875.

[35] Henriquez CS: **Simulating the electrical behavior of cardiac tissue using the bidomain model**, *Crit. Rev. Biomed. Eng.*, 1993; 21(1):1-77.

[36] Hodgkin AL, Huxley AF: **A quantitative description of membrane current and its application to excitation and conduction in the nerve** , *J. Physiol.*, (London) 1952; 117:500-544.

[37] Hogan PM, Davis LD: **Evidence for specialized fibers in the canine right atrium** , *Circ. Res.*, 1968; 23:387-396.

[38] Hogues H, Leon LJ: **Electric field interactions between cardiac myocytes**, *Proceedings of the Canadian Medical and Biological Engineering*

Society Conference, 1990.

[39] Hogues H, Leon LJ: **A study of propagation of impulses in a bundle of cardiac fibers using a boundary element model**, *Computers in Biomedicine*, Computational Mechanics Publications 1991; 337-346.

[40] Hogues H, Leon LJ, Roberge FA: **A model study of electric field interactions between cardiac myocytes**, *IEEE Trans. Biomed. Eng.*, 1992; 39:1232-1243.

[41] Hoyt RH, Cohen ML, Saffitz JE: **Distribution and three-dimensional structure of intercellular junctions in canine myocardium**, *Cir. Res.*, 1989; 64:563.

[42] Jack JJB, Noble D, Tsien RW: **Electric current flow in excitable cells**, *Clarendon Press · Oxford*, 1975.

[43] Kadish AH, Spear JF, Levine JH, Moore EN: **The effects of procainamide on conduction in anisotropic canine ventricular myocardium** , *Circulation*, 1986; 74:616-625.

[44] Kléber AG, Riegger CB: **Electrical constants of arterially perfused rabbit papillary muscle**, *J. Physiol*, (Lond) 1987; 385:307-324.

[45] Kléber AG, Riegger CB, Janse MJ: **Electrical uncoupling and increase of extracellular resistance after induction of ischemia in isolated, arterially perfused rabbit papillary muscle**, *Cir. Res.*, 1987; 61:271-279.

[46] Le Guyader PM: **Cartographie des propriétés électriques passives du tissu cardiaque**, *Mémoire de maîtrise és sciences appliquées*, Ecole Polytechnique de Montréal, 1992.

[47] Leon LJ, Roberge FA: **A new cable model formulation based on Green's theorem**, *Annals of biomedical Engineering*, 1990; 18:1-17.

[48] Leon LJ, Roberge FA: **Structural complexity effects on transverse propagation in a two-dimensional model of myocardium**, *IEEE Trans. Biomed. Eng.*, 1991; 38:997-1009.

[49] Lesh MD, Spear JF, Moore EN: **The importance of cell coupling and anisotropy to conduction in cardiac tissue** in Fisch C, Surawicz B (eds): *Cardiac Electrophysiology and Arrhythmias*, Elsevier Science Publishing Co. Inc., 1991; pp 25-34.

[50] McWilliam JA: **Fibrillar contraction of the heart**, *J. Physiol.*, 1897; 8:296-310.

[51] Metzger P, Weingart R: **Electric current flow in cell pairs isolated from adult rat hearts**, *J. Physiol.*, 1985; 366:177.

[52] Miller WT, Geselowitz DB: **Simulation studies of the electrocardiogram**, *Circ.Res.*, 1978; 43:301-315.

[53] Mines GR: **On dynamic equilibrium in the heart**, *J. Physiol.*, 1913; 46:350-383.

[54] Mobley BA, Page E: **The surface area of sheep cardiac Purkinje fibers**, *J. Physiol.*, 1972; 220:547-563.

[55] Moe GK, Mendez C, Han J: **Abberant av impulse propagation in the dogheart: A study of functional bundle branch block**, *Circ.Res.*, 1965; 16:261-286.

[56] Neu JC, Krassowska W: **Homogenization of syncytial tissues** , *Crit. Rev. Biomed. Eng.*, 1993; 21(2):137-199.

[57] Nyboer J: **Electrical impedance plethysmography** , *Medical Physics*, Year Book Publishers, Chicago, 1944; 1:744.

[58] Nyboer J: **Electrical impedance plethysmography** , *Charles C. Thomas, Springfield*, 1959; I11:243.

[59] Paes de Carvalho A, Hoffman BF, de Paula Carvalho M: **Two components of the cardiac action potential. I. Voltage time course and the effect of acetylocholine on atrial and nodal cells of the rabbit heart** , *J.Gen.Physiol.*, 1969; 54:607-635.

[60] Plonsey R: **Bioelectric phenomena**, *McGraw-Hill*, 1969.

[61] Plonsey R, Barr RC: **The four-electrode resistivity technique as applied to cardiac muscle**, *IEEE Trans. Biomed. Eng.*, 1982; 29:541-546.

[62] Plonsey R, Barr RC: **A critique of impedance measurements in cardiac tissue**, *Annals of Biomedical Eng.*, 1986; 14:307-322.

[63] Plonsey R: **Bioelectric sources arising in excitable fibers**, *Ann Biomed Eng*, 1988; 16:519-546.

[64] Pollard AE, Hooke N, Henriquez CS: **Cardiac propagation simulation**, in *High Performance Computing in Biomedical Engineering*, Pilkington TC, Loftis b, Thompson JF et al. CRC Press, 1992.

[65] Roberts DE, Hersh LT, Scher AM: **Influence of cardiac fiber orientation on wavefront voltage, conduction velocity, and rissue resitivity in the dog**, *Circ Res*, 1979; 44:701-712.

[66] Roberts DE, Scher AM: **Effect of tissue anisotropy on extracellular potential fields in canine myocardium in situ**, *Circ Res*, 1982; 50:342-351.

[67] Roth BJ, Wikswo,Jr. JP: **A bidomain model for the extracellular potential and magnetic field of cardiac tissue**, *IEEE Trans. Biomed. Eng.*, 1985; 33:467-469.

[68] Roth BJ, Gielen FLH: **A comparison of two models for calculating the electrical potential in skeletal muscle**, *Annals of Biomedical Eng.*, 1987; 15:591-602.

[69] Roth BJ, Gielen FLH, Wikswo,Jr. JP: **Spatial and temporal frequency-dependent conductivities in volume-conduction calculations for skeletal muscle**, *Mathematical Biosciences*, 1988; 88:159-189.

[70] Roth BJ: **The electrical potential produced by a strand of cardiac muscle: a bidomain analysis**, *Annals of Biomedical Eng.*, 1988; 16:609-637.

[71] Roth BJ: **Action potential propagation in a thick strand of cardiac muscle** , *Circ. Res.*, 1991; 68:162-173.

[72] Rush S, Abildskov JA, McFee R: **Resistivity of body tissue at low frequencies**, *Circ. Res.*,1963; 12:40-50.

[73] Sano T, Takayama N, Shimamoto T: **Directional differences of conduction velocity in cardiac ventricular syncytium studied by microelectrodes**, *Circ. Res.* 1959; 7:262-267.

[74] Schwan HP, Kay CF: **The conductivity of living tissues**, *Ann. N.Y. Acad. Sci.*, 1957; 65:1007-1013.

[75] Schwan HP, Ferris CD: **Four-electrode null techniques for impedance measurement with high resolution**, *The Review of Scientific Instruments*, 1968; 39:481-485.

[76] Sjöestrand FS, Andersson-Cedergren E, Dewey MM: **The ultrastructure of the intercalated disc of frog, mouse and guinea pig cardiac muscle**, *J. Ultrastruct. Res.*, 1958; 1:271-287.

[77] Sommer JR, Johnson EA: **Cardiac muscle. A comparative study of Purkinje fibers and ventricular fibers**, *J. Cell Biol.*, 1968; 36:497-526.

[78] Sommer JR, Scherer B: **Geometry of cell and bundle appositions in cardiac muscle: light microscopy**, *Am. J. Physiol.*, 1985; 248:H792-H803.

[79] Spach MS, Miller WT, Geselowitz DB, Barr RC, Kootsey JM, Johnson EA: **The discontinuous nature of propagation in normal canine cardiac muscle. Evidence for recurrent discontinuities of intracellular resistance that affects the membrane currents**, *Circ. Res.*, 1981; 48:39-54.

[80] Spach MS, Miller WT, Dolber PC, Kootsey JM, Sommer JR, Mosher JrCE: **The functional role of structural complexities in the propagation of depolarization in the atrium of the dog** , *Cir. Res.*, 1982; 50:175-191.

[81] Spach MS: **The discontinuous nature of electrical propagation in cardiac muscle**, *Ann.Biomed. Eng.*, 1983; 11:209-261.

[82] Spach MS, Dolber PC, Heidlage JF: **Influence of the passive anisotropic properties on directional differences in propagation following modification of the sodium conductance in human atrial muscle. A model of reentry based on anisotropic discontinuous propagation**, *Cir. Res.*, 1988; 62:811-832.

[83] Suenson M: **Interaction between ventricular cells during the early part of excitation in the ferret heart**, *Acta. Physiol. Scand.*, 1985; 125:81-90.

[84] Tung L: **A bidomain model for describing ischemic myocardial d.c. potentials**, *Ph. D. Dissertation*, Massachusetts Inst. Technol. Cambridge, 1978.

[85] Veenstra RD, DeHaan RL: **Measurement of single channel currents from cardiac gap junctions** , *Science (Washington, D.C.)*, 1986; 233-972.

[86] Wagner ML, Lazzara R, Weiss RM, Hoffman BF: **Specialized conducting fibers in the interatrial band** , *Circ. Res.*, 1966; 18:502-518.

[87] Weidmann S: **The electrical constants of Purkinje fibers** , *J. Physiol.*, (London) 1952; 118:348-360.

[88] Weidmann S: **Electrical constants of trabecular muscle from mammalian heart** , *J. Physiol.*, (London) 1970; 210:1041-1054.

[89] Weingart R, Maurer P: **Action potential transfer in cell pairs from adult rat and guinea pig ventricles** , *Circ. Res.*, 1988; 63:72-80.

[90] Weingart S: **Electrical properties of the nexal membrane studied in rat ventricular cell piars** , *J. Physiol.*, 1986; 370:267-284.